E-1A

A SEARCH FOR WEAK NEUTRAL CURRENTS IN SEMILEPTONIC INTERACTIONS

Fredric Messing

A DISSERTATION

IN

PHYSICS

1975

FERMILAB
LIBRARY

A SEARCH FOR WEAK NEUTRAL CURRENTS IN SEMILEPTONIC INTERACTIONS

Fredric Messing

A DISSERTATION
IN
PHYSICS

Presented to the Faculty of the Graduate School of Arts and Sciences
of the University of Pennsylvania in Partial Fulfillment of the
Requirements for the Degree of Doctor of Philosophy

1975

Supervisor of Dissertation

Graduate Group Chairman

FERMILAB
LIBRARY

ABSTRACT

A SEARCH FOR WEAK NEUTRAL CURRENTS

IN SEMILEPTONIC INTERACTIONS

Fredric Messing

Professor Alfred K. Mann, Supervisor of Dissertation

The subject of this paper is a search for weak neutral currents in semileptonic interactions. One of the puzzling aspects of weak interactions is the fact that they appear to depend on the electromagnetic charge of the particles involved. A second puzzle has been the nearly identical forms of the weak and electromagnetic Lagrangians. These puzzles have led to considerable speculation that the two forces might be related. Such speculations lead naturally to the idea that neutral currents should manifest themselves in weak interactions.

Searches for weak neutral currents have been based primarily on the decays of K mesons. These have lead conclusively to the idea that neutral current interactions cannot be accompanied by a change in strangeness. Attempts to search for strangeness conserving weak neutral currents by utilizing particle collisions are generally unsatisfactory due to the presence of strong and electromagnetic forces. These problems are overcome by the use of neutrino beams since the neutrino interacts only via the weak force.

An experiment was performed in the neutrino beam of the Fermi National Accelerator Laboratory to search for weak neutral current

interactions. The neutrinos (ν_μ) and antineutrinos ($\bar{\nu}_\mu$) entered a target-detector consisting of sixteen modules of ionization calorimeters filled with liquid scintillator. When a ν_μ ($\bar{\nu}_\mu$) interacted via a neutral current, the final state ν_μ ($\bar{\nu}_\mu$) was undetectable. When a ν_μ ($\bar{\nu}_\mu$) interacted through the charged current, the final state muon generally emerged from the calorimeter and entered a magnetic spectrometer. The muon was recorded in any of five optical wide gap spark chambers or any of eighteen scintillation counters which it traversed within the spectrometer. Charged current interactions could therefore be distinguished from neutral current interactions by the observation of a muon in the spectrometer.

The data presented here are from two runs of the experiment characterized by different energy spectra and different values of the parameter α which is the ratio of the number of charged current events due to ν_μ divided by the number of charged current events due to both ν_μ and $\bar{\nu}_\mu$. After applying corrections (primarily for the acceptance of the spectrometer) it was found that the ratio R of events without muons to events with muons was $R = .22 \pm .04$ for $\alpha = .62$ and $R = .32 \pm .04$ for $\alpha = .94$ where the errors are statistical only. Systematic errors on R are estimated to be about .03. Backgrounds are estimated to be at the .01 level.

While the existence of events without muons is strongly supported by the data, it is not yet possible to pin down their source. Several possibilities have been considered which are con-

sistent with the data. These include heavy lepton production, violation of muon number conservation, and the existence of weak neutral currents. For the case of heavy leptons it is shown that a mass of $3.1 \pm .5$ GeV/c^2 and a small branching ratio into final states with muons would explain the observations. Under the assumption that weak neutral currents are the source, the space-time properties of the current are discussed in light of the variation of R with the energy transferred to the hadron system.

ACKNOWLEDGEMENTS

The research described here could not have been accomplished without the participation of a large number of talented people. Each member of the Harvard-Pennsylvania-Wisconsin-Fermilab (HPWF) collaboration made essential contributions. The members are: Bernard Aubert, Alberto Benvenuti, Dave Cheng, Dave Cline, Bill Ford, Richard Imlay, Ta-Yung Ling, Al Mann, Bob Piccioni, Jim Pilcher, Don Reeder, Carlo Rubbia, Ray Stefanski, and Larry Sulak.

We were assisted in this work by the highly competent technical staffs of the universities and of the Physical Sciences Laboratory, Stoughton, Wisconsin. In particular, the efforts of Bob Beck, Ed Mayer, L. C. Thomas, and Hans Weedon were invaluable. I gratefully acknowledge the efforts of the many people at Fermilab who were responsible for making this laboratory such a highly productive research facility.

INDEX

Acceptance	(see detection efficiency)
α	12, 19, 25, 31, 56, 72, 101
Backgrounds	4, 12, 22, 30, 35
Beam	(see α and energy spectra) 10, 36, 53, 110
Beta decay	1
Boson	(see W boson)
Calorimeter	10, 14, 38, 50, 53, 65, 111
Coulomb Scattering	17, 18, 24, 52
Counters	10, 11, 15, 24, 47, 49, 53, 56, 58, 65, 122
Cross sections	7, 26, 28, 29, 31, 33, 103, 105
Decays	1, 3, 10, 26, 29, 36, 55, 61, 62
Detection efficiency	12, 15, 17, 19, 27, 43, 56, 72, 75, 82
E_H	7, 11, 14, 16, 19, 20, 22, 24, 27, 30, 32, 34, 39, 41, 70, 72, 86, 98, 109, 132
Electron neutrino (ν_e)	1, 4, 22, 27, 28
Energy spectra (E)	4, 11, 20, 24, 63, 88, 91
Fermi Theory of weak interaction	1, 35
Gauge theories	27, 33, 108
Hadron energy	(See E_H)
Hadron penetration	10, 15, 16, 19, 70, 72, 74
Heavy leptons (L)	27, 32, 34, 35, 102
Horn, magnetic,	12, 36, 101
Intermediate vector boson	(see W boson)

K mesons	3, 10, 23, 36, 50, 61, 62
Magnet	11, 24, 44, 49, 65, 118, 130
Marks generator	42, 49, 53, 116
Monte Carlo	18, 24
Noise	38, 49, 126, 133
Optics	42, 51, 127
π mesons	3, 10, 23, 36, 39, 52, 61, 62, 115
R	19, 20, 22, 30, 31, 33, 72, 82, 89, 108, 109
Resolutions	40, 47, 52, 58, 69, 73, 115, 130
R_L	28, 34, 105
R_W	26, 104
Scaling	8
Scanning	14
Scintillator	10, 11, 38, 47, 57, 58
Space-time properties	(see transformation properties)
Spark chambers	(see wide gap spark chambers)
Spectrometer	(see magnet)
Target detector	(see Calorimeter)
θ	7, 18, 20, 24, 75, 76, 78, 95
Transformation Properties	1, 7, 8, 28, 30, 108
TRIM	46, 58, 120
W boson	2, 26, 32, 60, 64, 102, 103
Weinberg-Salam model	33, 108

Wide gap spark chambers (WGSC) 10, 14, 24, 42, 49, 51, 53, 65, 117, 127

TABLE OF CONTENTS

	ACKNOWLEDGEMENTS	ii
	INDEX	iii
	TABLE OF CONTENTS	vi
	BIBLIOGRAPHY	vii
	FIGURE CAPTIONS	x
I.	INTRODUCTION	1
II.	PHYSICAL MODEL OF NEUTRINO INTERACTIONS	7
III.	DATA COLLECTION	10
IV.	EVENT SELECTION AND DATA ANALYSIS	14
V.	BACKGROUNDS	22
VI.	THE MONTE CARLO SIMULATION	24
VII.	POSSIBLE SOURCES OF NEUTRAL INTERACTIONS	26
VIII.	CONCLUSIONS	35
IX.	THE BEAM	36
X.	IONIZATION CALORIMETER	38
XI.	WIDE GAP SPARK CHAMBERS (WGSC)	42
XII.	IRON CORE MAGNET	44
XIII.	TRIGGER COUNTERS	47
XIV.	NOISE	49
XV.	OPTICS	51
XVI.	ELECTRONIC LOGIC AND DATA RECORDING	53
FOOTNOTES		55
FIGURES		60

BIBLIOGRAPHY

Albright, C. H., et al., Ref. Th. 1855-CERN, 1974.

Aubert, B., et al., Physical Review Letters 32, 1454 (1974).

Aubert, B., et al., Physical Review Letters 32, 1457 (1974).

Aubert, B., et al., Physical Review Letters 33, 984 (1974).

Barger, V., "Two Component Dual Parton-Regge Model of Deep Inelastic Electron and Neutrino Structure Functions", Preprint (1973).

Barish, B. C., et al., Physical Review Letters 31, 180 (1973).

Barish, B. C., et al., Physical Review Letters 31, 410 (1973).

Barish, B. C., et al., Physical Review Letters 32, 1387 (1974).

Benvenuti, A., et al., Physical Review Letters 30, 1084 (1973).

Benvenuti, A., et al., Physical Review Letters 32, 125 (1974).

Benvenuti, A., et al., Physical Review Letters 32, 800 (1974).

Bernardini, G., et al., Il Nuovo Cimento 38, 608 (1965).

Bernardini, G., Rendiconti Della Scuola Internazionale Di Fisica "Enrico Fermi", Course XXXII, 1 (1964).

Bjorken, J. D., Llewllyn-Smith, C. H., Physical Review D7, 887 (1973).

Bjorken, J. D., Paschos, E. A., Physical Review D1, 3152 (1970).

Bjorken, J. D., Physical Review 179, 1547 (1969).

Bloch, P., et al., XVII International Conference on High Energy Physics, London, 1974.

Brown, R. W., Smith, J., Physical Review D3, 207 (1971).

Burns, R., et al., Physical Review Letters 15, 42 (1965).

Camerini, U., et al., Nuovo Cimento 37, 1795 (1965).

Carithers, W. C., et al., Physical Review Letters 30, 1336 (1973).

Clark, A. R., et al., Physical Review Letters 26, 1667 (1971).

Cundy, D. C., et al., Physics Letters 31B, 478 (1970).

Eichten, T., et al., Physics Letters 46B, 274, 281 (1973).

Fermi, E., Nuovo Cimento 11, 1 (1934).

Feynman, R. P., Gell-Mann, M., Physical Review 109, 193 (1958).

Gurr, H. S., et al., Physical Review Letters 28, 1406 (1972).

Gurr, H. S., et al., Physical Review Letters 33, 179 (1974).

Hassert, F. J., et al., Physics Letters 46B, 138 (1973).

Keller, Schluter, and White, Nuclear Instruments and Methods, 41 (1966).

Klems, J. H., et al., Physical Review D4, 66 (1971).

Lari, and Wilhelm, Computer Program TRIM for Magnet Design, Argonne National Laboratory, May 20, 1970.

Lee, W., Physics Letters 40B, 423 (1972).

Limon, P., et al., Fermilab Report No. NAL-Pub-73/66-EXP, (1973).

Llewllyn-Smith, C. H., Ref. Th. 1621-CERN, 1973.

Miller, G., et al., Physical Review D5, 528 (1972).

Paschos, E. A., Wolfenstein, L., Physical Review D7, 91 (1973).

Perkins, D. H., 16th International Conference on High Energy Physics, Chicago-Batavia, 1972.

Rubbia, C., 16th International Conference on High Energy Physics, Chicago-Batavia, #687, 1972.

Salam, A., Elementary Particle Theory, edited by N. Svartholm, Almquist and Forlug, Stockholm, 1968.

Stech, B., International Conference of Elementary Particles, Aix-En-Provence, 1973.

Sehgal, L. M., Nuclear Physics B65, 141 (1973).

Weinberg, S., Physical Review Letters 27, 1688 (1971).

FIGURE CAPTIONS

Fig. 1 Diagrams for electron-electron interactions mediated by electromagnetic forces and possible weak neutral forces.

Fig. 2 Possible decays of K mesons involving weak neutral leptonic currents.

Fig. 3 Results of searches for the decay modes listed in Fig. 2.

Fig. 4 Neutrino energy (E) spectra available at various laboratories.

Fig. 5 Analogous inelastic weak and electromagnetic interaction diagrams which form a basic motivation for this search.

Fig. 6 The experimental apparatus including four trigger counter banks (A,B,C,D), sixteen modules of liquid scintillator ionization calorimeter, eight wide gap optical spark chambers (WGSC), and a toroidal iron core magnet.

Fig. 7 An example of a charged current neutrino interaction showing (a) its position in the apparatus, (b) the corresponding pulse height distribution in the sixteen calorimeter channels, (c) the track pattern in the WGSC.

Fig. 8 A photograph of a neutrino interaction showing a hadronic shower in the upstream chambers and no muon in the spectrometer chambers. This is a signature for neutral interactions.

Fig. 9 Same as Fig. 8.

Fig. 10 Errors in the vertex measurement technique used to make fiducial volume restrictions. These errors were measured by using charged current events with fully reconstructed muons. The interaction vertex was determined by projecting the muon momentum vector and the hadron shower tracks back to the Z plane of the vertex. The error was the difference between the two measurements.

Fig. 11 Probability for a hadron to penetrate to muon detector MU1 as a function of the energy transfer E_H.

Fig. 12 Probability for a hadron to penetrate to muon detector MU1 as a function of the Z coordinate of the interaction vertex. The restriction on energy transfer of $E_H < 40$ GeV has been applied.

Fig. 13 Results of the corrections made to the observed ratio of neutral to charged events.

Fig. 14 Measured angular errors in the Y-Z($\Delta\theta_Y$) and X-Z($\Delta\theta_X$) planes for muon tracks measured in WGSC4.

Fig. 15 Measured angular errors in the Y-Z($\Delta\theta_Y$) and X-Z($\Delta\theta_X$) planes for hadron tracks measured in WGSC4.

Fig. 16 Geometric acceptance (detection efficiency) as a function of the muon polar angle θ for the three detectors.

Fig. 17 Observed, corrected, and calculated muon angular (θ) distributions for the E_p= 300 GeV (α= .62) run.

Fig. 18 Observed, corrected, and calculated muon angular (θ) distributions for the E_p= 400 GeV (α= .94) run.

Fig. 19 Maximum muon momentum (P_μ) as a function of the muon polar angle θ for various incident neutrino energies E. The kinematic limit is reached in the case of quasielastic scattering ($\nu_\mu N \rightarrow \mu^- P$). For θ > 350 mr the limit is independent of E.

Fig. 20 Observed and calculated muon momentum (P_μ) distributions for fully reconstructed $\nu_\mu(\mu^-)$ events from the E_p= 300 GeV run.

Fig. 21 Observed and calculated muon momentum (P_μ) distributions for fully reconstructed $\bar{\nu}_\mu$ (μ^+) events from the E_p= 300 GeV run.

Fig. 22 Observed and calculated muon momentum (P_μ) distributions for fully reconstructed ν_μ (μ^-) events from the E_p= 400 GeV run.

Fig. 23 The corrected value of R obtained with the MU2 detector as a function of the transverse position (X,Y) of the interaction vertex for the E_p= 300 GeV (α=.62) run. Also shown is the detection efficiency (ε_μ).

Fig. 24 Same as Fig. 23 for the E_p= 400 GeV (α=.94) run.

Fig. 25 The corrected value of R obtained with the MU2 detector as a function of the longitudinal position (Z) of the interaction vertex for the E_p= 300 GeV (α= .62) run. Also shown is the detection efficiency (ε_μ).

Fig. 26 Same as Fig. 25 for the E_p= 400 GeV (α= .94) run.

Fig. 27 The corrected value of R obtained with the MU2 detector as a function of the energy transfer E_H for the E_p= 300 GeV (α= .62) run. The theoretical variation of R with E_H for primitive neutral currents with V-A, V+A, V or A structure is also shown. The theoretical curves have been normalized to produce the observed average R.

Fig. 28 Same as Fig. 27 for the E_p= 400 GeV (α= .94) run.

Fig. 29 The distribution of neutral events as a function of the observed energy E_H is shown. The corresponding distribution for charged events is the incident neutrino energy (E) spectrum. The difference between these curves is evidence that the neutral events are not highly inelastic ($y \sim 1$, $E_H \sim E$, θ>480 mr) charged current events with undetected muons, but rather, events in which large fractions of the total energy escape in the form of undetected neutrinos. Data are from the combined E_p= 300 GeV and E_p= 400 GeV runs (average α= .82).

Fig. 30 The corrected ratio R of neutral to charged events for the three muon identifiers as obtained with the E_p= 300 GeV (α= .62) data. The different geometric acceptances are due in part to the distances Z from the target as expressed in meters. The differences in hadron penetration probabilities are due to the distances Z from the target as expressed in radiation lengths or nuclear collision lengths. Within the statistics, the measured values of R agree for the three detectors.

Fig. 31 The same as Fig. 30 except that the values of R were obtained with the E_p= 400 GeV (α= .94) data.

Fig. 32 Observed and corrected distributions of total energy E for ν_μ (μ^-) events from the E_p= 300 GeV run.

Fig. 33 Observed and corrected distributions of total energy E for $\bar{\nu}_\mu$ (μ^+) events from the E_p= 300 GeV run.

Fig. 34 Observed and corrected distributions of total energy E for ν_μ(μ^-) events from the E_p= 400 GeV run.

Fig. 35 Observed and corrected distributions of total energy E for $\bar{\nu}_\mu$(μ^+) events from the E_p= 400 GeV run.

Fig. 36 Observed and calculated muon polar angle (θ) distributions for fully reconstructed ν_μ(μ^-) events from the E_p= 300 GeV run.

Fig. 37 Observed and calculated muon polar angle (θ) distributions for fully reconstructed $\bar{\nu}_\mu(\mu^+)$ events from the E_p= 300 GeV run.

Fig. 38 Observed and calculated muon polar angle (θ) distributions for fully reconstructed $\nu_\mu(\mu^-)$ events from the E_p= 400 GeV run.

Fig. 39 Observed and calculated energy transfer (E_H) distributions for fully reconstructed $\nu_\mu(\mu^-)$ events from the E_p= 300 GeV run.

Fig. 40 Observed and calculated energy transfer (E_H) distributions for fully reconstructed $\bar{\nu}_\mu(\mu^+)$ events from the E_p= 300 GeV run.

Fig. 41 Observed and calculated energy transfer (E_H) distributions for fully reconstructed $\nu_\mu(\mu^-)$ events from the E_p= 400 GeV run.

Fig. 42 Calculation of the ratio of antineutrino ($\bar{\nu}_\mu$) to neutrino (ν_μ) events and of the mixing parameter α. The numbers are obtained from the corrected energy spectra of Fig. 32-35.

Fig. 43 Diagrams for possible sources of the observed neutral interactions including production of charged intermediate vector bosons W, nonconservation of muon number, production of new heavy leptons, and primitive weak neutral current interactions.

Fig. 44 Cross section for production of charged intermediate vector bosons by neutrinos as a function of neutrino energy E and boson mass M_W.

Fig. 45 The ratio $R_W = \sigma(\nu_\mu N \to W^+\mu^-)/\sigma(\nu_\mu N \to \mu^- + \text{hadrons})$ averaged over the incident energy spectrum for the $E_p = 400$ GeV ($\alpha = .94$) run and shown for W masses $M_W = 3, 5, 7, 10$ GeV/c^2. If the entire observed neutral signal were due to W production then $R = R_W$ and $M_W = 3.2 \pm .2$ GeV/c^2.

Fig. 46 The ratio R_L of heavy lepton (L) production to light lepton (μ) production as a function of neutrino energy E for L masses $M_L = 2, 4, 6$ GeV/c^2.

Fig. 47 The ratio R_L of heavy lepton (L) production to light lepton (μ) production averaged over the incident energy spectrum for the $E_p = 300$ GeV ($\alpha = .62$) run and shown as a function of the L mass M_L. If the entire observed neutral signal were due to L production then $R = R_L$ and $M_L = 3.2 \pm .4$ GeV/c^2.

Fig. 48 Same as Fig. 47 for the $E_p = 400$ GeV ($\alpha = .94$) run. The appropriate mass for $R = R_L$ is $M_L = 2.8 \pm .3$ GeV/c^2.

Fig. 49 Plot of the ratios of neutral to charged cross sections for neutrinos (R^ν) and antineutrinos ($R^{\bar{\nu}}$). The solid lines enclose the one standard deviation regions (statistical errors only) allowed by the two experiments discussed here. Systematic errors in the computation of R could shift the location (but not the width) of

these bands by .03. The dashed lines show the theoretical predictions for various space time properties of the neutral current. The curved axis shows the values predicted by the Weinberg-Salam model as a function of the parameter $w = \sin^2\theta_W$.

Fig. 50 The corrected value of R obtained with the MU2 detector as a function of the energy transfer E_H for the E_p= 400 GeV (α= .94) run. The theoretical variation of R with E_H as predicted by the Weinberg-Salam model is shown for several values of the parameter $w=\sin^2\theta_W$.

Fig. 51 Layout of Fermilab showing a section of the proton synchrotron, the extraction switchyard, proton target, hadron drift region, muon shield, and neutrino detector.

Fig. 52 Electronics for the ionization calorimeter used for pulseheight recording and event triggering.

Fig. 53 Response of a single calorimeter module to high energy muons incident at small angles.

Fig. 54 Variation of the response of a single calorimeter module over the active area. The improvement of twelve tubes over one tube is shown as well as the improvement due to the teflon over a $1/R^2$ variation. Units are pulse height analyzer channel number.

Fig. 55 Correction of visible energy E_{vis} to incident pion energy E_π from a calibration measurement using pion beams of known energy.

Fig. 56 Observed distributions in visible energy E_{vis} for incident pion beams of energy 14.7, 19.8, 24.6, 34.6, 49.5, 73.4, 97.3, 123.1, 146.1 GeV.

Fig. 57 Marks generator and clearing field circuits for WGSC.

Fig. 58 WGSC delay curves expressed as efficiency for producing a track as a function of the delay in triggering the Marks generator. Data are shown for clearing fields of 0, 200, and 470 volts/cm.

Fig. 59 Magnetic spectrometer showing four iron core toroidal magnets with gaps for inserting Hall generator probes.

Fig. 60 Magnetization function for the steel used in the spectrometer.

Fig. 61 Variation of the B field with the radius R in the magnet calculated analytically by assuming circular field lines in the steel and numerically using the computer program TRIM.

Fig. 62 Measurements of the magnetic field component normal to the vertical and horizontal gaps. The solid line shows the calculated field derived from Fig. 61.

Fig. 63 Schematic arrangement of liquid scintillation counter banks A, B, D.

Fig. 64 Electronics for trigger counter banks A, B, D. For A the mean timing circuit is replaced by a coincidence circuit.

Fig. 65 Schematic arrangement of plastic scintillation counter bank C.

Fig. 66 Electronics for trigger counter bank C.

Fig. 67 Noise immune circuit for advancing the frame number solenoid.

Fig. 68 Equivalent end view of the $\pm 7.5^{o}$ and 90° optical system obtained by unfolding all mirror reflections.

Fig. 69 Mirror arrangement for 90° optical system used for viewing WGSC 1-4.

Fig. 70 Mirror arrangement of $\pm 7.5^{o}$ optical system used for viewing WGSC 1-8.

Fig. 71 Observed distributions in momentum for incident muon beams of nominal momentum (P_{NOM}) 20, 35, 70, 100, 125 GeV/c.

Fig. 72 Electronic logic used for triggering the apparatus, recording pulse height and counter information, and operating the computer and optical recording system.

Fig. 73 Measured efficiency of the calorimeter threshold discriminator as a function of the energy transfer E_H for neutrino events.

Fig. 74 Noise immune circuit for sequencing the camera advance.

I. INTRODUCTION

The subject of this paper is a search for a weak neutral current in semileptonic interactions. The motivation for this search has its roots in the very earliest studies of the weak interactions via beta decay of unstable nuclei. In 1930, W. Pauli proposed the existence of the neutrino[1] (which he called the neutron) to explain the continuous beta emission spectrum, i.e., he suggested that the decay reaction proceeded via

$$(A,Z) \rightarrow (A,Z+1) + e^- + \bar{\nu}$$

rather than

$$(A,Z) \rightarrow (A,Z+1) + e^-$$

which experiment showed would violate energy conservation. Based on Pauli's suggestion, E. Fermi composed a theory of weak interactions[2] in analogy with electromagnetism. He proposed a weak Lagrangian density which, in present day notation, is the product of two currents[3]

$$L = J_H^\dagger J_L .$$

The currents J are Lorentz covariant bilinear combinations of field operators for the various particles involved in the interactions. In the case of beta decay discussed by Fermi,

$$J_L = \bar{\psi}_e \, \theta_L \, \psi_{\nu_e} \equiv (e\nu_e)$$

$$J_H \equiv \bar{\psi}_p \, \theta_H \, \psi_n \equiv (pn)$$

where θ_L and θ_H are Dirac gamma matrices determining the space-time properties of the currents.

The current (pn) corresponds to the destruction of a neutron and the simultaneous creation of a proton. The current ($e\nu_e$) corresponds to the simultaneous creation of an electron and an antineutrino.

Subsequent discoveries of additional weakly interacting particles have resulted in the inclusion of other currents in the theory. Today the Langrangian is written $L=J^{\dagger} J$ where $J=J_H+J_L$. The current J_H contains hadron or quark fields, and the current J_L contains lepton fields. The lepton current J_L has been expanded only to include the muon current ($\mu\nu_\mu$). The hadron current, however, has been modified to account for the many weakly interacting hadrons. With this expansion of the currents, the basic form of the interaction and its analogy to electromagnetism have remained unchanged.

One of the puzzling aspects of weak interactions is the fact that they appear to depend on the electromagnetic charge of the particles involved. For example, two electrons can interact electromagnetically by exchanging a (neutral) photon (Fig. 1). However, two electrons cannot interact weakly (to lowest order) because ($e\nu_e$) is a charged current. If two electrons are to interact weakly, then the interaction must proceed via a weak neutral current (ee) and can be envisioned as the exchange of a neutral boson (Fig. 1). Similar analogies and the idea that weak interactions should be universal suggest the existence of ($\mu\mu$), ($\nu_\mu\nu_\mu$) and ($\nu_e\nu_e$).

To search for weak neutral currents, one first turns to particle decays. The particles most easily produced are π mesons. Since muons and electrons are the only charged particles lighter than pions, the final state of a charged π decay must contain a μ or e of the same charge, i.e., $\pi^+ \rightarrow \mu^+ + \nu_\mu$ or $\pi^+ \rightarrow e^+ + \nu_e$. These reactions involve $(\mu\nu_\mu)$ and $(e\nu_e)$. The π^o must decay into a final state which is neutral. The decay $\pi^o \rightarrow \mu^+\mu^-$ is forbidden since the μ mass is so close to the π mass. The decays $\pi^o \rightarrow \nu_\mu \bar{\nu}_\mu$ and $\pi^o \rightarrow \nu_e \bar{\nu}_e$ would be unobservable and would violate conservation of angular momentum. No attempts to observe the decay $\pi^o \rightarrow e^+e^-$ have been reported.

Since pions provide no avenues for neutral current searches, K-mesons were used. Charged kaons can decay into charged pions plus a neutral lepton pair. Neutral kaons can decay into neutral lepton pairs with or without neutral pions (see Fig. 2 for a list of possible decays). Searches have been made for six kaon decay modes involving weak neutral leptonic currents. The results are given in Fig. 3. The $K^o_L \rightarrow \mu^+\mu^-$ decay has yielded a possible signal with six events observed by a Columbia-CERN-NYU[7] group. This result is in disagreement with an earlier limit set by an LRL[5] group. Recently the observation of 24 events ascribed to $K^+ \rightarrow \pi^+e^+e^-$ has been reported by a Saclay-Geneva[4] collaboration. The observed rates for these decays are consistent with higher order electromagnetic decay.

The failure to observe the decays listed in Fig. 3 at rates comparable to charged current decay rates does not necessarily rule out the existence of weak neutral leptonic currents. Instead, some other mechanism such as the absence of a $\Delta S=1$ $\Delta Q=0$ hadronic current may prohibit these modes.

Attempts to study weak interactions by utilizing particle collisions are generally unsatisfactory due to the presence of strong and electromagnetic forces. These problems are overcome in interactions of neutrino beams since the neutrino interacts only via the weak force. At the very lowest energies (Fig. 4) the Irvine[10] group has searched at the Savannah River reactor for the neutral currents ($\nu_e\nu_e$) and (ee) through the leptonic interaction $\bar{\nu}_e e^- \rightarrow \bar{\nu}_e e^-$ and the semi-leptonic interaction $\bar{\nu}_e d \rightarrow np\bar{\nu}_e$. While they have observed no signal, they are severely hampered by low event rates ($\sim$1 event per day) and large reactor induced backgrounds. In the GeV range, the CERN[11], Columbia-BNL[12], and CERN-Gargamelle[13] groups have produced negative results for the neutral channels $\nu_\mu p \rightarrow \nu_\mu p$, $\nu_\mu p \rightarrow \nu_\mu n\pi^+$, $\nu_\mu p \rightarrow \nu_\mu p\pi^o$, $\nu_\mu n \rightarrow \nu_\mu n\pi^o$. These results depend heavily on poorly known corrections due to neutron and photon backgrounds and suffer from particle recognition problems. The CERN group makes a further correction due to carbon events (as opposed to free proton events) in propane equal to 50% of the observed rate. The π^o searches are hampered by charge exchange in the aluminum target. These problems make interpretation of the cross section limits difficult.

Neutrino-nucleon interactions become more tractable when the

incident neutrinos attain energies high enough to permit large statistics experiments. At these energies one is able to study the inclusive reactions $\nu_\mu N \to \nu_\mu +$ hadrons and $\bar{\nu}_\mu N \to \bar{\nu}_\mu +$ hadrons which are analogous to inclusive electroproduction reactions (Fig. 5). These experiments make the investigation independent of the various backgrounds and corrections which plague the lower energy experiments.

Recent results published by the CERN-Gargamelle[14] collaboration have indicated a positive signal for the neutral inclusive reactions. This experiment was carried out in a heavy liquid bubble chamber situated in the CERN neutrino beam (Fig. 4). While the evidence provided by this experiment is strong, the interpretation of the measurement is affected by several problems. A 15% correction was applied to the data to account for neutral particles other than neutrinos interacting in the liquid. An unknown correction must be made to account for particles other than muons appearing to be muons by exiting the chamber. Any muon which stopped within the physical volume occupied by the hadron shower might not be observed to decay. Finally, the kinematic constraint of visible energy in the shower ≥ 1 GeV provides a strong bias since the CERN neutrino spectrum lies primarily below 4 GeV.

The possibility of searching for weak neutral currents in the Fermilab energy range provides a completely different experimental environment in which to work. Problems of muon identification and neutron and photon backgrounds are handled in a different manner.

Kinematic constraints no longer play a significant role. Furthermore, with the apparatus described later, it is possible not only to measure the magnitude of the neutral signal but to study its properties.

II. PHYSICAL MODEL OF NEUTRINO INTERACTIONS

The variables of neutrino-nucleon interactions consist of the four-vector momenta of the incident neutrino ($\underline{P}$), the target nucleon ($\underline{P}_N$), the outgoing lepton ($\underline{P}_1$), and the hadronic final state ($\underline{P}_H$). We define the four-momentum transfer as $\underline{Q}=\underline{P}-\underline{P}_1=\underline{P}_H-\underline{P}_N$. From these momenta we can define only three independent Lorentz invariant scalar variables[15]: $\underline{P}_N \cdot \underline{P}=ME$, $\underline{P}_N \cdot \underline{Q}=ME_H \equiv \nu$, and $|\underline{Q}\cdot\underline{Q}|=q^2=2EE_1(1-\cos\theta)$ where:

M = nucleon mass

E = incident neutrino energy

E_H= energy transferred to the hadron system

E_1= final state lepton energy

θ = lepton scattering angle.

From these, one can define two dimensionless variables: $y=E_H/E$ and $x=q^2/2ME_H=q^2/2\nu$.

J. D. Bjorken and E. A. Paschos[16] have derived the differential cross section for neutrino-nucleon interactions. They used the V-A theory (vector minus axial vector) proposed by R. P. Feynman and M. Gell-Mann[17]. With the approximations that $E_H \gg 2M \approx 2$ GeV, and $q^2 \ll E_H^2$, the neutrino cross section is

$$\frac{d^2\sigma^\nu}{dxdy} = \frac{G^2M}{\pi} E F_2[L+(1-y)^2R+2(1-y)S]$$

where F_2,L,R, and S are functions of q^2 and ν. The antineutrino cross section is obtained by interchanging L with R. L,R, and S are bounded such that $0 \leq L,R,2S \leq 1$ and $L+R+2S=1$. The cross section was further simplified by Bjorken[18] with the introduction of the

scaling hypothesis. The scaling hypothesis states that there are no masses associated with the weak interactions. This implies that F_2,L,R, and S, all of which are necessarily dimensionless, must be functions of dimensionless variables, i.e., $F_2(q^2, \nu)=F_2(x)$, $L=L(x)$, $R=R(x)$, $S=S(x)$. With this, one can easily show that the ratio of total cross sections $\sigma^{\bar{\nu}}/\sigma^{\nu}$ is bounded by $1/3 \leq \sigma^{\bar{\nu}}/\sigma^{\nu} \leq 3$. Actual measurements of this ratio[19,20] for charged current interactions are consistent with the lower bound of $\sigma^{\bar{\nu}}/\sigma^{\nu}= 1/3$ up to $E \approx 80$ GeV. The lower bound implies L=1 and R=S=0. The resultant differential cross sections can therefore be written

$$\frac{d^2\sigma^{\nu}}{dxdy} = \frac{G^2M}{\pi} E\, F_2(x)$$

$$\frac{d^2\sigma^{\bar{\nu}}}{dxdy} = \frac{G^2M}{\pi} E\, F_2(x) \cdot (1-y)^2$$

If the neutral current enters the Lagrangian in the same way as the charged, i.e., with coupling constant G^2 and structure V-A, then these differential cross sections will hold for the neutral interactions. On the other hand, one might expect that if the analogy between weak and electromagnetic interactions implied some deep symmetry, then both neutral currents might be expected to have the same form, i.e., V. The resulting weak neutral cross sections would be

$$\frac{d^2\sigma_o^{\nu}}{dxdy} = \frac{d^2\sigma_o^{\bar{\nu}}}{dxdy} = \frac{G^2M}{\pi} E\, F_2(x) \left[\frac{1 + (1-y)^2}{2}\right]$$

and $\sigma_o^{\bar{\nu}}/\sigma_o^{\nu} = 1$. The same cross sections would apply for A.

Should the weak neutral current have a V + A structure, then the neutrino and antineutrino would switch roles implying

$$\frac{d^2\sigma_o^{\nu}}{dxdy} = \frac{d^2\sigma^{\bar{\nu}}}{dxdy}$$

$$\frac{d^2\sigma_o^{\bar{\nu}}}{dxdy} = \frac{d^2\sigma^{\nu}}{dxdy}$$

and $\sigma_o^{\bar{\nu}}/\sigma_o^{\nu} = 3$.

III. DATA COLLECTION

The data discussed here were obtained during two of a series of five experiments[21] done by the Harvard-Pennsylvania-Wisconsin-Fermilab (HPWF) collaboration. The experiments were designed to search for the neutral leptonic current ($\nu_\mu \nu_\mu$) via the interactions $\nu_\mu + N \rightarrow \nu_\mu +$ hadrons and $\bar{\nu}_\mu + N \rightarrow \bar{\nu}_\mu +$ hadrons. The neutrino beams for these experiments were created by protons extracted from the Fermi National Accelerator Laboratory (Fermilab) synchrotron. Hadrons (predominantly π and K mesons) produced by interactions of the proton beam in an aluminum target were then focused to enhance the flux of neutrinos or antineutrinos produced by meson decays in a 340 m evacuated drift region. All particles other than neutrinos were then stopped by a 900 m earth and steel shield. The neutrinos and antineutrinos entered a target-detector (Fig. 6) consisting of sixteen ionization calorimeter modules filled with liquid scintillator. Charged particles entering the detector were vetoed by trigger counter A located just upstream of the calorimeter. Interactions in the liquid triggered the apparatus when ionization energy deposited in the calorimeter by the emerging hadrons exceeded a threshold value. The trigger was used to initiate recording of the calorimeter pulse height and to fire optical widegap spark chambers (WGSC) located downstream of every fourth calorimeter module. The hadron shower was then photographed in the WGSC. Any part of the hadron shower emerging from calorimeter module 16 was absorbed by a 35 cm thick steel shield before it could reach WGSC4.

When a neutrino or antineutrino interacted through the charged current ($\mu\nu_\mu$) , the final state muon generally emerged from the calorimeter and steel shield. The muon then traversed a magnetic spectrometer consisting of four iron core toroidal magnets each followed by a WGSC. Eighteen scintillation counters assembled into three banks (B,C,D) were located within the spectrometer. The muon was observed in any of the chambers or counters it traversed. Charged current interactions could therefore be distinguished from neutral current interactions by the observation of a muon downstream of the calorimeter. In both cases the hadron energy transfer (E_H) could be determined from pulse height measurements within the calorimeter. For charged current interactions the final state lepton (muon) momentum ($\underline{P}_l$) was measured in the spectrometer and the incident neutrino energy was determined as $E=E_H+E_l$. A typical charged current interaction is shown in Fig. 7 with the corresponding pulse height distribution. Fig. 8 and 9 show neutral current interactions, i.e., neutrino interactions with no observed muon.

The five experiments in this series were carried out during the period May 1973 to March 1974. They are distinguished from each other primarily by different incident neutrino beams. The extracted proton energy was either 300 GeV or 400 GeV. The neutrino and antineutrino spectra are shifted towards higher energies for the higher proton energies providing the possibility for any threshold effects to appear differently for different experiments.

Different hadron focusing systems were used to alter the energy spectra, increase the flux, and change the mixture of neutrinos and antineutrinos incident on the detector. This provided the possibility for distinguishing differences between neutrinos and antineutrinos interacting through a neutral current.

The first experiment was done with extracted protons of both 300 GeV and 400 GeV but no focusing of the secondary hadrons was provided. The result of this beam configuration was that the fraction of the charged current events due to neutrinos[22] (α) was $\alpha=.83\pm.02$. An earlier version of the spectrometer was used which employed smaller chambers and counters located farther from the target (calorimeter). This resulted in a low and poorly measured acceptance for the final state muons of charged current interactions introducing an uncertain background of charged current events with unobservable muons simulating neutral current events.

The data presented here are the product of the next two experiments which were run after modifying the spectrometer to the configuration described here. The first of these was run with extracted proton energy of 300 GeV. The secondary hadrons were focused by a magnetic horn with polarity set to enhance the flux of negative hadrons. This in turn resulted in an antineutrino flux enhanced with respect to the unfocused beam. The fraction of charged current events due to neutrinos was $\alpha=.62\pm.03$ for the 300 GeV horn focused experiment. The following experiment was run with extracted proton energy of 400 GeV. Secondary hadrons were focused

by the same magnetic horn but with the polarity set to enhance positive hadrons. The result of this beam configuration was an almost completely pure neutrino beam. The measured value of α was $\alpha = .94 \pm .01$. These two experiments together provide a neutral current search in a pure neutrino beam and a mixed neutrino-antineutrino beam allowing one to measure the results obtainable from neutrinos and antineutrinos independently.

The final two experiments in the series were run with extracted proton energy of 300 GeV. Secondary hadrons were focused by a series of quadrupole and dipole magnets[23] designed to select hadrons of one sign. This resulted in beams for the two experiments characterized by $\alpha = .12 \pm .05$ and $\alpha = .98 \pm .01$ respectively. The magnet configuration also reduced the particle flux and restricted the neutrino and antineutrino energies to lie primarily in the range $20 \leq E \leq 80$ GeV. The sign selection allowed neutral current searches to proceed in relatively separated neutrino and antineutrino beams but the reduced flux limited the statistics.

IV. EVENT SELECTION AND DATA ANALYSIS

The film obtained with the 300 GeV and 400 GeV horn focused beams was scanned with a loose selection criterion to obtain a set of event candidates. Any event which produced two or more tracks in WGSC 1,2, or 3, was considered a candidate. The tracks were then projected upstream to obtain the location of the interaction vertex (Fig. 10). Candidates whose vertex could not be located in all three stereo views were rejected. For the surviving events, the number of tracks in each WGSC was recorded. The further requirement that the vertex coordinate along the beam line (Z) agree with the pulse height measurements made in the calorimeter modules was applied. An additional requirement was applied to insure against bias in favor of charged current events. The threshold discriminator was found to be fully efficient for energy transfers above 4 GeV (Fig. 73). This requirement was therefore applied to all the data.

Film from the 300 GeV run was first scanned by physicists and then rescanned by non-physicist scanners. 95% of the events found by physicists were also found by scanners. Film from the 400 GeV run was first scanned by scanners. Each candidate was then examined by physicists to check the application of scanning criteria. This resulted primarily in identifying sparks which were unrelated to the observed events. Unrelated sparks were due to charged particles entering the apparatus during the >10 μs memory time of the WGSC (clearing fields had not yet been installed). These sparks

were easily distinguished from related sparks due to their physical displacement from the interaction, lower light output, and non-linearity (due to drifting and recombination of the ions).

Once a set of events was obtained in this way for each experimental run, it was divided into two categories. Events were termed charged current (C) if a muon was detected. Events were termed neutral current (N) if no muon was detected. Three corrections had to be applied to the data. Low energy muons which ranged out before detection, or wide angle muons which missed the detector produced no muon signal and tended to shift events from C to N. Energetic hadrons which penetrated the absorbers protecting the muon detectors produced a false muon signal and tended to shift events from N to C.

As a check on systematic errors in the application of these corrections, the analysis was done in three ways. In one analysis (MU1), observation of a muon was determined by a count in counter B^{24}. The large size of MU1 and its proximity to the target minimized the corrections due to low energy and wide angle muons but resulted in the largest correction due to hadron penetration. In the second analysis (MU2), observation of a muon was determined by a count in counter C or a track in WGSC5. The separation of MU2 from the target increased the corrections due to missed muons. However, as shown below, the 74 radiation lengths and 12 interaction lengths provided by the first magnet eliminated the correction due to penetrating hadrons. In the third analysis (MU3),

observation of a muon was determined by a track in WGSC4. The smaller size of MU3 increased the correction for wide angle muons and reduced the number of penetrating hadrons. Also, the ability to measure the direction of the momentum vector of particles seen in MU3 provided a technique, described below, for separating hadrons from muons.

For the MU1 detector, the probability for a hadron to penetrate was measured by using a sample of charged events detected in MU1 and MU2. Of these events, the fraction which had more than one counter in the B bank trigger or which had an excessively large pulse height in B with only one counter in the bank triggering was measured as a function of the energy transfer E_H (Fig. 11). Because of the high probability for hadrons from large E_H events simulating muons in the MU1 detector, a cut was placed on events for the MU1 analysis of E_H<40 GeV. After applying this additional constraint we have plotted the penetration probability as a function of the vertex location Z in Fig. 12. The events in the MU1 analysis must then be corrected according to these measurements. The results are shown in Fig. 13.

A measure of the number of hadrons which penetrate to MU2 was obtained by searching for events with two or more apparent[25] muons. No events were found.

For the MU3 detector, penetrating hadrons were distinguished from muons by requiring muon tracks in MU3 to extrapolate back to the interaction vertex. A sample of 558 events have tracks seen

both in MU3 and WGSC5 and are therefore guaranteed to be muons. By measuring 306 of these tracks, it was found that .93±.02 of the muons extrapolate back with projected angular errors in the X-Z and Y-Z planes of less than 100 mr (Fig. 14). The width of this distribution is due to multiple scattering (20 mr for 4 GeV muons), vertex measurement errors (20 mr r.m.s.), and track reconstruction errors (30 mr r.m.s.). By measuring a sample of 164 events which have two or more tracks in WGSC4, one of which must be a hadron (delta rays have been excluded), it was found that only .24±.04 of the hadrons artificially satisfy the 100 mr constraint (Fig. 15). The C events for the MU3 detector are then divided into two classes. Those with tracks also visible in WGSC5 are assured of being muons and need no correction. The C events without a track in WGSC5 were all measured and the extrapolation errors calculated. Using the measured probabilities for muons and hadrons satisfying the 100 mr constraint, these C events were then reclassified as having muons (C) or penetrating hadrons (N). The results of analyzing the events in this way are shown in Fig. 13. This procedure was repeated using a 60 mr angular error constraint. The probability for hadrons to satisfy the constraint is reduced to .11±.03. For the muons, .75±.03 satisfy the constraint. The corrected numbers of neutral and charged events using these values agree with the previous ones within less than one standard deviation.

For the MU1 and MU3 analyses, the acceptance (ε_μ) for wide angle muons was purely geometric. Assuming azimuthal symmetry for

the final state muons, the acceptance of MU1 and MU3 as a function of the polar angle θ was calculated for each point within the target. The angular acceptance, averaged over the fiducial volume, is shown in Fig. 16. The measurements in MU3 discussed in the previous paragraphs yield directly the observed angular distribution shown in Fig. 17 and 18. Using the calculated geometric acceptance and the observed angular distribution, we obtained the corrected angular distribution for $\theta \leq 480$ mr, shown in Fig. 17 and 18. From Fig. 17 and 18, we calculated the probability for detecting muons (the detection efficiency) produced at angles $\theta \leq 480$ mr. For angles $\theta > 480$ mr the detection efficiency was too low for this calculation. Consequently, a monte carlo calculation (see section VI) was done which estimated the fraction of muons produced at $\theta > 480$ mr to be .06±.005 for the 400 GeV run and .04±.005 for the 300 GeV run. The resulting detection efficiency over all angles is given in Fig. 13 for the various detectors. The monte carlo calculation can be seen to reliably predict the corrected angular distribution for $\theta \leq 480$ mr in Fig. 17 and 18.

For the MU2 analysis, a similar calculation was done. In this case, the monte carlo was also needed to estimate the effect of the magnetic focusing of the first magnet. This changed the value of the detection efficiency by <.01 when averaged over the data. For both analyses, the effect of multiple Coulomb scattering on the detection efficiency was calculated to be <.005.

The correction for low energy muons which ranged out before detection could only be made using the monte carlo calculation.

This correction, however, turned out to be quite small for two reasons. The average range cutoff for MU1 and MU3 was 1.2 GeV and for MU2 it was 2.4 GeV. The median muon energy, however, was measured to be 30 GeV or 25 (or 12) times the cutoff, suggesting a small effect. Secondly, all models of neutrino interactions imply a strong correlation between the energy and angle of the final state muon. This is in large part aided by the kinematics of Lorentz transformations which enforce a maximum momentum (and therefore energy) at each angle as shown in Fig. 19. Consequently, most muons which ranged out were at angles such that they would not have been detected anyway. The result is a reduction of <.02 in detection efficiency which has been included in the calculation in Fig. 13. The reliability of this calculation can be seen in part by a comparison of the observed muon momentum distribution above 5 GeV/c with the monte carlo prediction in Fig. 20 -22.

After removing penetrating hadrons (none of MU2), and correcting for the average detection efficiencies, the resulting ratios R of neutral to charged events were calculated. For the 300 GeV run (mixed ν_μ and $\bar{\nu}_\mu$) R =.22±.04 and for the 400 GeV run (almost pure ν_μ) R=.32±.04. Except for the small kinematic constraint E_H>4 GeV, the ratio R is the ratio of cross sections $R=\sigma_o/\sigma$ averaged over the mixture of neutrinos and antineutrinos ($R=\alpha R^{\nu}+(1-\alpha)R^{\bar{\nu}}$) present in the beam.

To check on the sensitivity of these results to various geometric constraints we have plotted in Fig. 23 - 26 the ratios

and detection efficiencies for MU2 computed as described above, as functions of the transverse dimension of the fiducial volume and as functions of the calorimeter module number (Z). The ratios were seen to be independent of these variables within statistical fluctuations. Attempts to alter the results by making a large increase in the number of muons produced at angles $\theta>480$ mr force these muons all to lie below 7 GeV as shown in Fig. 19. This would cause a large discrepancy in the muon momentum distributions in Fig. 20 - 22. In addition, since the muons retain so little energy, the hadron energy transfer would be large ($y\simeq 1$ and $E_H \simeq E$) and the R would show a strong rise with E_H (Fig. 27 and 28). Furthermore, if $E_H \simeq E$ the distribution in the observed energy for the neutral events (E_H) would follow the incident spectrum of neutrino energy (E) (see Section VI). In Fig. 29, however, it is shown that the observed energy for neutrals falls rapidly above 20 GeV while the incident spectrum has a broad maximum at 30 GeV indicating that large amounts of energy are carried off by final state neutrinos for neutral events.

The use of the three different muon identifiers provides a further check on the systematic errors (Fig. 30 and 31). The MU2 identifier has moderate detection efficiency but involves no hadron penetration correction. The MU1 identifier is much closer to the target and so has very high detection efficiency but is subject to a significant hadron correction. The MU3 identifier provides a cross-check by using a different technique for removal

of penetrating hadrons with a sacrifice in detection efficiency. The fact that these three identifiers produce the same value of R within statistics even though the corrections differ greatly in magnitude and technique, provides convincing support for the validity of this result. We conclude from these various checks that systematic errors in R are around .03.

The two data sets discussed here produce results which differ by 2.75 standard deviations. Note, however, that the running conditions differed significantly. The incident proton energies were E_p= 300 GeV and E_p=400 GeV. Focusing of secondary hadrons produced by the protons favored neutrinos in the 400 GeV run and antineutrinos in the 300 GeV run and made significant changes in the ν_μ and $\bar{\nu}_\mu$ energy spectra. The implications of these differences are discussed in Section VII.

Previous results published by HPWF are in complete agreement with these data with the exception of the value R^ν=.13±.06 measured with the sign selected beam which is 3 standard deviations below the value reported here. The number of neutral current events for this measurement was sufficiently small (22), that this disagreement may only be a statistical accident.

V. BACKGROUNDS

Backgrounds consist of neutral particles entering the detector and interacting without producing final state muons. The most likely candidates are machine associated neutrons, photons, and electron neutrinos (ν_e). Cosmic rays do not contribute since no events were found in an equal time period of running with the accelerator off.

The radiation length in the liquid scintillator is about 50 cm or one calorimeter module. Therefore, photons entering the front of the detector would be damped by $e^{-10} \simeq 10^{-4}$ before reaching modules 11 and 12. Photons entering the sides of the detector would most likely enter at narrow angles to the beam line substantially increasing the attenuation from 140 cm (3 radiation lengths). For example, if the photons were incident at 20^0 the effective attenuation would be 9 radiation lengths. Sources of neutrons would have similar attenuation. The independence within statistical errors of the ratio R with respect to vertex location within the detector is evidence that neutrons and photons are not the source of the neutral events. In addition, since such neutral particles would most likely have low energy, the fact that the ratio R remains high at large E_H (Fig. 27 and 28) is further evidence against this background.

Electron neutrinos interacting within the detector would have a uniform spatial distribution. The electrons would be absorbed by the scintillator and the hadron absorbers. In addition, since the radiation length is so long and is comparable to the

nuclear interaction length, shower transition curves cannot be used to identify the final state electrons. One must instead depend on calculations of the production of ν_e. Charged π mesons have branching ratios of 10^{-4} into ν_e as compared to ν_μ so do not contribute to the flux. The branching ratio for $K^{\pm}\rightarrow\pi e\nu_e$ is .05 and for $K_L^0\rightarrow\pi e\nu_e$ is about .4 resulting in a ν_e flux on the order of .01 of the ν_μ flux. Thus, unless the production of K_L^0 is very large, the background due to ν_e is negligible.

VI. THE MONTE CARLO SIMULATION

Events were generated by the monte carlo at energy E with uniform spatial vertex distribution within the volume of the calorimeter. The energy transfer to the hadronic final state was determined on the basis of a uniform distribution in the variable y for neutrinos and a $(1-y)^2$ distribution for anti-neutrinos. The polar angle of the muon was then determined using the nucleon structure function $F_2(x)$ which was obtained from measurements of electron-nucleon scattering[26]. Azimuthal symmetry was assumed. Each muon was then projected through the apparatus taking account of ionization energy losses, multiple Coulomb scattering, and magnetic focusing. The transverse coordinates at which the muon traversed the plane of each counter and WGSC were recorded.

From the events generated in this way, a subsample was selected of those events which could be completely reconstructed, i.e., those events which traversed three or more WGSC in the spectrometer. At each energy, one could therefore determine the fraction of final state muons which could not be reconstructed. The observed energy spectrum could then be corrected for this fraction (Fig. 32 - 35). The correction is smaller for $\bar{\nu}_\mu$ since the μ^+ on average retains a larger fraction of the incident energy than a corresponding μ^- produced by ν_μ. This forces the μ^+ to exit at small angles θ. The corrected energy spectrum was then used by the monte carlo to predict distributions for muon momentum,

muon polar angle, and hadron energy transfer. These were compared with the actual data in Fig. 20 - 22 and Fig. 36 - 41. In all cases, positive muons were attributed to antineutrinos and negative muons were attributed to neutrinos.

To obtain the ratio of antineutrinos to neutrinos in the beam the corrected distributions of Fig. 32 - 35 were used. The observed ratio of μ^+/μ^- (Fig. 42) was thereby corrected to a ratio of $\bar{\nu}_\mu$ events to ν_μ events of .07±.01 for the 400 GeV run and .62±.06 for the 300 GeV run. The μ^+ and μ^- angular monte carlo distributions were then mixed in this ratio to obtain the distributions of Fig. 17 and 18 and the corrections discussed in Section IV. Also, from the ratio of events the mixing parameter α is determined.

VII. POSSIBLE SOURCES OF NEUTRAL INTERACTIONS

While convincing evidence exists that wide angle muons are not the source of the neutral signal (see Section IV), it is still worthwhile to discuss possible sources of such wide angle muons. The production of a new particle, such as a charged intermediate vector boson (W), (Fig. 43), near threshold would distort the muon angular distribution. If the W production accompanied muons only at very wide angles and the decay mode $W \to \mu\nu_\mu$ were suppressed, then an apparent neutral signal would be the result. Cross sections for W^+ production have been calculated by R.W. Brown and J. Smith[27]. These are shown in Fig. 44 as a function of neutrino energy E. When averaged over the neutrino spectrum for the 400 GeV run (almost no anti-neutrinos) the ratio $R_W = \sigma(\nu_\mu + N \to W^+ + \mu^-)/\sigma(\nu_\mu + N \to \mu^- + X)$ $(X \neq W^+)$ as a function of the W mass is given in Fig. 45. If the entire neutral signal were due to W production, then $R = R_W$ and the W^+ mass would be 3.2±.3 GeV. Production of a W^0 utilizing its electromagnetic moments would involve a weak neutral leptonic current $(\nu_\mu \nu_\mu)$. Calculations of production cross sections as a function of the W^0 mass have not been made.

Previous searches for W bosons in neutrino interactions[28] have looked for the decay modes $W^+ \to \mu^+ \nu_\mu$ and $W^+ \to e^+ \nu_e$, the signature being the observation of two leptons of opposite charge in the final state. No positive signal has been observed. This places a lower limit on the W mass between 1.5 and 5.0 GeV depending on the branching ratio into the final state for which the search took

place. The production of a 3.2 GeV W which decays almost exclusively into final states without muons is in agreement with these previous measurements. The question of W production will be answered when it is possible to measure the angle and sign of very wide angle muons. This will increase the detection probability for final states with two muons and will extend measurements of x and y distributions almost to the kinematic limit where W production events will occur.

Since electrons can not be distinguished from hadrons in this apparatus, any neutrino interaction in which the final state lepton were an electron rather than a muon would be a source of an apparent neutral signal. The possibility of an anomalously large ν_e contamination was discussed earlier and is unlikely. If, on the other hand, the principle of total muon number conservation were to break down at high energies then the interaction $\nu_\mu + N \rightarrow e^- + X$ would be possible (Fig. 43). This could be expressed as a current of the type $(\nu_\mu e)$ with an energy threshold associated with its cross section. The question of electrons in the final state will be answered in bubble chambers where electrons can be easily identified or in counter experiments where electromagnetic transition curves can be distinguished from hadronic transition curves. However, since the electron would be absorbed the measured E_H would be $E_H = E$ and Fig. 29 makes this unlikely.

A third possible source of a neutral signal is the production of new heavier leptons (Fig. 43). Some spontaneously broken gauge

theories predict the existence of heavy leptons[29]. These leptons are members of symmetry groups with light leptons of different electrical charge but identical lepton and muon charge. Some models have charged heavy leptons, and some have neutral. It is also possible that the lepton families are just larger than two leptons per family and that there are higher mass states with the same electrical charge as the associated light leptons. These could be produced by currents of the form (Ll) where L is the new heavy lepton with charge +,-,0 and l is ν_e, ν_μ, e, or μ. Additionally, the heavy lepton currents might have the same transformation properties as light leptons (V-A) or they could be any linear combination of S,T,P,V, or A. If the current ($L\nu_\mu$) has a V-A structure, then the differential cross sections for producing heavy and light leptons are identical except for the lepton mass (M_L). When the lepton mass terms are retained the cross sections are[29]:

$$\frac{d^2\sigma^L}{dxdy} = \frac{G^2M}{\pi} E\, F_2\left(1-\frac{M_L^2}{xs}\right)^2$$

$$\frac{d^2\sigma^{\bar{L}}}{dxdy} = \frac{G^2M}{\pi} E\, F_2\left(1-\frac{M_L^2}{xs}\right)^2 (1-y)^2$$

over the kinematic range $0 \leq y \leq 1-\frac{M_L^2}{xs}$ and $x \geq \frac{M_L^2}{s}$. Integrating the neutrino cross section we calculate the ratio of total cross sections $R_L = \sigma(\nu_\mu N \to LX)/\sigma(\nu_\mu N \to \mu^- X)$ as a function of the neutrino energy (Fig. 46). Taking into account the mixture of neutrinos and antineutrinos and averaging over the energy spectrum, we

calculate R_L as a function of the lepton mass (Fig. 47 and 48). Heavy leptons would normally be expected to decay via two modes

$$L \to \mu + X$$

$$L \to \nu_\mu + X$$

If the muon decay mode were suppressed then the decay of the heavy lepton would produce an apparent neutral signal. In this case $R=R_L$. From Fig. 47 and 48 we see this implies a lepton mass, averaging over both data sets, of $3.1 \pm .5$ GeV/c^2. If the muon decay mode were not suppressed but had a branching ratio B, then $R=(1-B)R_L$ and a lower mass lepton would be needed to produce the entire neutral signal.

Recent searches for heavy leptons[30] have searched for the muon decay mode of the lepton. They are able to identify a heavy lepton only if it has electric charge opposite that of the muon. The signature they search for is a positive muon produced by

$$\nu_\mu + N \to L^+ + X, \; L^+ \to \mu^+ \nu_\mu \nu_\mu$$

amongst a sample of negative muons produced by the usual interactions $\nu_\mu + N \to \mu^- + X$. These searches are not able to distinguish the reaction $\nu_\mu + N \to L^- + X$, $L^- \to \mu^- + X$. Also, if the branching ratio B were lower than expected, the L^+ would not be detected as readily. Calculations of B and of the decay spectrum of the L^+ are heavily model dependent and use the as yet unmeasured asymptotic value of $K=\sigma(e^+e^- \to \text{hadrons})/\sigma(e^+e^- \to \mu^+\mu^-)$.

Another major problem with previous heavy lepton searches is the background due to $\bar{\nu}_\mu$ interactions which produce μ^+ final states. Since the level of such backgrounds is hard to measure and is always at least a few percent, it will be necessary to distinguish muon decay modes of heavy leptons by their effect on distributions of kinematic variables. If the leptons decay via $L \to \mu \nu_\mu \nu_\mu$ then the total observed energy is reduced producing an apparent enhancement at large y[31]. If the decay mode is $L \to \mu +$ hadrons or photons then the observed hadron energy transfer is increased producing enhancement at large y. Recent measurements of y distributions show such enhancement for anti-neutrino energies E>30 GeV[32] and may be signalling heavy lepton production. The apparent rise of R for E_H>60 GeV (Fig. 27 and 28) may be a companion signal for production of heavy leptons contributing part of the observed neutral signal.

All of the possible sources of the observed neutral signal discussed thus far are not true neutral currents (except L^0 or W^0 production) but are charged current interactions in which the final state lepton cannot be observed. The possibility of a neutral current $(\nu_\mu \nu_\mu)$ occurring as a third current in the weak Lagrangian is consistent with the observations we have made. If the structure of the $(\nu_\mu \nu_\mu)$ current were V-A and the coupling constant G_0^2 were equal to the Fermi coupling constant G^2 of the charged current $(\nu_\mu \mu)$, then the neutral and charged cross sections would be identical. This would imply R=1. The fact that R<1

could result from $G_0^2/G^2=R<1$, or it could be that the transformation properties of $(\nu_\mu \nu_\mu)$ are not (V-A). If, for example, the neutral current transformed as V+A, then the neutral cross sections would be:

$$\frac{d^2\sigma_o^\nu}{dxdy} = \frac{G_o^2 M}{\pi} E\, F_2(x) \cdot (1-y)^2$$

$$\frac{d^2\sigma_o^{\bar{\nu}}}{dxdy} = \frac{G_o^2 M}{\pi} E\, F_2(x)$$

This would mean that for neutrinos the ratio of neutral to charged cross sections would be $R^\nu=3$. If the $(\nu_\mu \nu_\mu)$ current transformed as the neutral electromagnetic current (V) or with opposite parity (A), then the neutral cross sections would be:

$$\frac{d^2\sigma_o^\nu}{dxdy} = \frac{d^2\sigma_o^{\bar{\nu}}}{dxdy} = \frac{G_o^2 M}{\pi} E\, F_2(x) \left[\frac{1+(1-y)^2}{2}\right]$$

and (assuming $G_0^2=G^2$) the ratios would be $R^\nu=2/3$ and $R^{\bar{\nu}}=2$. Similar calculations could be made for S,T, or P.

The observed value of R is a linear combination of R^ν and $R^{\bar{\nu}}$ according to $R=\alpha R^\nu+(1-\alpha)R^{\bar{\nu}}$ where α is the number of charged current neutrino interactions divided by the number of charged current neutrino interactions plus antineutrino interactions. It is determined, as discussed in Section VI, by correcting the observed number of μ^+ and μ^-. For the 300 GeV run, $\alpha=.62\pm.03$ and for the 400 GeV run $\alpha=.94\pm.01$. In Fig. 49 are shown predictions of the various options discussed above with no assumption about G_0^2.

as well as the one standard deviation regions (statistical errors only) derived from the measured values of R and α. V+A seems to be in substantial disagreement with the observations. V-A is in reasonably good agreement with both data sets. In this case the two data sets could be averaged giving a total neutral signal $R=R^{\nu}=R^{\bar{\nu}}=.28\pm.02=390$ (N)/1387(C).

A further test of the transformation properties of the neutral current results from the different $d\sigma/dy$ discussed above. Since the final state neutrino momentum cannot be measured, the only available kinematic variable is the energy transfer E_H. For any given $d\sigma/dy$, the dependence of R on E_H can be calculated. Fig. 27 and 28 show the results of this calculation with the coupling constant G_0^2 adjusted to produce the observed average R. The R dependence on E_H tends to favor the V+A cross sections. However, the disagreement with V-A, V, or A shapes is not compelling. The best fit to the data would be something in between V or A and V-A. To reliably determine the structure would require a large increase in statistics on the order of a factor of 40. It should be noted that any new particle production including intermediate vector bosons or heavy leptons would alter the R variation with E_H and change the nature of these preliminary conclusions. In particular, the R behavior for $E_H<60$ GeV is suggestive of other than V-A structure while the rise in R for $E_H>60$ GeV is suggestive of new particle production.

Neutral currents are also predicted by models of weak

interactions employing gauge fields to renormalize the theory. The simplest such model, proposed by S. Weinberg and A. Salam[33], has only one free parameter $0 \leq w \leq 1$. L. Sehgal[34] has calculated the cross sections for neutral currents (employing the same assumptions discussed in Section II) within the Weinberg-Salam model as:

$$\frac{d^2\sigma_o^{\nu}}{dxdy} = \frac{G^2M}{\pi} E F_2(x) [(\frac{1}{2} - w + \frac{5}{9} w^2) + \frac{5}{9} w^2(1-y)^2]$$

$$\frac{d^2\sigma_o^{\bar{\nu}}}{dxdy} = \frac{G^2M}{\pi} E F_2(x) [(\frac{1}{2} - w + \frac{5}{9} w^2)(1-y)^2 + \frac{5}{9} w^2]$$

Integrating these over x and y and dividing by the total cross sections for charged currents yields

$$R^{\nu} = (\frac{1}{2} - w + \frac{20}{27} w^2)$$

$$R^{\bar{\nu}} = (\frac{1}{2} - w + \frac{20}{9} w^2)$$

These ratios exceed only slightly the lower bounds calculated by Paschos and Wolfenstein[35],

$$R^{\nu} \geq (\frac{1}{2} - w + \frac{2}{3} w^2)$$

$$R^{\bar{\nu}} \geq (\frac{1}{2} - w + 2 w^2).$$

In Fig. 49, the allowed values of R^{ν} and $R^{\bar{\nu}}$ calculated by Sehgal are shown. Allowing for some systematic errors, the observations agree with Weinberg-Salam model predictions for $.1 \leq w \leq .4$ within 2 standard

deviations. The dependence of R on E_H (Fig. 50) tends to favor larger values of w near w=.9 but, within the statistics, the region of small w agrees well with the observations. Values of w in the region $.4 \leq w \leq .7$ are unlikely.

One further note should be made. There is no evidence to preclude the possibility that the observed neutral signal is due to a combination of effects. For example, neutral decays of 4 GeV heavy leptons would result in R_L=.13 in the 300 GeV run and R_L=.16 in the 400 GeV run. If there also were a V-A neutral current with coupling constant $G_0^2=.12G^2$, then the observed R would be R=.28 for E_p=400 GeV and R=.25 for E_p=300 GeV which is in agreement with the respective observed ratios R=.32±.04 and R=.22±.04. As indicated earlier, this may also prove to be the best explanation of the variation of R with E_H.

VIII. CONCLUSIONS

In the absence of any undiscovered sources of background, the observation of 390 neutrino and antineutrino induced interactions without muons in the final state is conclusive evidence for the existence of new phenomena. While the motivation for this work was based on the question of the existence of weak neutral currents, the data are not sufficient to distinguish this from all other possibilities. However, certain hypothetical sources can be ruled out, such as heavy leptons with masses below 3 GeV/c^2, a V-A weak neutral current with coupling constant $G_0^2 > .39\ G^2$ (95% confidence level), or V+A neutral currents.

IX. THE BEAM

The neutrino-antineutrino beam for this research is provided by the Fermilab N-O beamline (Fig. 51). Protons of energies 300 GeV and 400 GeV are extracted from the synchrotron by a coherent extraction technique. The resulting beam spill lasts from 20 to 300 μs. The protons are then guided by the switchyard magnets into the neutrino target hall. There the protons strike an aluminum target located 1400 m from the experimental apparatus. Particles emerging from the target (primarily π and K mesons accompanied by surviving protons) are then focused by a magnetic horn. After being focused the particles enter an evacuated cylindrical decay pipe 340 m long by 1 m in diameter. A fraction of the mesons will decay via

$$\binom{\pi}{K} \rightarrow \mu + \nu_\mu$$

thereby producing the $\nu_\mu(\bar{\nu}_\mu)$ beam. At the end of the decay pipe is a beam stop which absorbs all hadrons which reach it. Following the beam stop is a 910 m earth shield which absorbs the muons produced in the mesonic decays. The shield is interrupted in several places for beam enclosures and experimental areas. Compensating these gaps are sections of steel which harden the shield. The beam emerging from the shield consists primarily of the neutrinos and antineutrinos produced in the decay pipe. However, some fraction of the neutrinos and antineutrinos interract in the shield producing a muon and hadron contamination. The hadrons are absorbed by a 2 m thick heavy concrete shield immediately upstream of the experi-

mental apparatus. The muons produce a distinct signature by traversing the entire apparatus and are easily vetoed by the electronics.

X. IONIZATION CALORIMETER

The calorimeter is composed of four separate tanks each containing 1.9×10^4 liters (16 metric tons) of liquid scintillator[36]. Each tank is subdivided into four optically independent modules with dimensions .46 m x 3.5 m x 2.9 m. The optical separation is provided by sheets of aluminum suspended from the top and bottom of the tanks. The scintillator is viewed by twelve phototubes[37], six on each of two opposing sides. Energy deposited in the liquid by charged particles is converted to light which passes from the liquid, through a plexiglass window, to the phototube. The index of refraction of the window is matched to that of the phototube glass by an optical coupling oil[38]. A cone of flat front surfaced mirrors is used to guide the light to the window. Light collection is further improved by coating all inner surfaces of the calorimeter with a .3 mm layer of Teflon[39]. The Teflon produces total internal reflection into the liquid.

Signals from the twelve tubes viewing each module are passively added by a back terminated daisy chain (Fig. 52). Both anode and dynode signals are carried by a single shielded twisted pair cable. The signals for each module are amplified and the dynode signal is inverted and then added to the anode signal. This doubles the pulse height and rejects common mode noise. After a delay of 300 nanoseconds (so as to be in time with triggering logic) the signal is digitized. Simultaneously the signals from

all 16 modules are added together forming a single pulse for the entire calorimeter. This pulse is fed into a threshold discriminator and is then used as an event trigger.

The response of the calorimeter to minimum ionizing particles has been measured using cosmic ray muons with incident angles less than 18° (300 mr). A typical response curve for a single module is shown in Fig. 53. The uniformity of the response over the surface of the module was measured (Fig. 54) by selecting cosmic ray muons traversing the liquid at various points along the axis of one of the tubes. The response of a single tube is seen to be greatly enhanced with respect to a $1/R^2$ variation by the reflective properties of the Teflon. The response of twelve tubes is seen to be uniform to ±15%.

The calibration of the calorimeter was performed in various beams at Fermilab. High energy muons produced in the earth shield by the neutrino-antineutrino beam were used to calibrate the calorimeter at low energies. The mean energy of these muons is measured to be 20 GeV and 95% are incident at angles less than 7.5^{o} (130 mr). These muons produce a mean energy deposition of 107 MeV per module or 1.7 GeV for the entire calorimeter. For higher energy calibration, π beams of 15 GeV to 146 GeV were targeted onto the calorimeter by the Fermilab N-5 beam line in conjunction with the 15 Foot Bubble Chamber magnet. The calorimeter response can be parameterized by the form $E_{vis}=E_{\pi}/[1 + .255\ \mathrm{Exp}(-E_{\pi}/E_{o})]$ with E_{o}=111.6 GeV (Fig. 55). The widths of the pulse height distributions

produced by the pion beams are a direct measure of the intrinsic resolution of the calorimeter. These distributions, shown in Fig. 56 indicate an intrinsic resolution of ±15% for energies less than 150 GeV.

The pions in the calibration beam are required to traverse the first module of the calorimeter without interacting so as to eliminate interactions which occurred upstream of the apparatus. Most of the pions then interact within the next few modules due to the .5 nuclear collision lengths per module. The remaining ten to fourteen modules provide a minimum of six collision lengths which prove sufficient to fully attenuate the hadronic cascades resulting from the pion interactions. Experimentally this is observed by the low or zero pulse height in the sixteenth calorimeter module. In this way one can be certain that the corrected energy measurement is equal to the incident hadron energy.

When measuring the energy of hadronic cascades resulting from neutrino collisions, the interaction vertices are not constrained to lie in the first few calorimeter modules. In fact they are uniformly distributed among the sixteen modules. For those interactions occurring in the more downstream modules a further correction must be made to the hadronic energy measurement to account for energy escaping from the downstream end of the calorimeter.

To make this final correction one needs to know what fraction of the ionization energy is actually observed. This is

measured experimentally by studying neutrino collisions which occur in the second module of the calorimeter. All such collisions are observed experimentally to be at least 95% contained within the fourteen remaining modules. The resulting transition curves are then used to calculate directly the shower containment as a function of vertex location and hadronic energy.

XI. WIDE GAP SPARK CHAMBERS (WGSC)

The wide gap spark chambers consist of three conducting planes separated by plexiglass spacers. Each plane has dimensions 3.05 m x 3.05 m x 1.27 cm and is made of an aluminum honeycomb with a solid outer aluminum frame and a 1 mm thick aluminum skin. The plexiglass spacers are 5 cm thick and are polished so that the chambers can be used with an optical recording system. When epoxied between the conducting planes the spacers form a chamber which is filled with a gas mixture of 80% neon + 20% helium. The mixture is kept pure by the continual flow into the chambers of fresh gas at the rate of 2 cm^3/sec. The slight overpressure needed to maintain this flow prevents air from entering the chambers.

When an event trigger is produced, a signal is sent to a spark gap driver amplifier[40]. The amplifier fires a thyratron[41] which discharges a capacitor bank. This discharge produces a 9.5 KV pulse which is used to trigger one Marks generator for each WGSC. The Marks generator (Fig. 57) consists of three banks of capacitors which are charged in parallel to -11 KV. The 9.5 KV pulse fires three sets of spark gaps within the generator. This puts the three banks in series resulting in a +33 KV pulse to the center plane of the WGSC. The gaps are prevented from firing spontaneously by maintaining 1.4 kg/cm^2 pressure of nitrogen within the Marks generator vessel.

If the chamber gas has been sufficiently ionized by the

traversal of a charged particle, the +33 KV pulse results in sparks (referred to as tracks) between the center high voltage plane and the two outer ground planes of the WGSC. Small impurities of highly electronegative gases such as oxygen will absorb ionization electrons so fast that it is impossible to produce tracks. However, if the gas is pure the efficiency for producing tracks in response to cosmic ray muons incident at angles less than 350 mr is measured to be greater than 99%. Recombination of the ionized gas is sufficiently slow that the efficiency remains above 90% even if the firing occurs more than 10 μs late. This proved to be a problem so a static electric field of -200 Volts/cm is used to clear the ions from the WGSC. Tests show that the time period during which the chambers "remember" a track can be reduced in this manner to 3.5 μs (Fig. 58). Further reduction is difficult due to the velocity saturation of the electrons[42].

XII. IRON CORE MAGNET

The iron core magnet is constructed in four modules. Each module consists of six cylinders of iron 20 cm thick with inner radius 15 cm and outer radius 183 cm. Each cylinder is assembled from four blocks (Fig. 59) with 2.4 mm stainless steel spacers maintaining gaps in between. The spacers maintain uniform gaps between the blocks for uniformity of magnetic field and for insertion of field measuring devices.

Water cooled copper conductors carry the current to produce the field. Each magnet section has 12 coils (7 turns per coil) wrapped around it in a toroid. The geometry is sufficiently complex that an analytical solution for the magnetic field is impossible. However, due to the magnetization effects of the iron, the field can be approximated by that of a straight wire. The static field equation

$$\vec{\nabla} \times \vec{H} = \frac{4\pi}{c} \vec{J}$$

has the approximate solution

$$\vec{H} = \frac{2I}{cR} \vec{\theta}$$

where I = 84 turns x current per turn

$c = 3 \times 10^{10}$ cm/sec

R = distance from wire

$\vec{\theta}$ = unit vector in azimuthal direction

A more accurate solution requires use of the magnetization (μ) curves (Fig. 60) for the iron and the application of boundary

conditions at the gaps. At the vertical gaps the H field is approximately normal to the boundary so the requirement is

$$\vec{B}_{iron} = \vec{B}_{gap} \equiv B\,\vec{\theta}$$

To solve for B one need only integrate the field equation within a circle [43] of radius R and apply the boundary conditions.

$$\frac{4\pi I}{c} = \int (\vec{\nabla} \times \vec{H}) \cdot dA = \oint \vec{H} \cdot d\vec{l} = 2\pi R H_{iron} + 2gH_{gap}$$

Using $B_{gap} = H_{gap}$

$B_{iron} = \mu H_{iron}$

g = gap width = 2.4 mm

and solving for B yields

$$B = \frac{2I\mu}{cR}\left(\frac{1}{1 + \frac{g\mu}{\pi R}}\right)$$

At the horizontal gaps the field is incident at varying angles. In addition each field line crosses four gaps as opposed to two for the vertical. The boundary conditions are

$$B_{gap}^{norm} = B_{iron}^{norm} = B\sqrt{1 - \left(\frac{X}{R}\right)^2}$$

$$B_{gap}^{tan} = \frac{1}{\mu} B_{iron}^{tan}$$

X = 61 cm (see Fig. 9)

Since μ is larger (μ>100) the tangential component in the gap can be ignored. Again integrating the field equation and applying boundary conditions

$$B = \mu \frac{2I}{cR} \left\{ \frac{1}{1 + \frac{2g\mu}{\pi R} \sqrt{1 - \left(\frac{X}{R}\right)^2}} \right\} .$$

The field magnitude as a function of R for this circular approximation is shown in Fig. 61.

The magnetic field can also be found by solving Maxwell's equations numerically. This avoids any assumptions as to the shape of the field lines. The program TRIM[44] was used on the Argonne National Laboratory IBM 360/65 computer and the results are shown in Fig. 61 to be in substantial agreement with the circular approximation[45].

As previously mentioned, the stainless steel spacers maintain gaps for the purpose of inserting field measuring instruments. For this purpose Hall generators[46] are mounted on fibre boards and inserted into the gaps. The plane of the generators is mounted parallel to the plane of the gap. A magnetic field produces a voltage at the generator terminals which is related to the field strength normal to the plane of the generator. Each generator was calibrated using a nuclear magnetic resonance technique as a reference. In this way the fields normal to the gaps are measured. The measured as well as the calculated fields are shown in Fig. 62.

XIII. TRIGGER COUNTERS

The experimental apparatus employs two types of trigger counters. A, B, and D are identical counters using liquid scintillator and C is an array of plastic scintillation counters.

Each liquid counter is composed of three separate tanks (modules) with dimensions 3.6 m x 1.2 m x .10 m. The full counter is assembled by stacking the three tanks on top of each other (Fig. 63). Each tank is filled with 450 liters of liquid scintillator[36]. The scintillator is viewed by eight phototubes[47], four on each of two opposing sides. High light collection efficiency is maintained through the use of Teflon linings, mirror cones, and optical coupling oil (see calorimeter discussion).

Signals (Fig. 64) from the four phototubes viewing one side of each counter module are linearly added, amplified, and then fed into a threshold discriminator. This results in six pulses for each counter[48]. Counters B and D are used as muon identifiers. To protect against accidental pulses and to provide a precisely timed signal, the right and left pulses for each module of B and D are fed into mean timing circuits. The timing of the output pulse from the mean timing circuit is independent of the position of the triggering particle in the module to ±1.5 ns. This is to be contrasted with the intrinsic ±4.5 ns which would result from the physical dimensions[49] alone if standard coincidence logic were used. The resulting pulses are used for triggering and particle tagging. Counter A is used as a veto counter to inhibit triggers produced by

charged particles entering the front of the apparatus. Because of its location, counter A is subjected to a high flux of particles during the accelerator beam spill. This would tend to overload a mean timer so standard coincidence logic is used. Counter C is an array of sixteen plastic scintillation counters each with dimensions .61 m x 1.2 m x 1.2 cm (Fig. 65). Light is collected at one end using a plexiglass light pipe. A single phototube[47] views each counter. The sixteen signals are linearly added (Fig. 66) and fed into a threshold discriminator. The discriminator output is then available for triggering or particle tagging.

XIV. NOISE

The inevitable result of discharging 33 KV in the WGSC is the production of large amounts of electrical noise. The discharge results in sparks between any two nearby conducting surfaces. Signal cables located 10 cm from the WGSC have been observed to arc to nearby ground planes. The shields on the Marks generator high voltage cables arc through their insulation when placed near each other. These sparks produce additional noise signals. The result of this noise has been disruption of virtually every phase of our data taking procedures.

In order to reduce the noise levels several steps are taken. While the WGSC can operate efficiently when filled with pure helium, this requires operation at 48 KV. The use of the much more expensive neon-helium mixture allows the reduction of voltage to 33 KV resulting in a large reduction in noise. All cables connected to the Marks generators are suspended a minimum of 4 cm from any conducting material. The Marks generators are all grounded via the shortest path to the iron magnet. All cables are kept as far from the WGSC as is physically possible. All power supplies associated with the WGSC are kept as close to the WGSC and as far from the other electronics as possible.

From the time that the decision is made by the triggering logic to fire the WGSC, there is approximately 300 ns remaining before the noise signals arrive at the data recording electronics. This allows sufficient time for all trigger counter and ionization

calorimeter information to be stored in the various electronic devices. In addition it provides time to establish a logical inhibit in all devices which might otherwise record the noise signals as data. After extensive study it was shown that most of the commercially available NIM and CAMAC standard electronics we use can be successfully protected from WGSC noise by use of logical inhibits. Special noise immune circuits were built to control the advancing of the camera (Fig. 74) and frame number (Fig. 67).

Digitizing the signals from the ionization calorimeter is the most delicate problem since the signal levels are as small as 100 μv. To deal with this several steps are taken. The tube base for each phototube is grounded to the iron shield surrounding the phototube. This shield is then electrically isolated from the calorimeter tank itself. In this way the shield and tube base form a Faraday cage around the tube and base, and noise signals are not transmitted from the tanks to the electrical ground. The phototube signals are carried by shielded twisted pair cables insuring that virtually all noise signals are common to the anode and dynode lines. Inverting the dynode signal and adding it to the anode then eliminates virtually all common mode noise transmitted through the cables. The remaining noise which enters the analog to digital conversion units is small compared to the amplified phototube signals.

XV. OPTICS

The optics in this experiment are designed so as to view the eight WGSC at three different angles and record the images with two cameras (Fig. 68). Two views consist of a $\pm 7.5^{0}$ stereo system viewing all eight WGSC with one camera. The third consists of the four upstream WGSC viewed at 90^{0} by a second camera.

The 90^{0} camera views the four WGSC 1-4 through an 80 mm lens set at f/5.6. The light from each WGSC is brought to the camera by two bending mirrors as shown in Fig. 69. The mirrors are placed so as to provide approximately equal optical path lengths to each WGSC.

The $\pm 7.5^{0}$ camera views WGSC 1-8 through a 210 mm lens set at f/11 . The mirror system (Fig. 70) is divided into two parts. WGSC 1-3 provide shower identification. The light from each WGSC is reflected by three bending mirrors into the upstream stereo mirrors. The two views created by the stereo mirrors are then bent into the camera with two small mirrors. WGSC 4-8 are used as muon identifiers. Since they typically have only one track they produce a much brighter spark then WGSC 1-3 which typically have many tracks. To reduce the light output a .8 neutral density filter is placed in front of each window of WGSC 4-8. The remaining light is reflected by three bending mirrors to the downstream stereo mirrors which are viewed directly by the camera.

Each WGSC has four fiducial marks for each camera which views

it. The marks are back-lighted "X"s machined into black opaque plexiglass. The fiducial lamps are flashed for four seconds after each event. A visual frame number consisting of six gas discharge tubes is also flashed after each event.

Muon tracks are measured using digitizing measuring tables. Corrections are made taking into account the distortions introduced by the mirrors and the WGSC windows. A correction is also made to account for refraction of the light passing through the windows (Snell's law). Reconstruction resolutions of 2 mm in the plane perpendicular to the optical axis (Y) and 6 mm in the plane parallel to the optical axis (X) have been measured. This is comparable to the 5.6 mm projected rms multiple scattering of a 15 GeV muon traversing one section of the magnetic spectrometer. A calibration of the entire system was made using approximately monoenergetic muons produced by pion decays in the N-5 beam line. Since pions were not removed from the beam, the distribution is somewhat skewed towards lower momenta. The measured momentum distributions are shown in Fig. 71. The resolution is seen to vary from 10% to 50% over the range 20 GeV/c to 125 GeV/c. The resolution is broadened by the fact that all the calibration muons were deflected in the horizontal plane where measurement errors are most severe.

XVI. ELECTRONIC LOGIC AND DATA RECORDING

An event trigger can be produced in either of two ways. The signals from the trigger counters can be required to be in coincidence. For example a BCD trigger (counters B,C, and D in coincidence) is used to identify muons which leave the calorimeter and traverse the entire magnetic spectrometer. A second event trigger (E) is produced by a minimum energy deposition in the calorimeter. For the electronics to accept either of these triggers three additional conditions must be satisfied which I label experiment on gate, WGSC ready, and computer ready. These are described below.

The trigger rate due to cosmic rays satisfying the $\overline{A}E$ trigger (A counter in anti-coincidence with E) is measured to be 50/sec. To reduce the trigger rate an experiment on gate is established. The 1 MHz clock train which is used to time the cycles of the Fermilab synchrotron is provided to each experiment. Using these signals we can provide an electronics gate which is timed to the beam extraction to within 14 μs. The actual spill lasts about 300 μs. For safety we begin our beam on gate 400 μs early and end it 300 μs late for a total gate of 1 ms. In addition, to provide a normalization for cosmic ray triggers within the beam on gate, a beam off gate of 1 ms is established immediately following the beam on gate. The experiment on gate is the sum of the beam off and beam on gates.

Each time the WGSC are fired the Marks generator capacitors

must be recharged. For this purpose, immediately following an event trigger the electronics are disabled for approximately 4 seconds after which the WGSC ready condition is re-established. During normal operation this has little effect. The cameras could not advance fast enough to record a second event during the 300 μs spill and the accelerator cycle time is at minimum six seconds so the generators are always ready by the next pulse.

While the computer is waiting to receive an event trigger interrupt the computer ready condition is established. As soon as an event trigger interrupt is received, the ready condition is removed and is not reestablished until the entire data recording procedure is complete.

Once the electronics accepts an event trigger the data recording cycle begins. Gates are sent to various electronic devices (Fig. 72). After a delay to permit completion of data storage an interrupt is sent to the computer[50] which reads the electronics output registers via a standard CAMAC dataway, branch highway, and electronic interface, and writes the data on magnetic tape. The event trigger is also used to discharge the WGSC and flash fiducial lamps and visual frame number for recording on the film. After all data are recorded the registers are cleared, the camera is advanced, the computer ready condition is established, and the apparatus is ready to accept another event.

FOOTNOTES

1) G. Bernardini, Rendiconti Della Scuola Internazionale Di Fisica "Enrico Fermi", Course XXXII, 1 (1964).

2) E. Fermi, Nuovo Cimento 11, 1 (1934).

3) I will adopt the convention that in all Lagrangians the Hermitian conjugate term is understood, i.e., $L=J_H^\dagger J_L$ implies $L=J_H^\dagger J_L+J_L^\dagger J_H$.

4) P. Bloch et al., XVII International Conference on High Energy Physics, London, 1974.

5) A. R. Clark et al., Physical Review Letters 26, 1667 (1971). At the International Conference of Elementary Particles, Aix-En-Provence, 1973, B. Stech reported that the $K_L^0 \to \mu^+\mu^-$ branching ratio had been changed by the LRL group to $\leq 3.5\times10^{-9}$.

6) U. Camerini et al., Nuovo Cimento 37, 1795 (1965).

7) W. C. Carithers et al., Physical Review Letters 30, 1336 (1973). Six events observed.

8) Reported by C. Rubbia, 16th International Conference on High Energy Physics, Chicago-Batavia, #687, 1972.

9) J. H. Klems et al., Physical Review D4, 66 (1971).

10) H.S. Gurr et al., Physical Review Letters 28, 1406 (1972) H.S. Gurr et al., Physical Review Letters 33, 179 (1974).

11) D.C. Cundy et al., Physics Letters 31B, 478 (1970).

12) W. Lee, Physics Letters 40B, 423 (1972). This is an analysis using the 1963-1965 Columbia-BNL neutrino experiment data.

13) Reported by D. H. Perkins, 16th International Conference on High Energy Physics, Chicago-Batavia, 1972, from a paper by Cho et al.

14) F. J. Hassert et al., Physics Letters 46B, 138 (1973).

15) The mass of the muon will be ignored everywhere. The units $\hbar=c=1$ are used.

16) J. D. Bjorken, E. A. Paschos, Physical Review D1, 3152 (1970).

17) R. P. Feynman, M. Gell-Mann, Physical Review 109, 193 (1958).

18) J. D. Bjorken, Physical Review 179, 1547 (1969).

19) T. Eichten et al., Physics Letters 46B, 274, 281 (1973).

20) A. Benvenuti et al., Physical Review Letters 30, 1084 (1973).
A. Benvenuti et al., Physical Review Letters 32, 125 (1974).

21) A. Benvenuti et al., Physical Review Letters 32, 800 (1974).
B. Aubert et al., Physical Review Letters 32, 1454 (1974).
B. Aubert et al., Physical Review Letters 32, 1457 (1974).

22) The technique for determining α is described in Section VI.

23) P. Limon et al., Fermilab report No. NAL-Pub-73/66-EXP, (1973).

24) To correct for a 3% geometric inefficiency due to spacers in counter B, events without a count in B but with a count in counter C or a track in WGSC5 were included in the C sample of MU1.

25) Events in which a second muon was positively identified are not counted here.

26) G. Miller et al., Physical Review D5, 528 (1972). We used an empirical fit by V. Barger, "Two Component Dual Parton-Regge Model of Deep Inelastic Electron and Neutrino Structure Functions", Preprint (1973).

27) R. W. Brown, J. Smith, Physical Review D3, 207 (1971).

28) B. G. Barish et al., Physical Review Letters 31, 180 (1973).
G. Bernardini et al., Il Nuovo Cimento 38, 608 (1965).
R. Burns et al., Physical Review Letters 15, 42 (1965).

29) J. D. Bjorken, C. H. Llewllyn Smith, Physical Review D7, 887 (1973).
C. H. Llewllyn Smith, Ref. Th. 1621-CERN, 1973.

30) B. C. Barish et al., Physical Review Letters 31, 410 (1973) and 32, 1387 (1974).

31) These effects have been calculated for specific models.
C. H. Albright et al., Ref. Th. 1855-CERN, 1974.

32) B. Aubert et al., Physical Review Letters 33, 984 (1974).

33) S. Weinberg, Physical Review Letters 27, 1688 (1971).
A. Salam, Elementary Particle Theory, edited by N. Svartholm, Almquist and Forlug, Stockholm, 1968. The parameter w is usually referred to as $\sin^2\theta_W$.

34) L. M. Sehgal, Nuclear Physics B65, 141 (1973).

35) E. A. Paschos, L. Wolfenstein, Physical Review D7, 91 (1973).

36) 70% mineral oil; 30% 1,2,4 trimethyl benzene; density .85 gram/cm^3. Nuclear Enterprises type NE235A. Index of refraction 1.47.

37) RCA #8055 phototube with 12.5cm diameter photocathode.

38) Dow Corning Silicon Oil. Index of refraction 1.495.

39) Index of refraction 1.33.

40) Scientific Accessories Corporation model 002A Spark Gap Driver Amplifier.

41) E. G. G. model H Y-62 Thyratron.

42) Keller, Schluter, and White, Nuclear Instruments and Methods, 41 (1966).

43) Field lines for this calculation are assumed to be circles.

44) Lari, and Wilhelm, Computer Program TRIM for Magnet Design, Argonne National Laboratory, May 20, 1970;
R. Lari, personal communication.

45) Magnetization curves for the TRIM calculation were somewhat different from those used for the circular approximation. This explains the slight differences between the results of the two calculations.

46) Siemens Hallgenerator type SV210.

47) RCA #8575 phototube with 5 cm diameter photocathode.

48) Signals are labeled as to which counter the signal came from (A,B,D), which module (Top, Middle, Bottom) and which side (Right, Left).

49) The maximum light path is 1.8m. The index of refraction of the liquid is 1.47. The resulting timing error is 1.8m/[(.3 m/ns)/1.47]= 9 ns. This implies a timing

resolution of ±4.5 ns.

50) Digital Equipment Corporation PDP-11 model 20 computer.

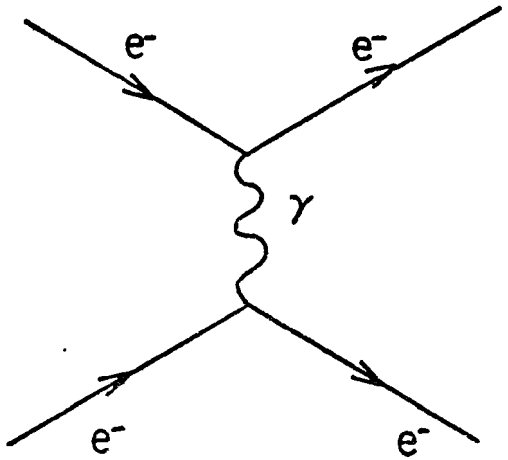

ELECTROMAGNETIC

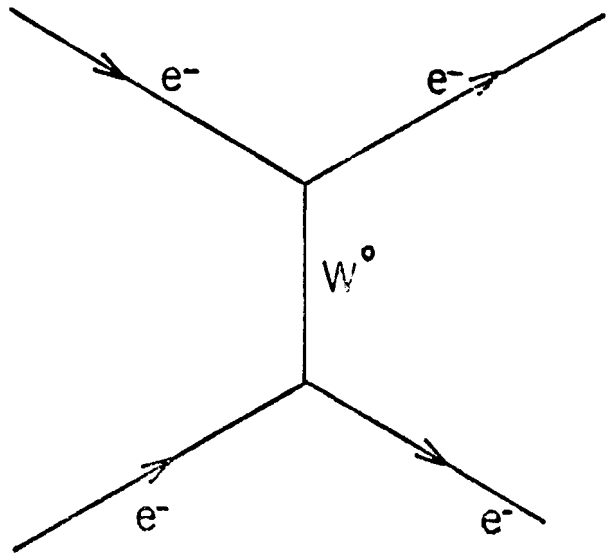

NEUTRAL WEAK

Fig. 1

$K^{\pm}\to\pi^{\pm}e^{+}e^{-}$	$K^{0}_{S,L}\to\pi^{0}e^{+}e^{-}$
$K^{\pm}\to\pi^{\pm}\mu^{+}\mu^{-}$	$K^{0}_{S,L}\to\pi^{0}\mu^{+}\mu^{-}$
$K^{\pm}\to\pi^{\pm}\nu\bar{\nu}$	$K^{0}_{S,L}\to\pi^{0}\nu\bar{\nu}$
$K^{0}_{S,L}\to e^{+}e^{-}$	$K^{0}_{S,L}\to\mu^{+}\mu^{-}$

Possible K-meson decays involving a neutral leptonic current.

Fig. 2

DECAY	EFFECTIVE SAMPLE	BRANCHING RATIO OR UPPER BOUND	b/c	GROUP
$K^+ \to \pi^+ e^+ e^-$	----	$= 2.3 \pm .08 \times 10^{-7}$	c	Saclay - Geneva[4]
$K_L^o \to e^+ e^-$	$.57 \times 10^9$	$\leq 1.57 \times 10^{-9}$	c	LRL[5]
$K^+ \to \pi^+ \mu^+ \mu^-$	$.77 \times 10^6$	$\leq 3 \times 10^{-6}$	b	Wisconsin-LRL[6]
$K_L^o \to \mu^+ \mu^-$	$.57 \times 10^9$	$\leq 1.82 \times 10^{-9}$	c	LRL[5]
	$.63 \times 10^9$	$= 11^{+10}_{-5} \times 10^{-9}$	c	Columbia-CERN-NYU[7]
$K_S^o \to \mu^+ \mu^-$	----	$\leq 4 \times 10^{-7}$	c	CERN-Heidelberg[8]
$K^+ \to \pi^+ \nu \bar{\nu}$	1.2×10^9	$\leq 1.4 \times 10^{-6}$	c	Chicago-LRL[9]

Results of searches for neutral currents in K-meson decays. b indicates bubble chamber. c indicates counter-spark chamber.

Fig. 3

Neutrino spectra

Laboratory	Energy
BNL	peak = 1 to 2 GeV
CERN	peak = 2 GeV, maximum = 10 GeV
ANL	peak = .5 GeV, maximum = 3 GeV
FNAL	peak = 40 GeV, maximum = 200 GeV
Savannah River	$3.6 \leq E_\nu \leq 5$ MeV

Fig. 4

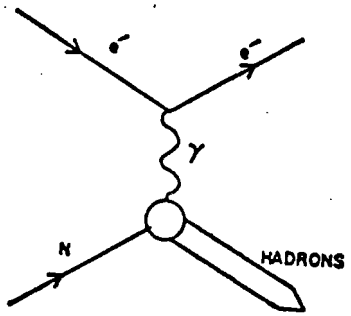

INCLUSIVE ELECTROPRODUCTION

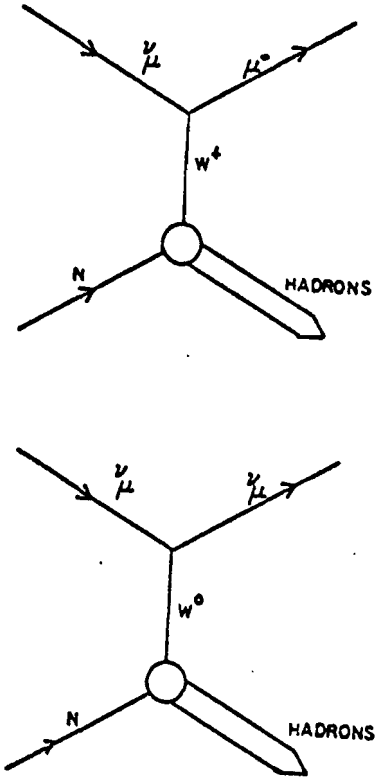

INCLUSIVE NEUTRINO PRODUCTION

Fig. 5

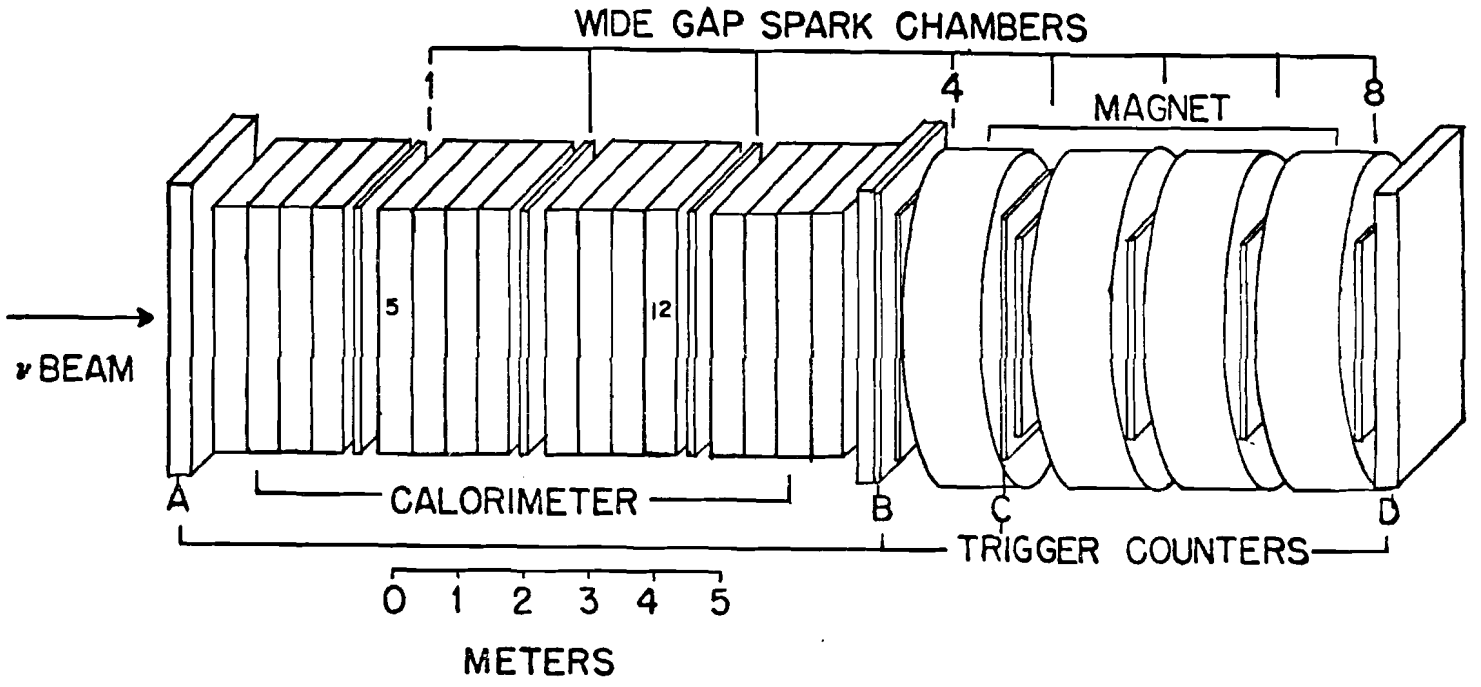
WIDE GAP SPARK CHAMBERS
1
4
8
MAGNET
5
12
ν BEAM
A
CALORIMETER
B
C
D
TRIGGER COUNTERS
0 1 2 3 4 5
METERS

Fig. 6

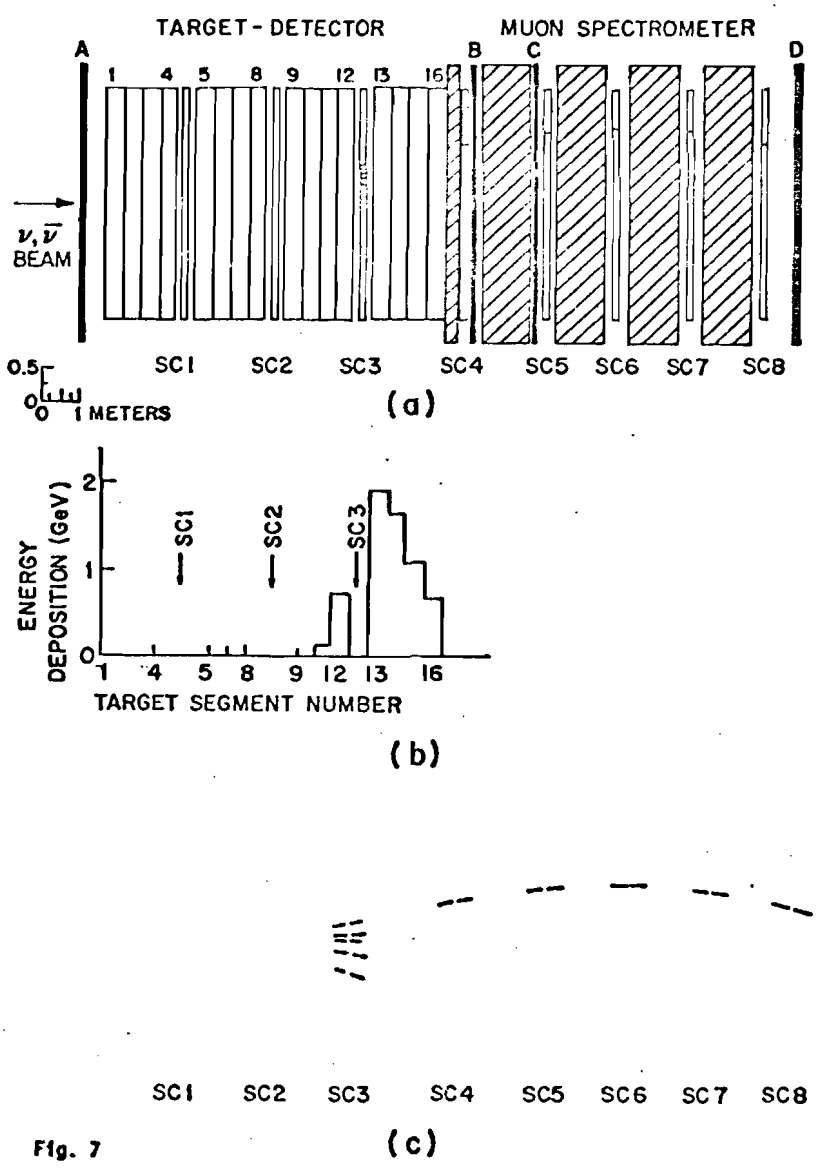
TARGET - DETECTOR
MUON SPECTROMETER
A
B
C
D
1 4 5 8 9 12 13 16
ν, ν̄
BEAM
SC1 SC2 SC3 SC4 SC5 SC6 SC7 SC8
0.5
0 1 METERS
(a)
ENERGY DEPOSITION (GeV)
2
1
0
SC1
SC2
SC3
1 4 5 8 9 12 13 16
TARGET SEGMENT NUMBER
(b)
SC1 SC2 SC3 SC4 SC5 SC6 SC7 SC8
(c)

Fig. 7

Fig. 8 225469

Fig. 9

225450

VERTEX MEASUREMENT ERROR

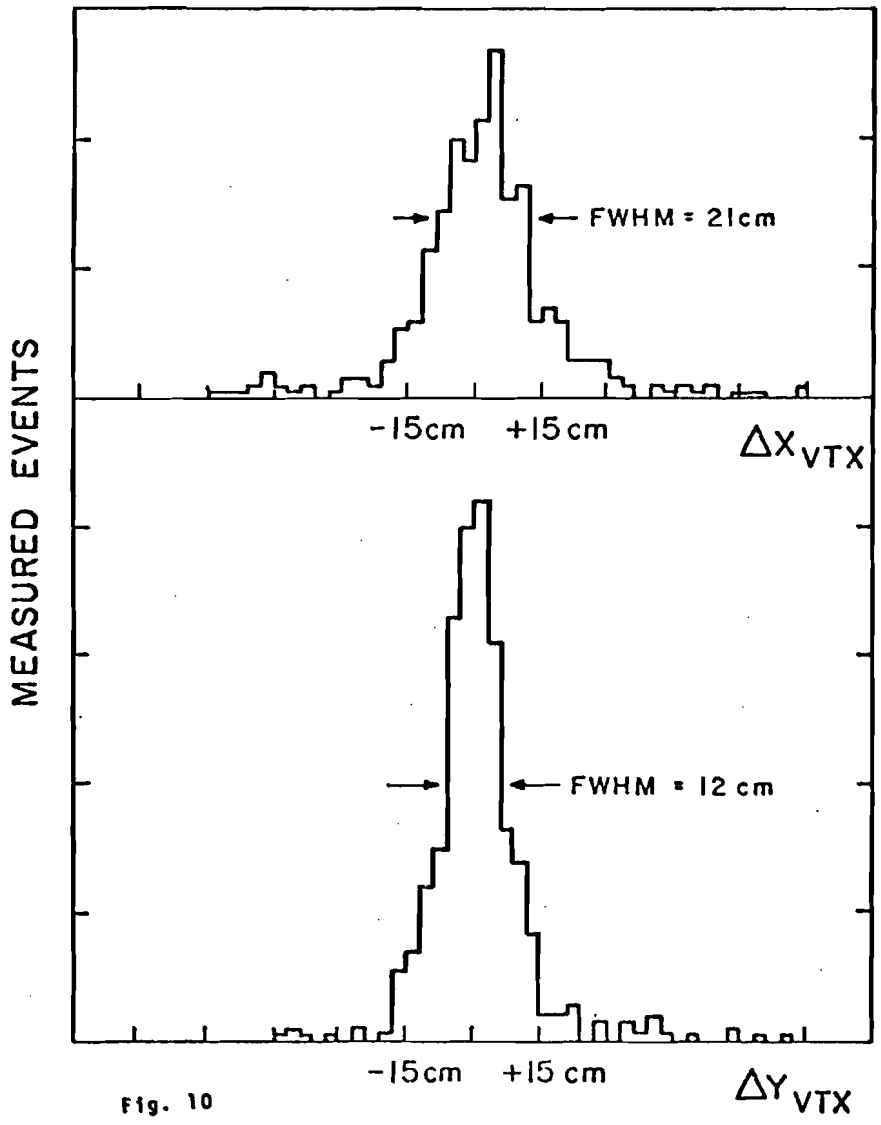

Fig. 10

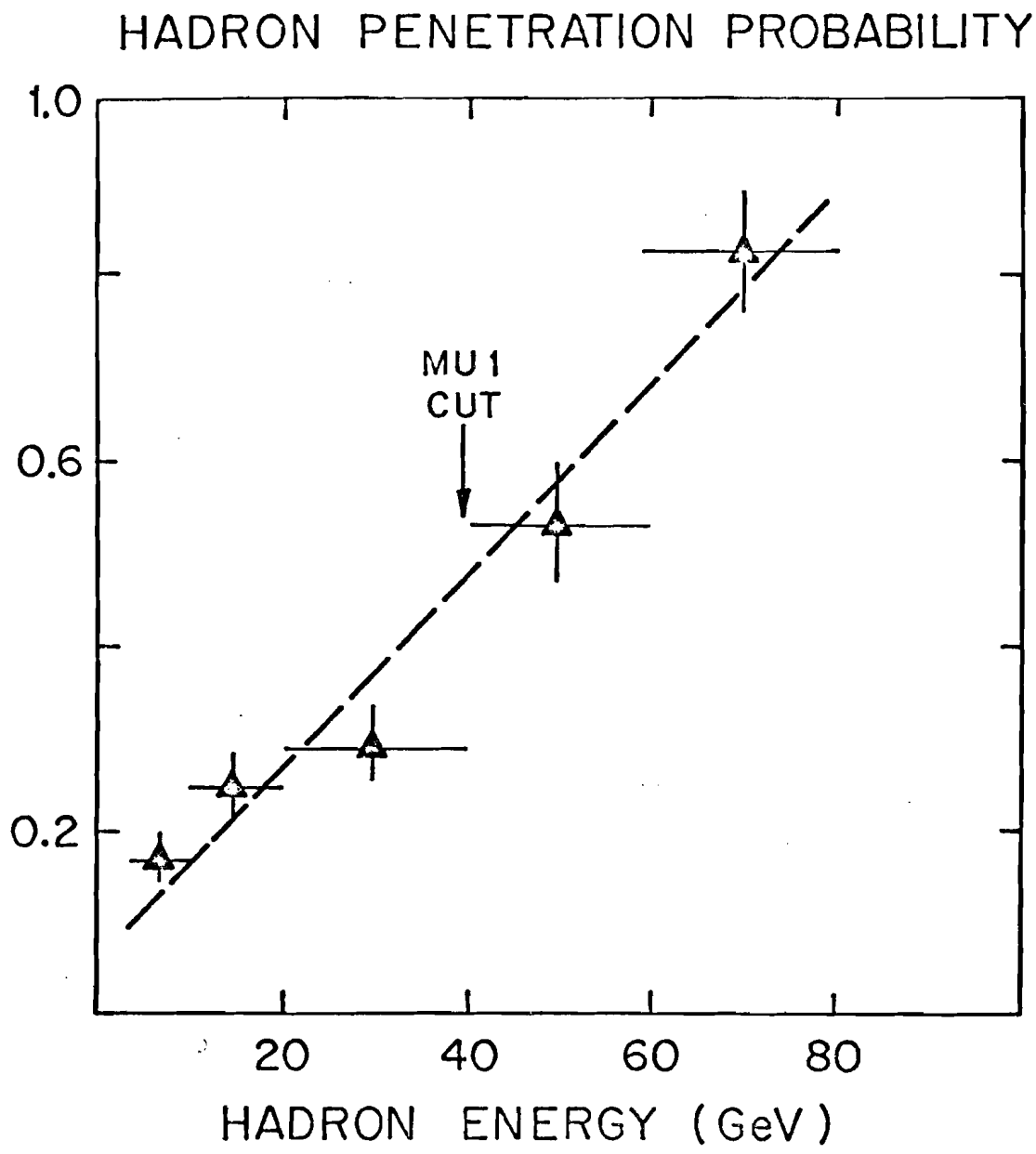
HADRON PENETRATION PROBABILITY
1.0
0.6
0.2
MU 1
CUT
20
40
60
80
HADRON ENERGY (GeV)

Fig. 11

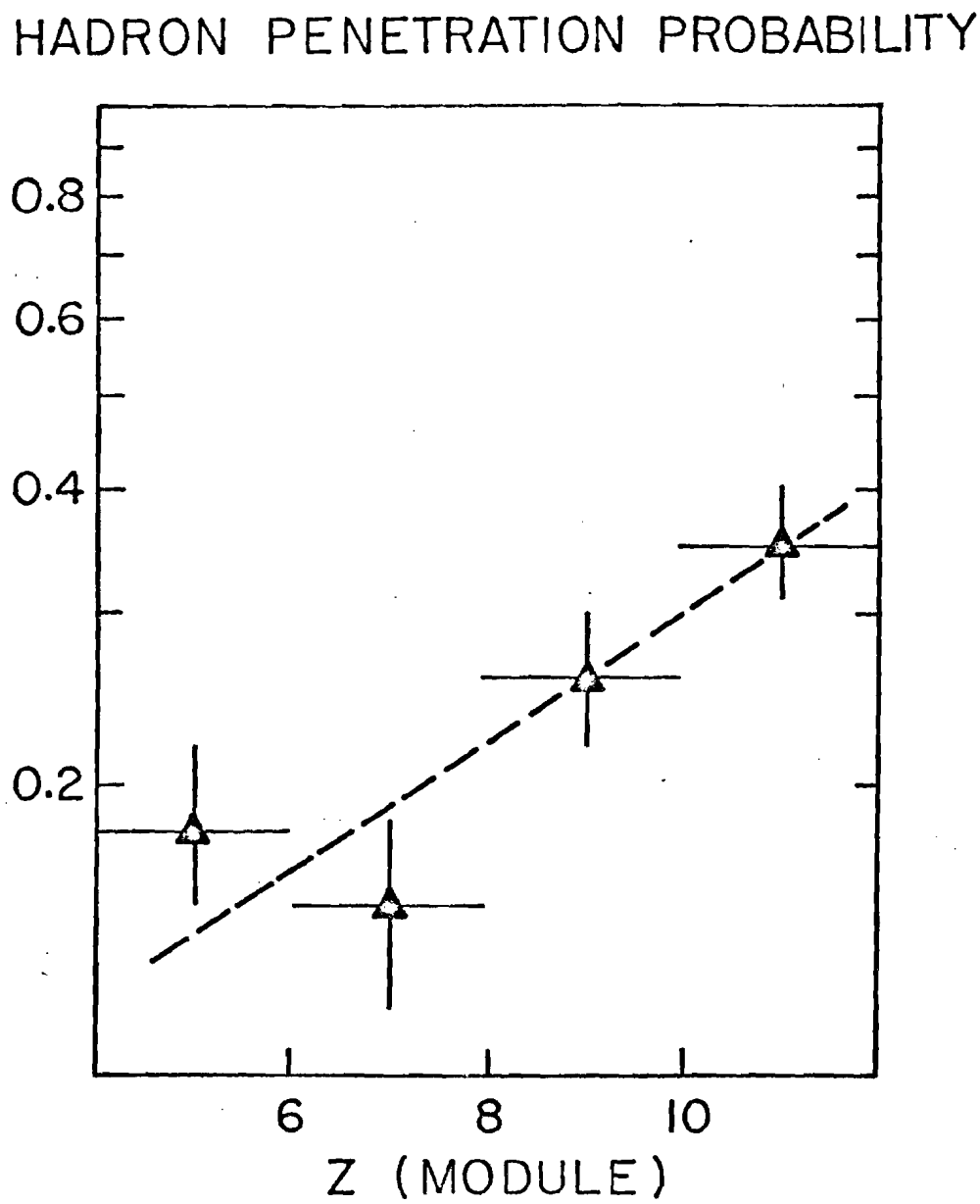

Fig. 12

JULY 3, 1975

2.T.	300	400
	.836	
	348	407
	MU2	MU2
	.55 (.40)	.43
	0	0
	.55	.43
	.823 (μb)	.867 (μb)
	.28 ± .05	.24 ± .04
	.26 ± .03 *	

* Average of R_{corr} for MU1, MU2, MU3 and 300 and 400 GeV

Proton Energy (E_p)	400 GeV			300 GeV		
α	.94±.01			.62±.03		
Events	891	1123		563	654	
Detector	MU1 (E_H<40)	MU2	MU3	MU1 (E_H<40)	MU2	MU3
Raw Data	229/662	485/638	---	118/445	227/427	---
N/C = R	.35±.03	.76±.05	---	.27±.03	.53±.04	---
Average Hadron Penetration Probability	.24	0.0	---	.24	0.0	---
R corrected for hadrons	.51±.04	.76±.05	481/642 .75±.05	.38±.05	.53±.04	238/411 .58±.09
Average Muon Detection Efficiency	.856	.757	.774	.885	.796	.810
R	.29±.04	.33±.03	.35±.04	.22±.04	.22±.04	.28±.07
Average R	.32±.04			.22±.04		

BONY? (+SC(6) [illegible] ONLY

Data and Corrections

Fig. 13

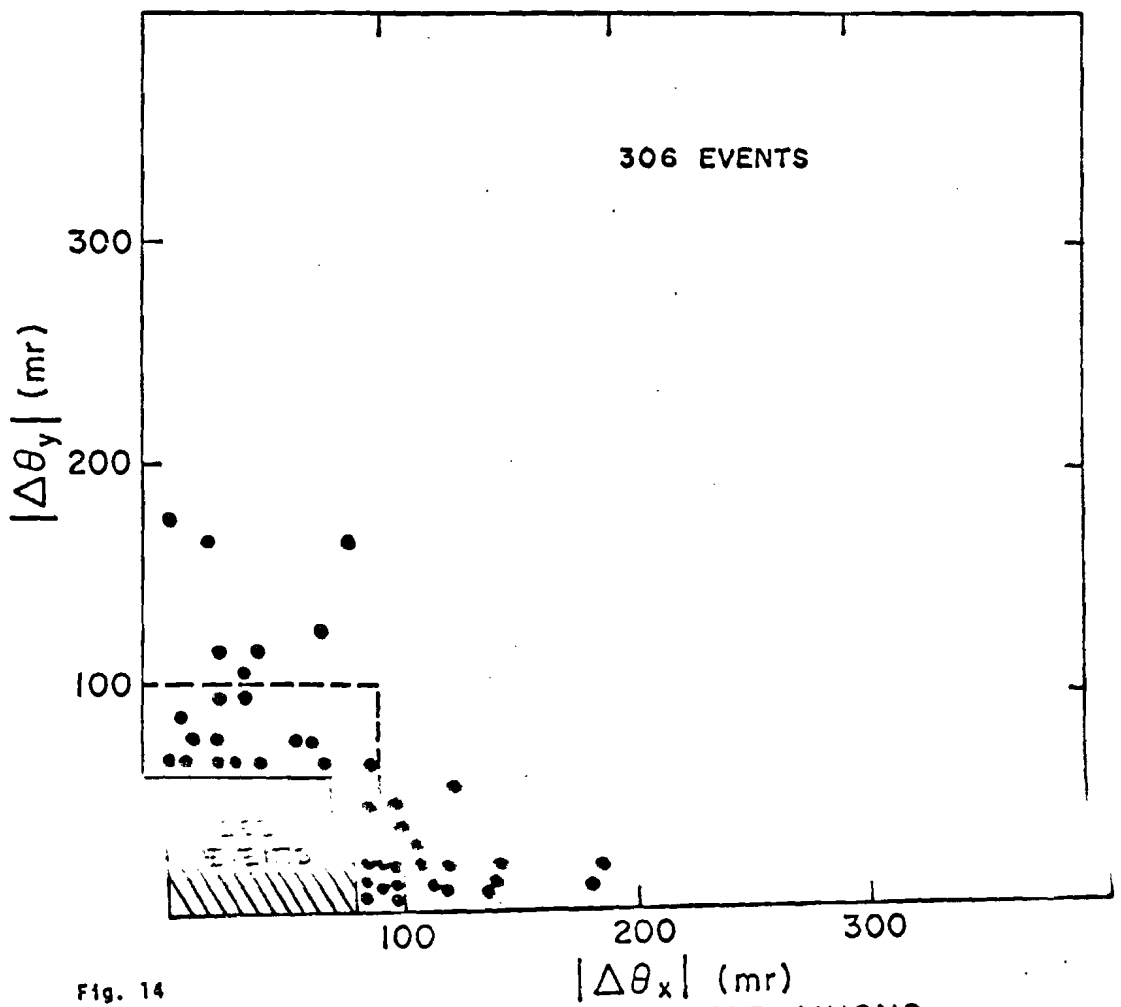

Fig. 14

ANGULAR ERRORS FOR MUONS

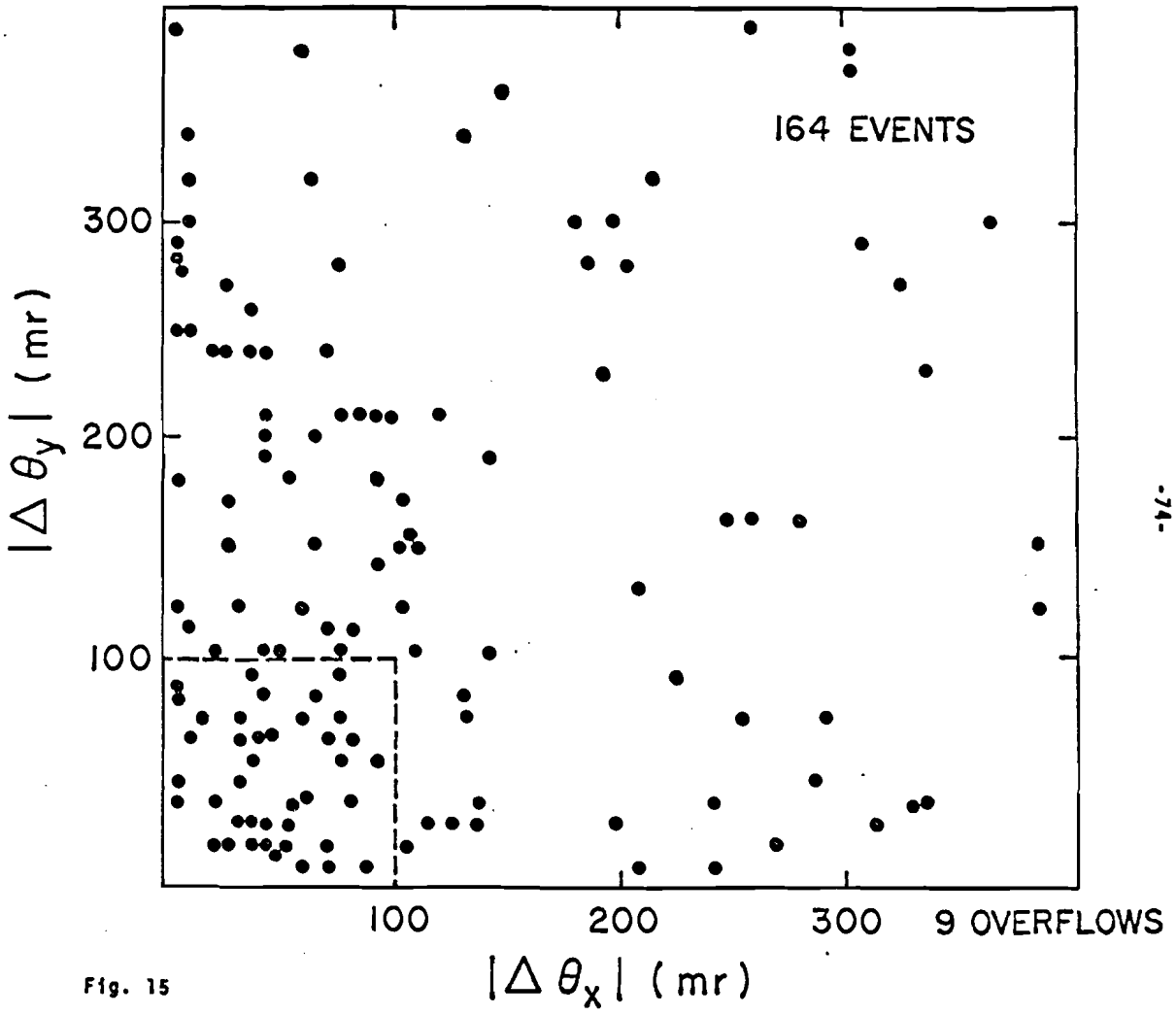
164 EVENTS
300
200
100
$|\Delta\theta_y|$ (mr)
100
200
300
9 OVERFLOWS
$|\Delta\theta_x|$ (mr)

Fig. 15

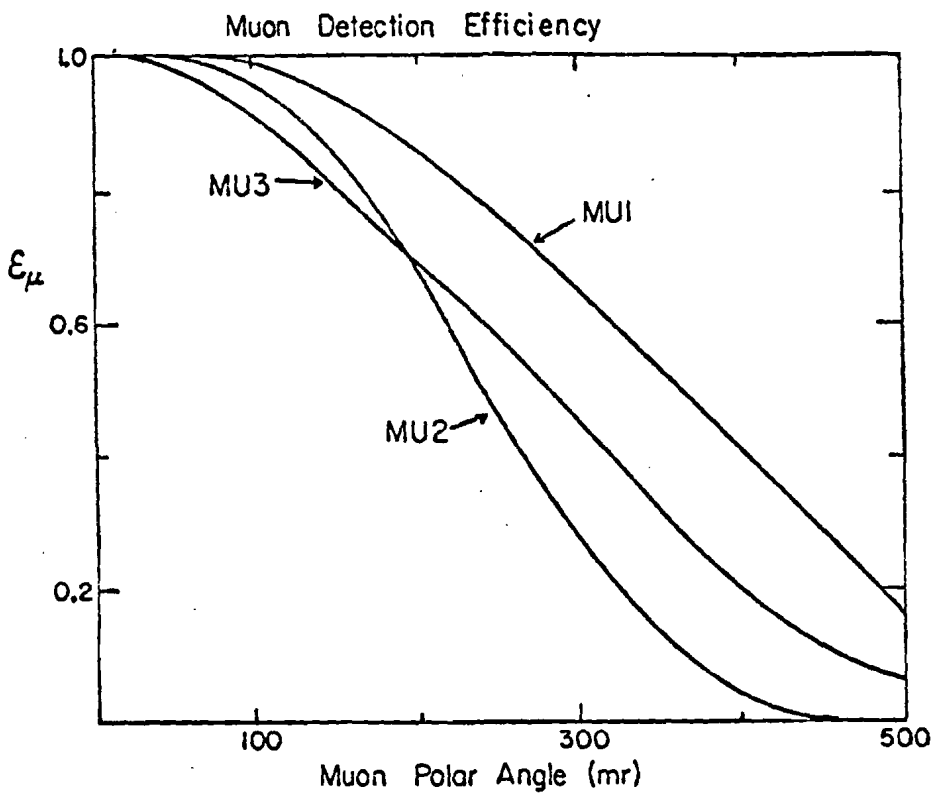
Muon Detection Efficiency
1.0
0.6
0.2
ε_μ
MU3
MU1
MU2
100
300
500
Muon Polar Angle (mr)

Fig. 16

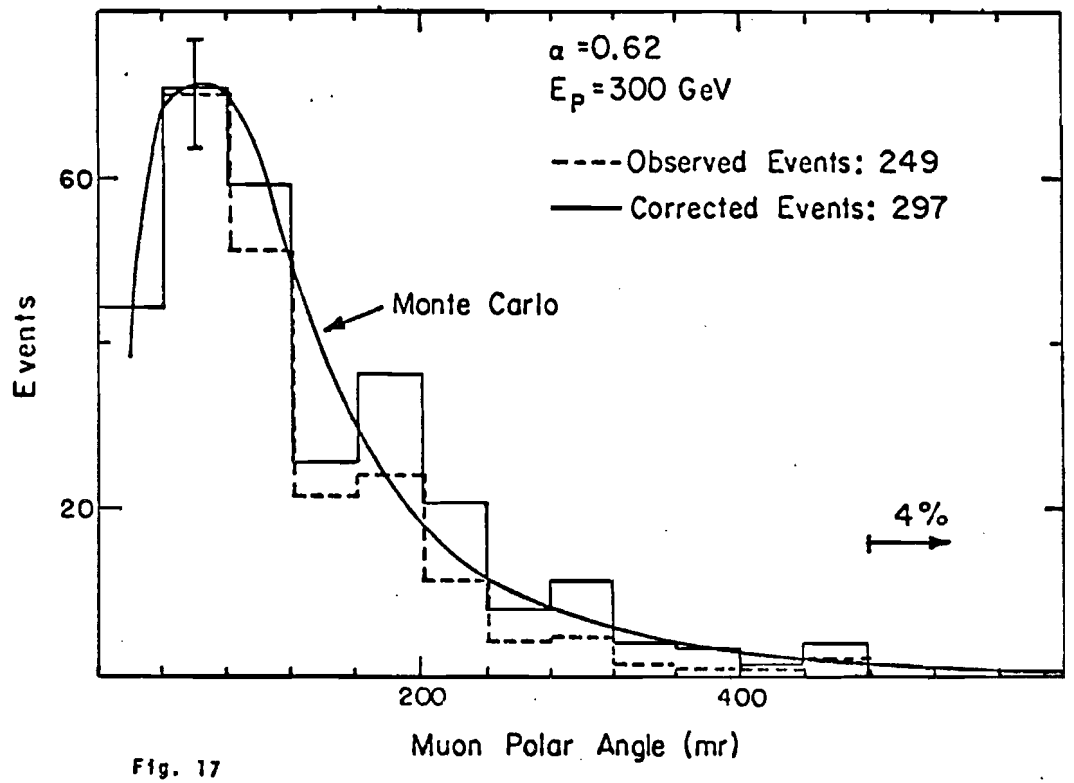

Fig. 17

1580825

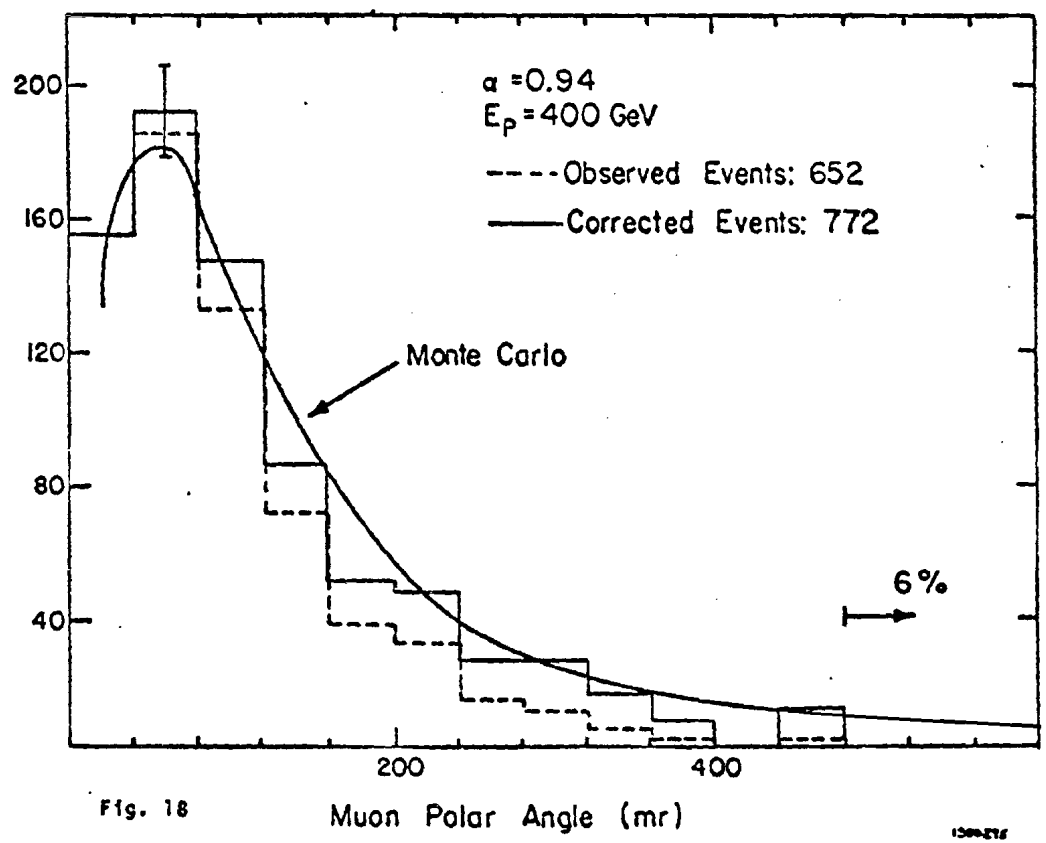
α =0.94
E_p =400 GeV
----Observed Events: 652
——Corrected Events: 772
Monte Carlo
6%
200
160
120
80
40
200
400
Muon Polar Angle (mr)

Fig. 18

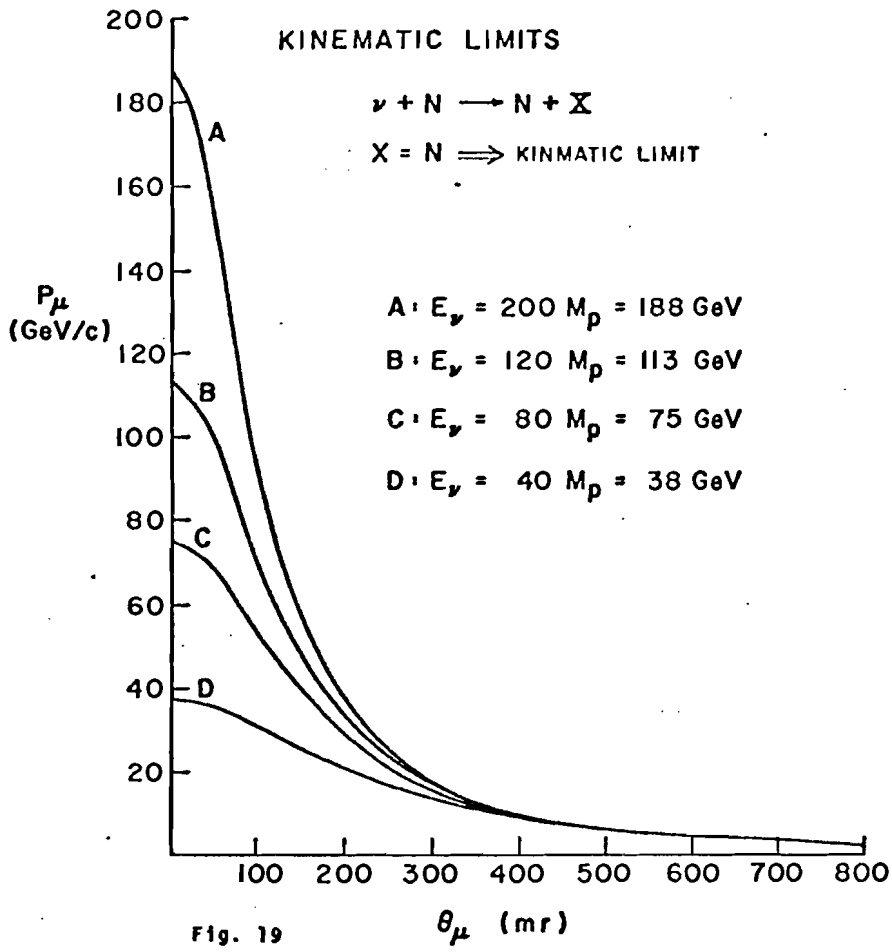
KINEMATIC LIMITS
ν + N → N + X
X = N ⟹ KINMATIC LIMIT
A : Eν = 200 Mp = 188 GeV
B : Eν = 120 Mp = 113 GeV
C : Eν = 80 Mp = 75 GeV
D : Eν = 40 Mp = 38 GeV
Pμ (GeV/c)
200
180
160
140
120
100
80
60
40
20
A
B
C
D
100
200
300
400
500
600
700
800
θμ (mr)

Fig. 19

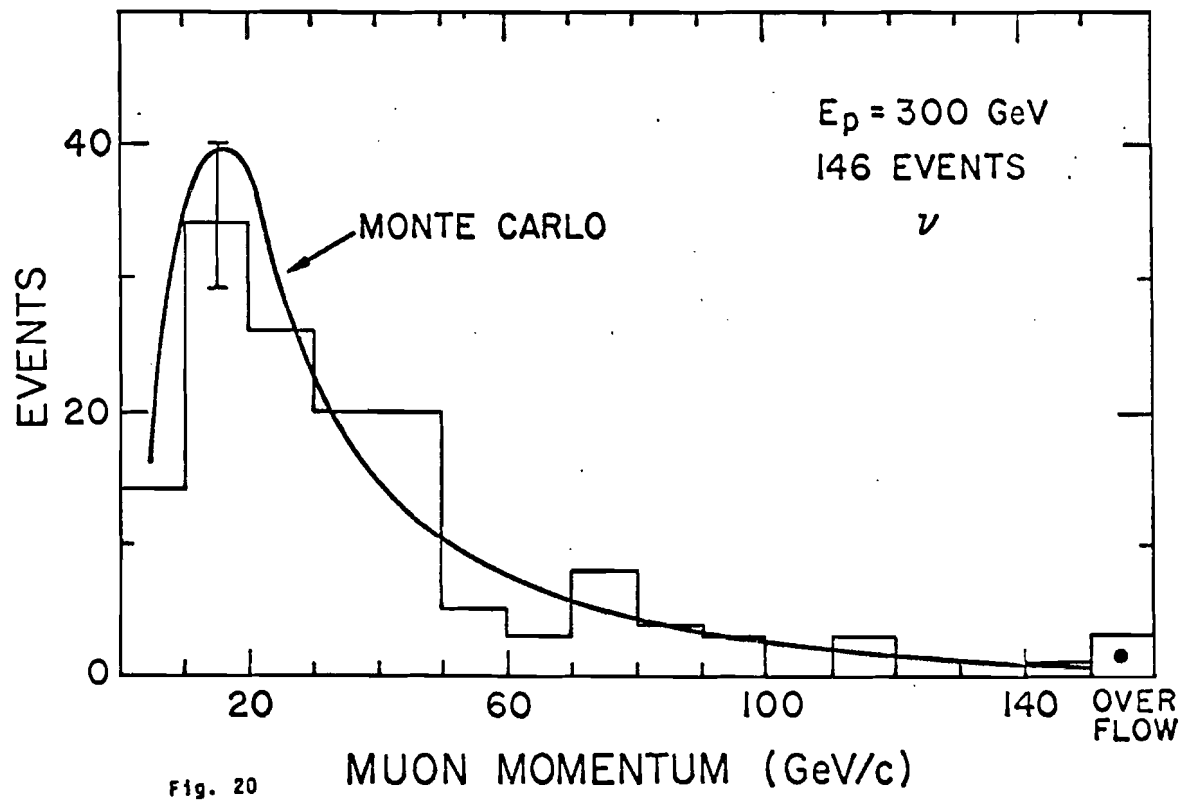
E_p = 300 GeV
146 EVENTS
ν
MONTE CARLO
EVENTS
40
20
0
20
60
100
140
OVER FLOW
MUON MOMENTUM (GeV/c)

Fig. 20

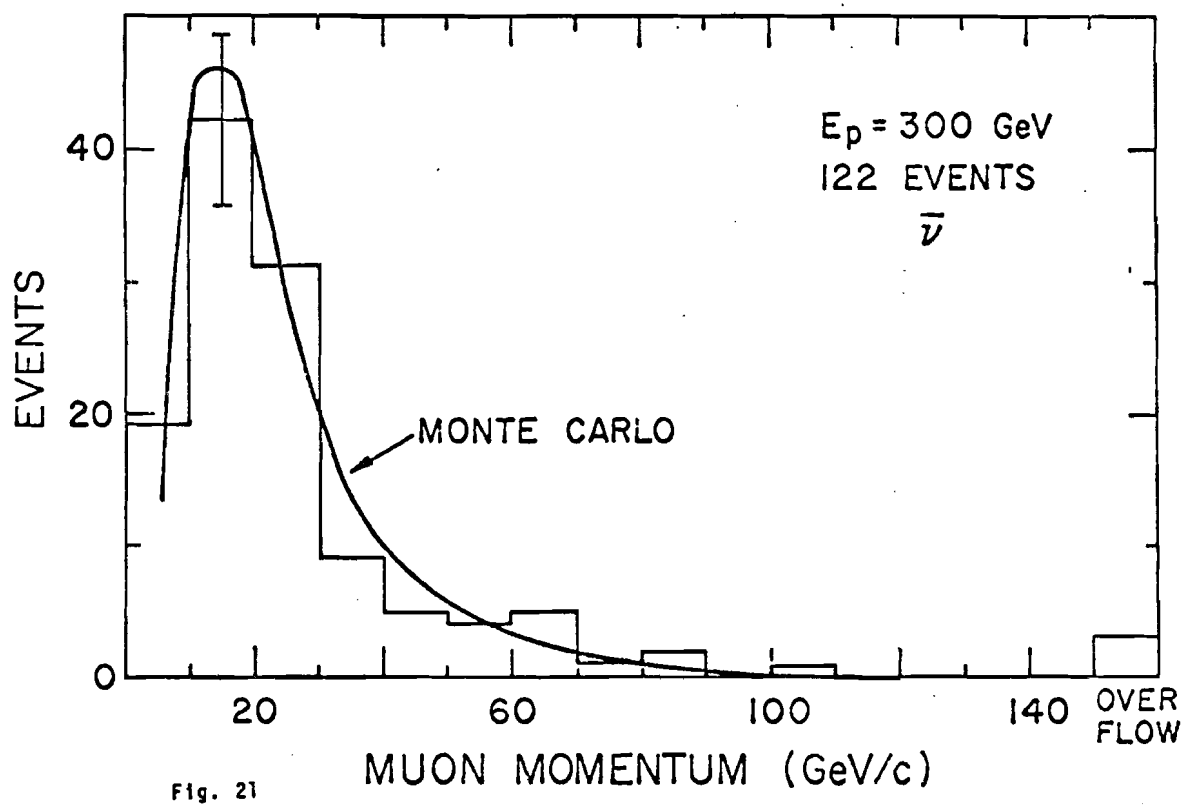
EVENTS
40
20
0
20
60
100
140
OVER FLOW
MUON MOMENTUM (GeV/c)
E_p = 300 GeV
122 EVENTS
$\bar{\nu}$
MONTE CARLO

Fig. 21

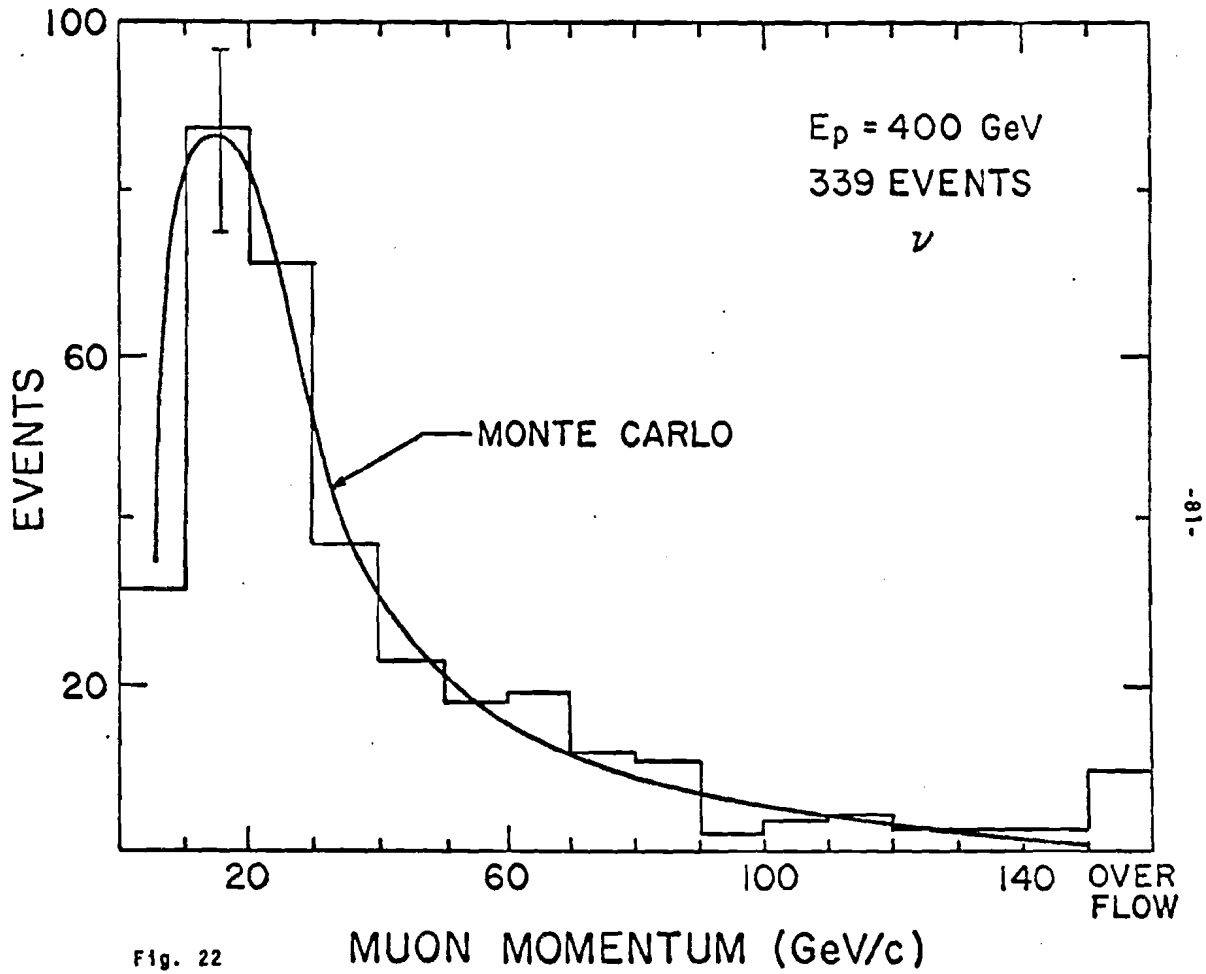
100
60
20
EVENTS
E_p = 400 GeV
339 EVENTS
ν
MONTE CARLO
20
60
100
140
OVER FLOW
MUON MOMENTUM (GeV/c)

Fig. 22

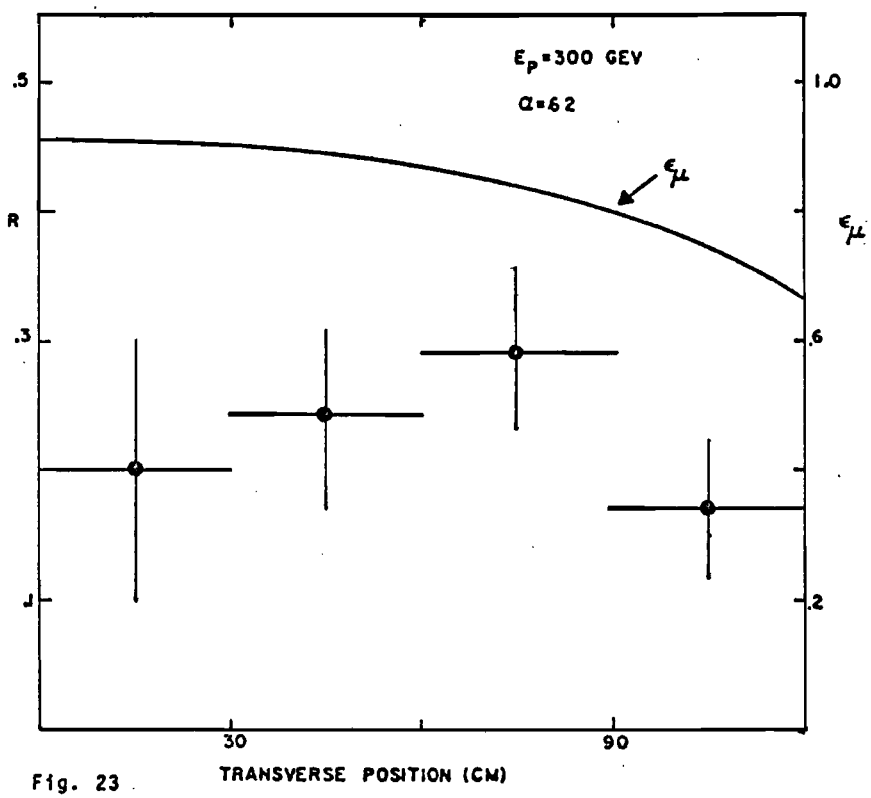
E_p=300 GEV
α=62
ϵ_μ
R
.5
.3
.1
1.0
.6
.2
30
90
TRANSVERSE POSITION (CM)

Fig. 23

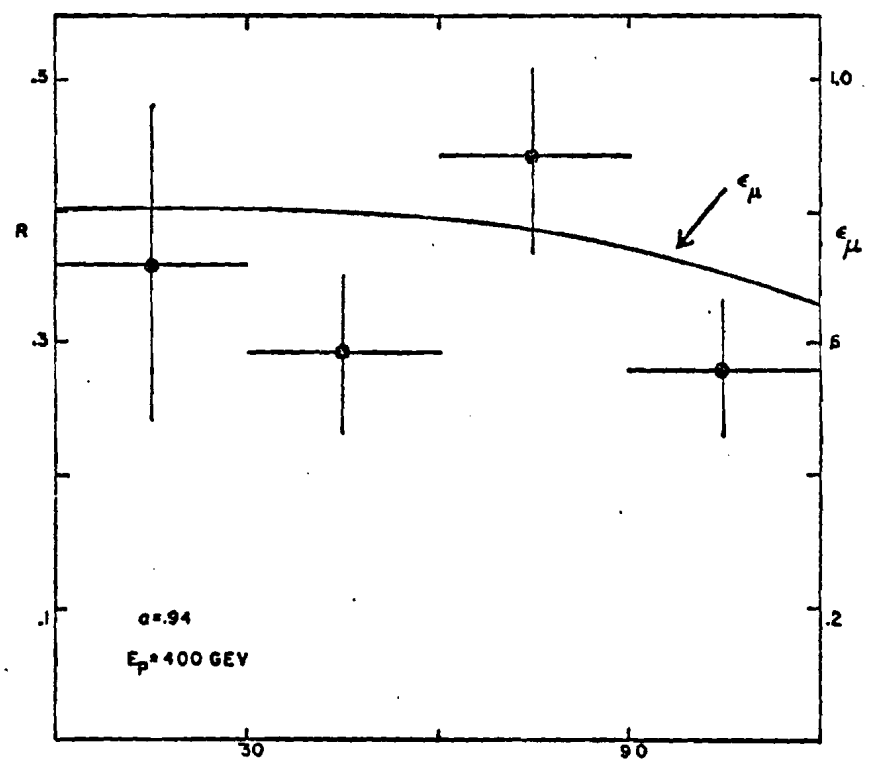

Fig. 24 TRANSVERSE POSITION (CM)

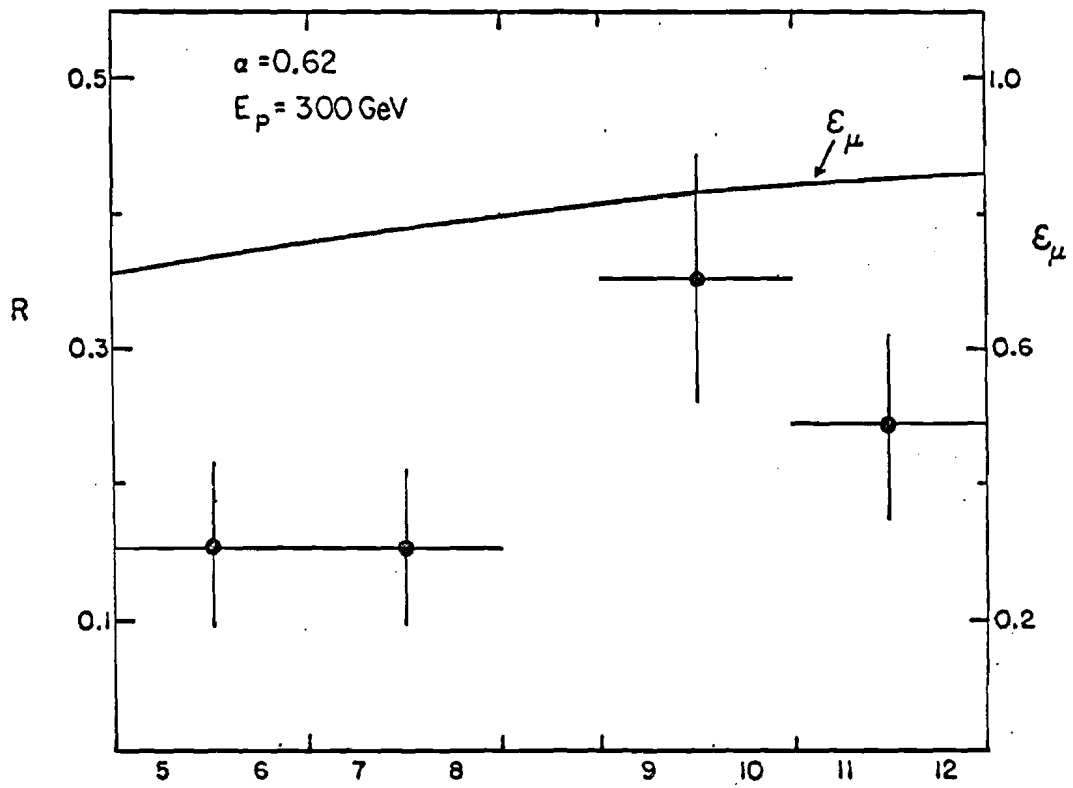
α =0.62
E_p = 300 GeV
ε_μ
R
0.5
0.3
0.1
1.0
0.6
0.2
5
6
7
8
9
10
11
12
Z (Calorimeter Module Number)

Fig. 25

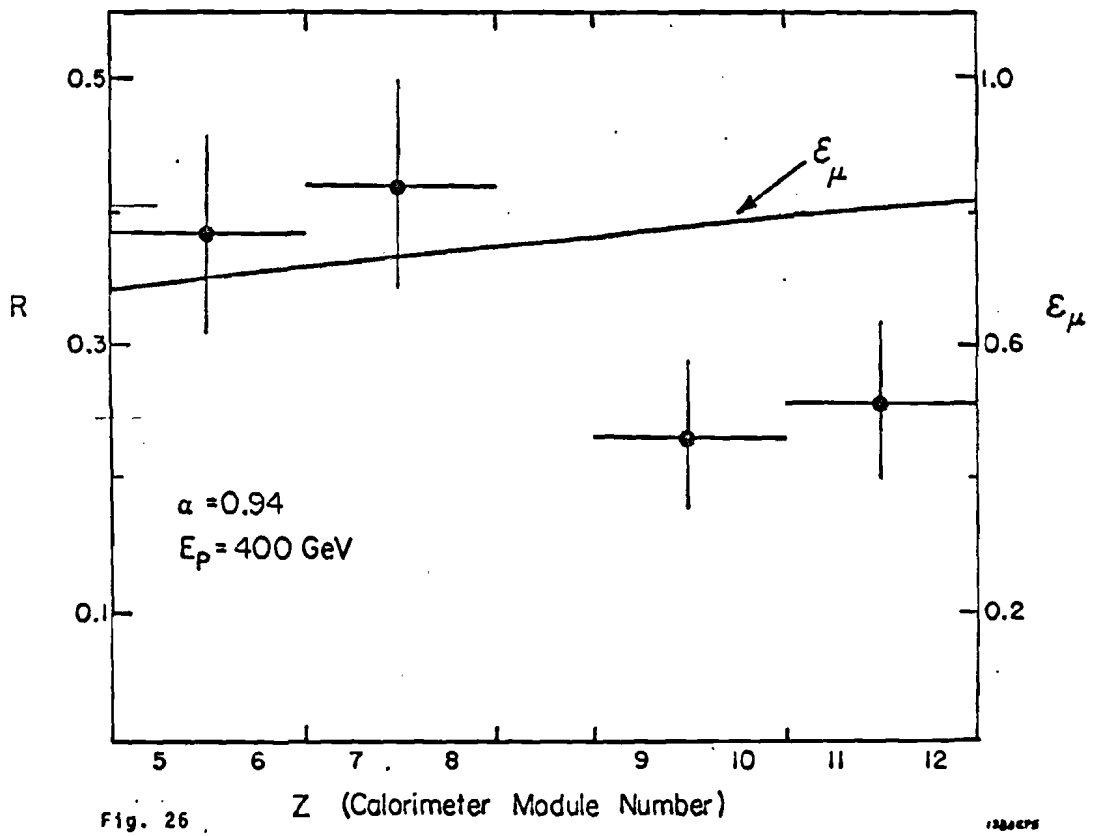
0.5
0.3
0.1
R
1.0
0.6
0.2
ε_μ
ε_μ
α =0.94
E_p = 400 GeV
5
6
7
8
9
10
11
12
Z (Calorimeter Module Number)

Fig. 26

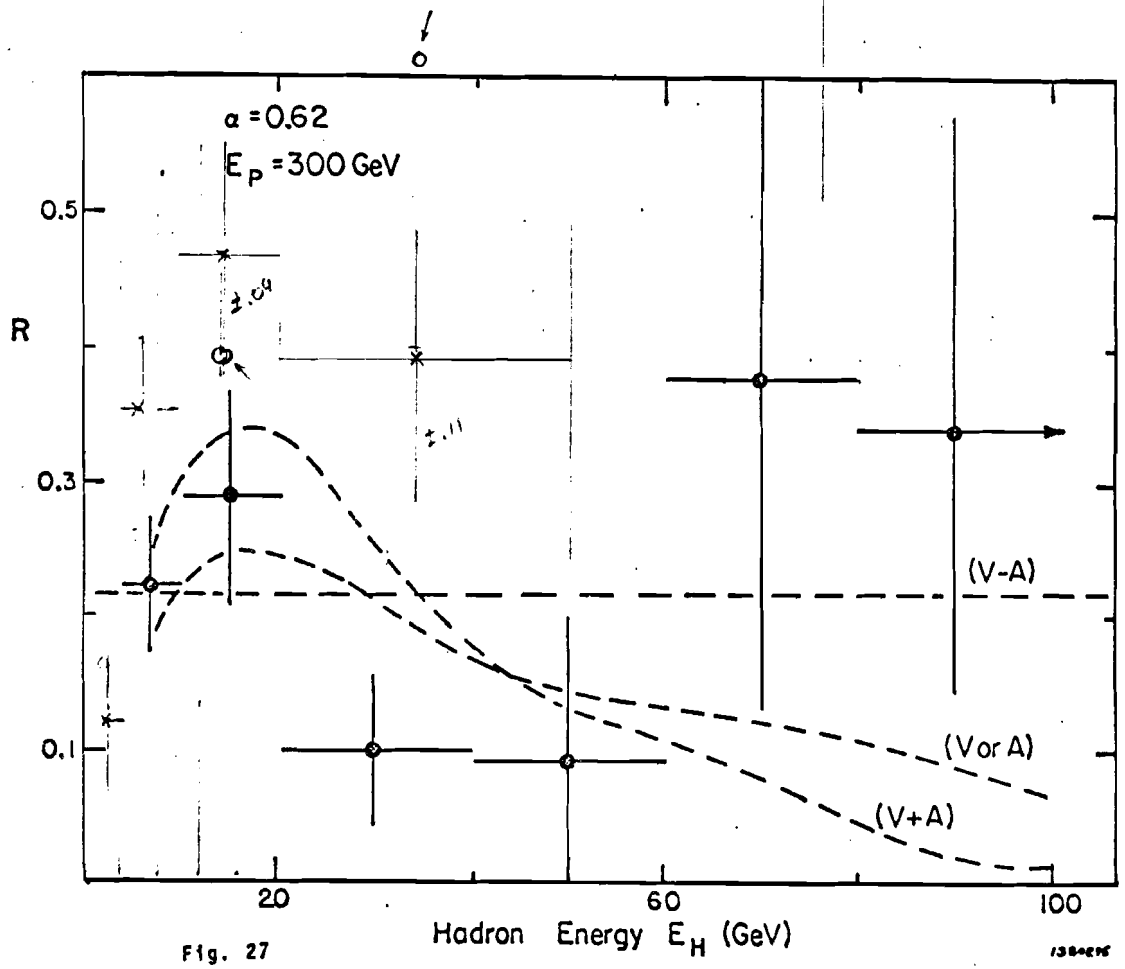

Fig. 27

R

o SC6
× B+SC5

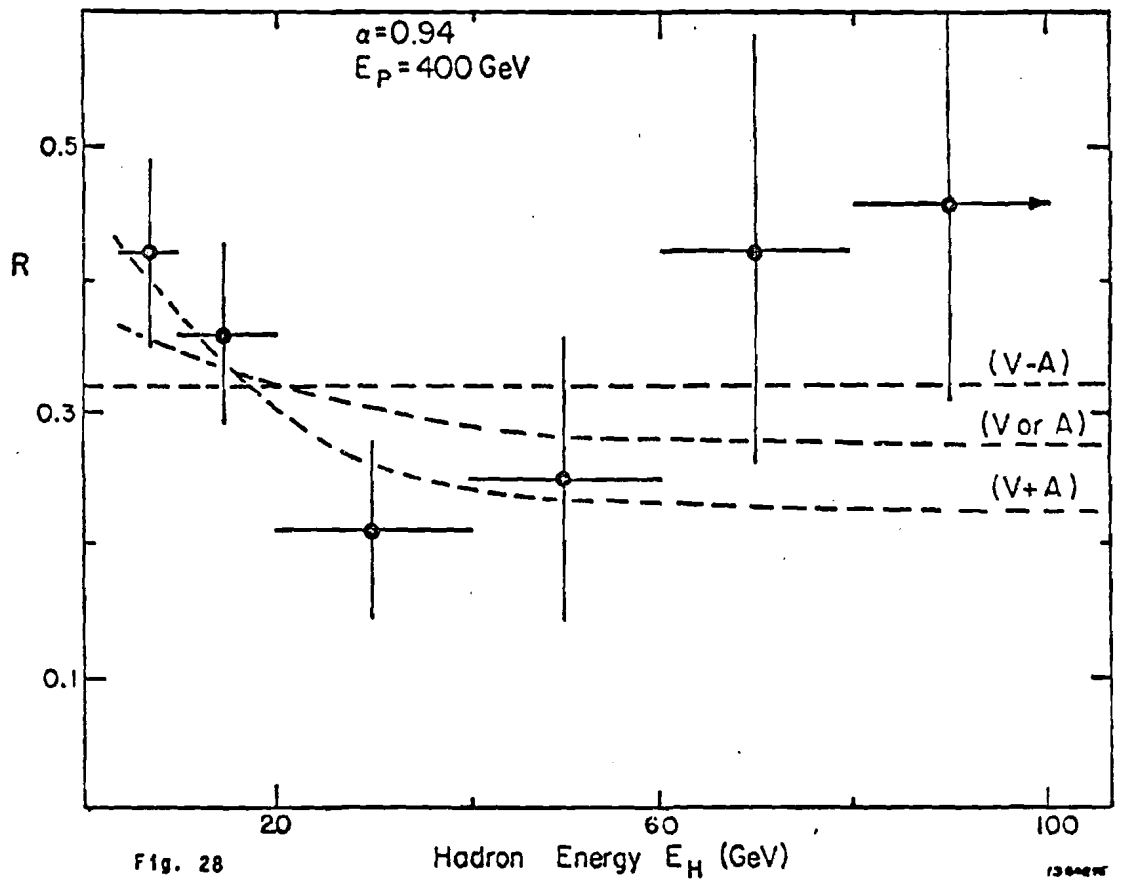
α=0.94
E_P = 400 GeV
0.5
R
0.3
0.1
(V-A)
(V or A)
(V+A)
20
60
100
Hadron Energy E_H (GeV)

Fig. 28

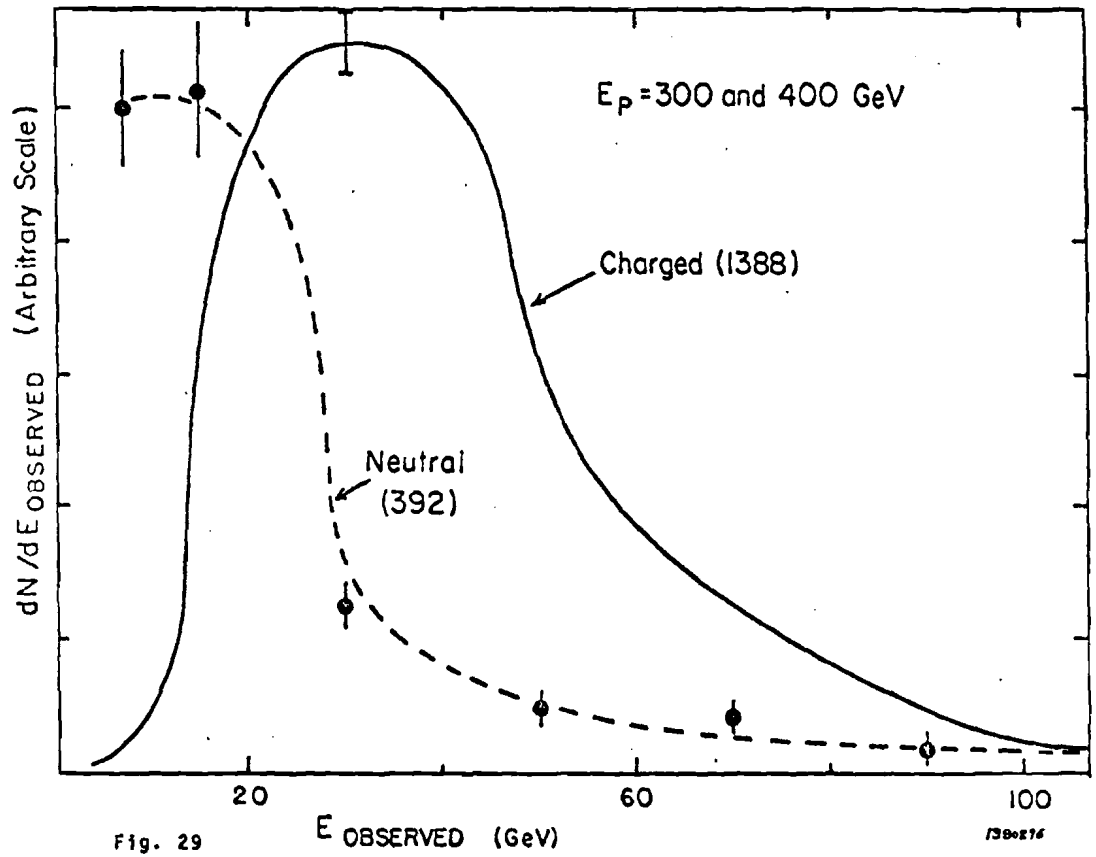
E_p = 300 and 400 GeV
Charged (1388)
Neutral
(392)
dN/dE OBSERVED (Arbitrary Scale)
20
60
100
E OBSERVED (GeV)

Fig. 29

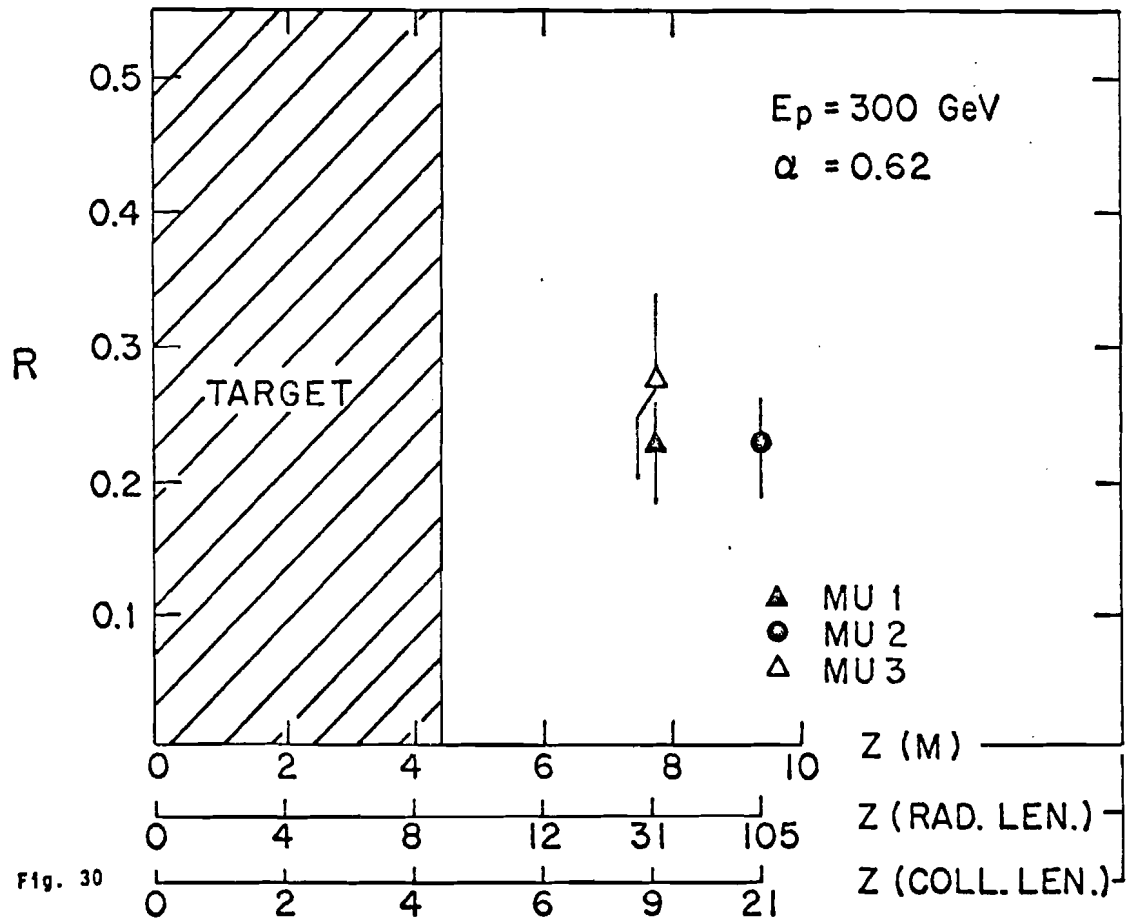
R
0.5
0.4
0.3
0.2
0.1
TARGET
Ep = 300 GeV
α = 0.62
MU 1
MU 2
MU 3
0 2 4 6 8 10
Z (M)
0 4 8 12 31 105
Z (RAD. LEN.)
0 2 4 6 9 21
Z (COLL. LEN.)

Fig. 30

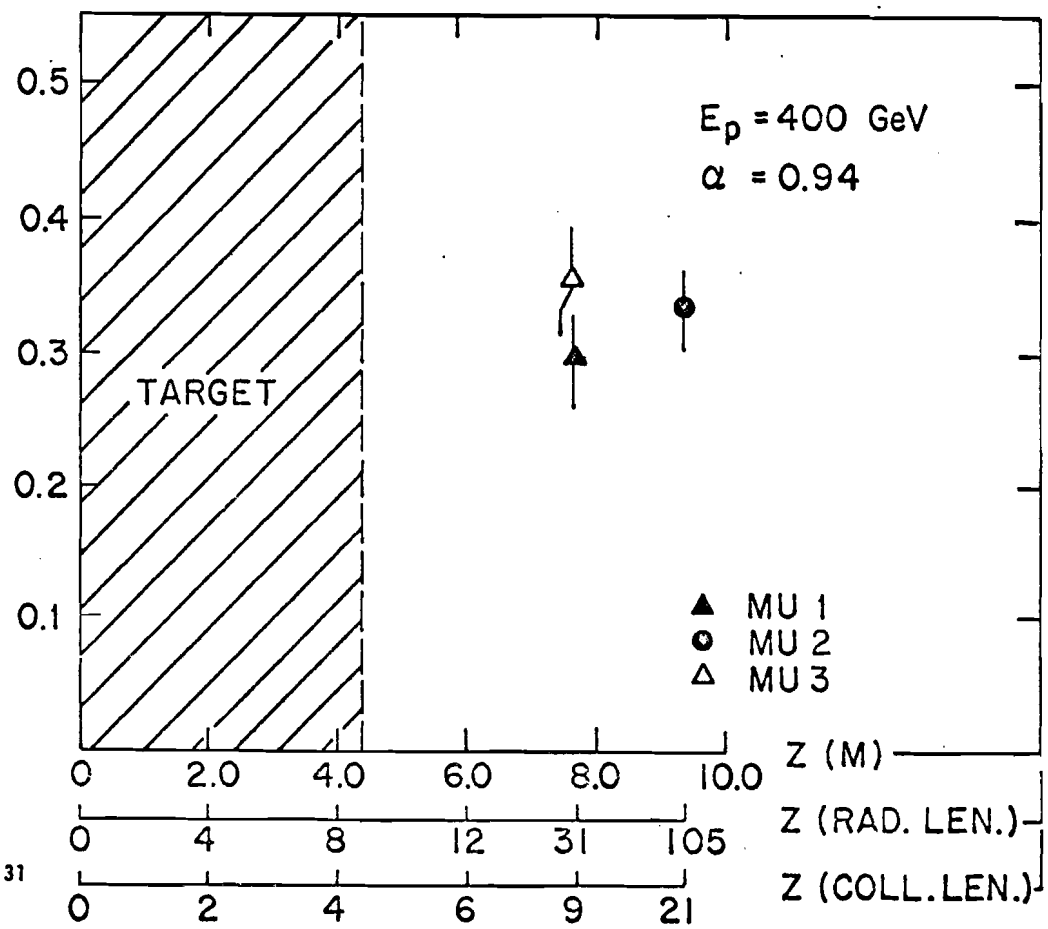
0.5
0.4
0.3
0.2
0.1
TARGET
E_p = 400 GeV
α = 0.94
MU 1
MU 2
MU 3
0
2.0
4.0
6.0
8.0
10.0
Z (M)
0
4
8
12
31
105
Z (RAD. LEN.)
0
2
4
6
9
21
Z (COLL. LEN.)

Fig. 31

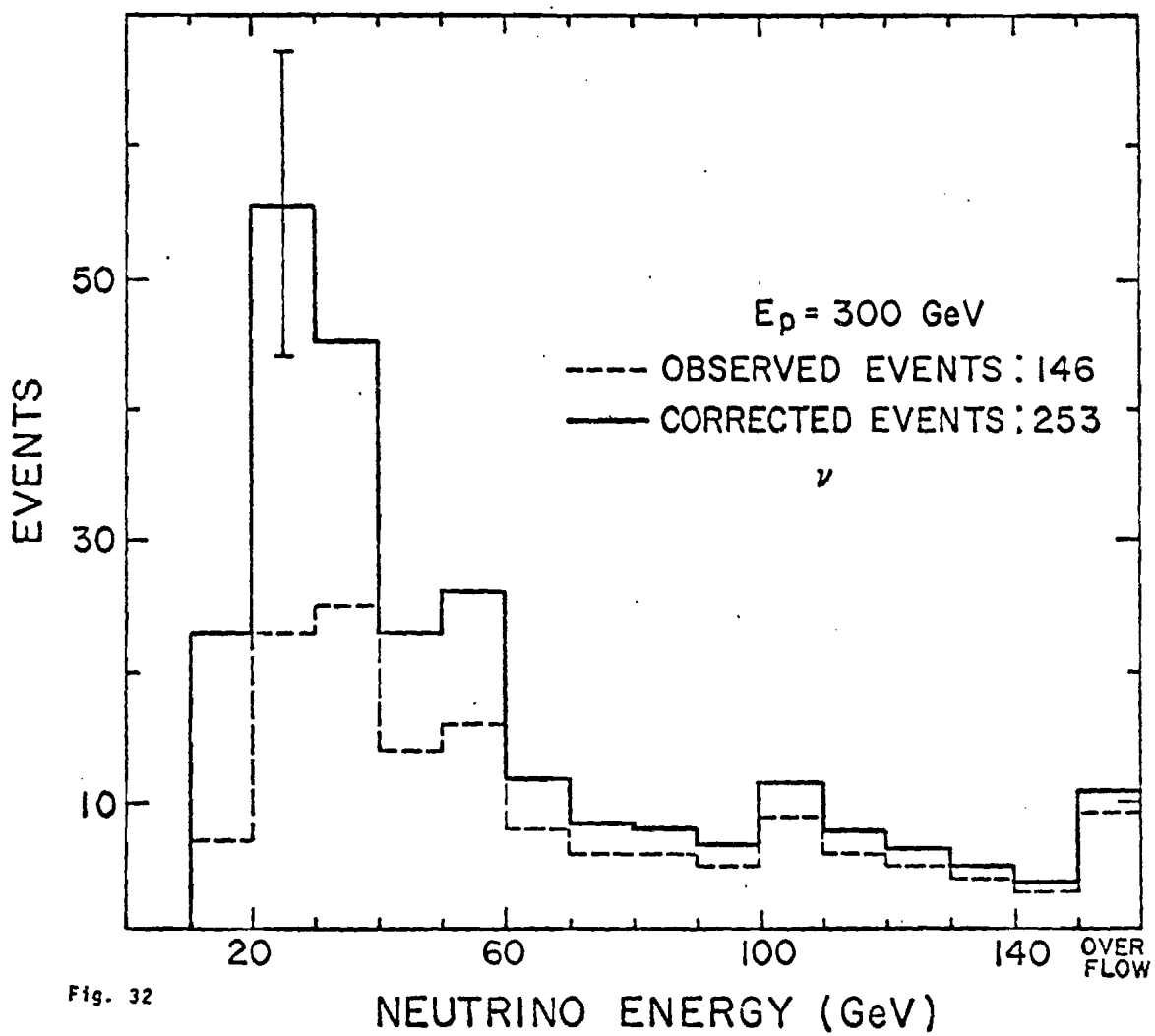
EVENTS
50
30
10
20
60
100
140
OVER FLOW
NEUTRINO ENERGY (GeV)
E_p = 300 GeV
---- OBSERVED EVENTS : 146
—— CORRECTED EVENTS : 253
ν

Fig. 32

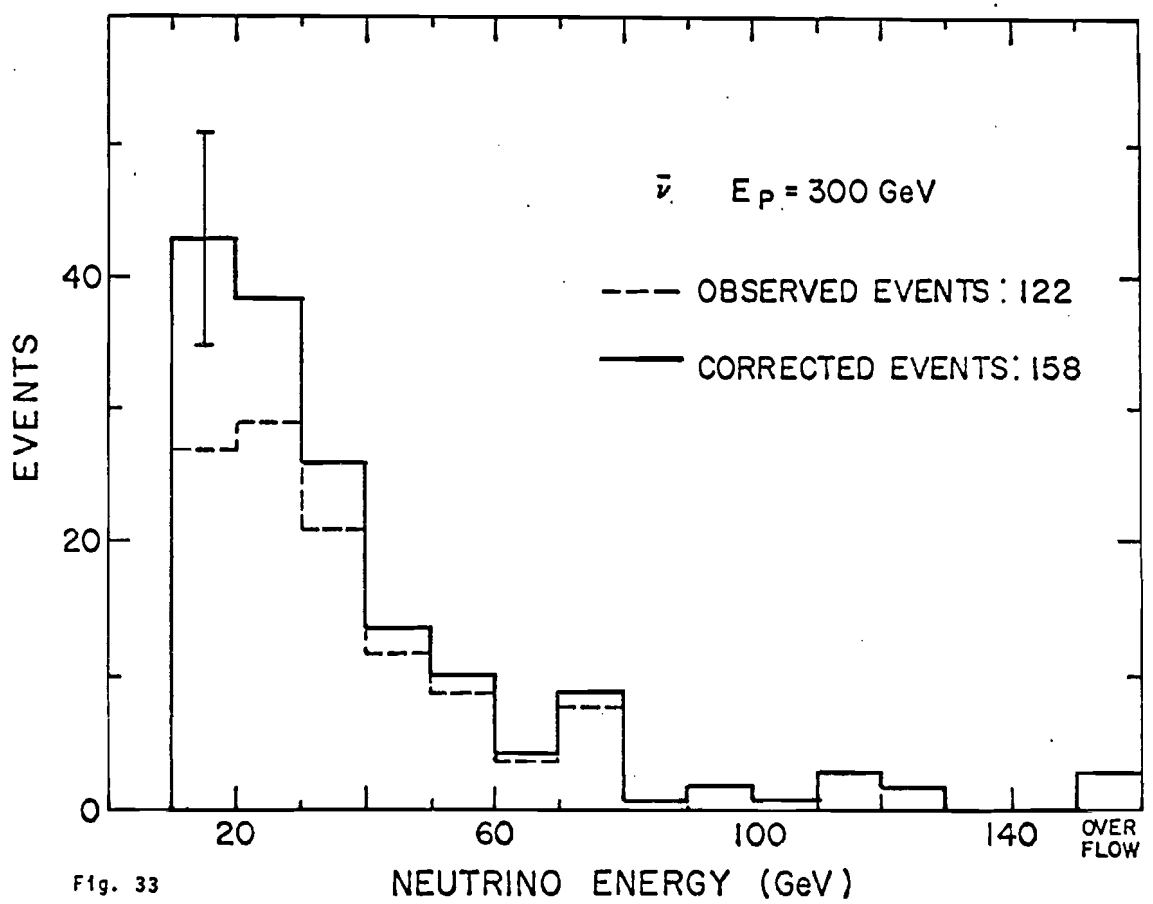
$\bar{\nu}$ E_p = 300 GeV
OBSERVED EVENTS : 122
CORRECTED EVENTS: 158
EVENTS
0
20
40
20
60
100
140
OVER FLOW
NEUTRINO ENERGY (GeV)

Fig. 33

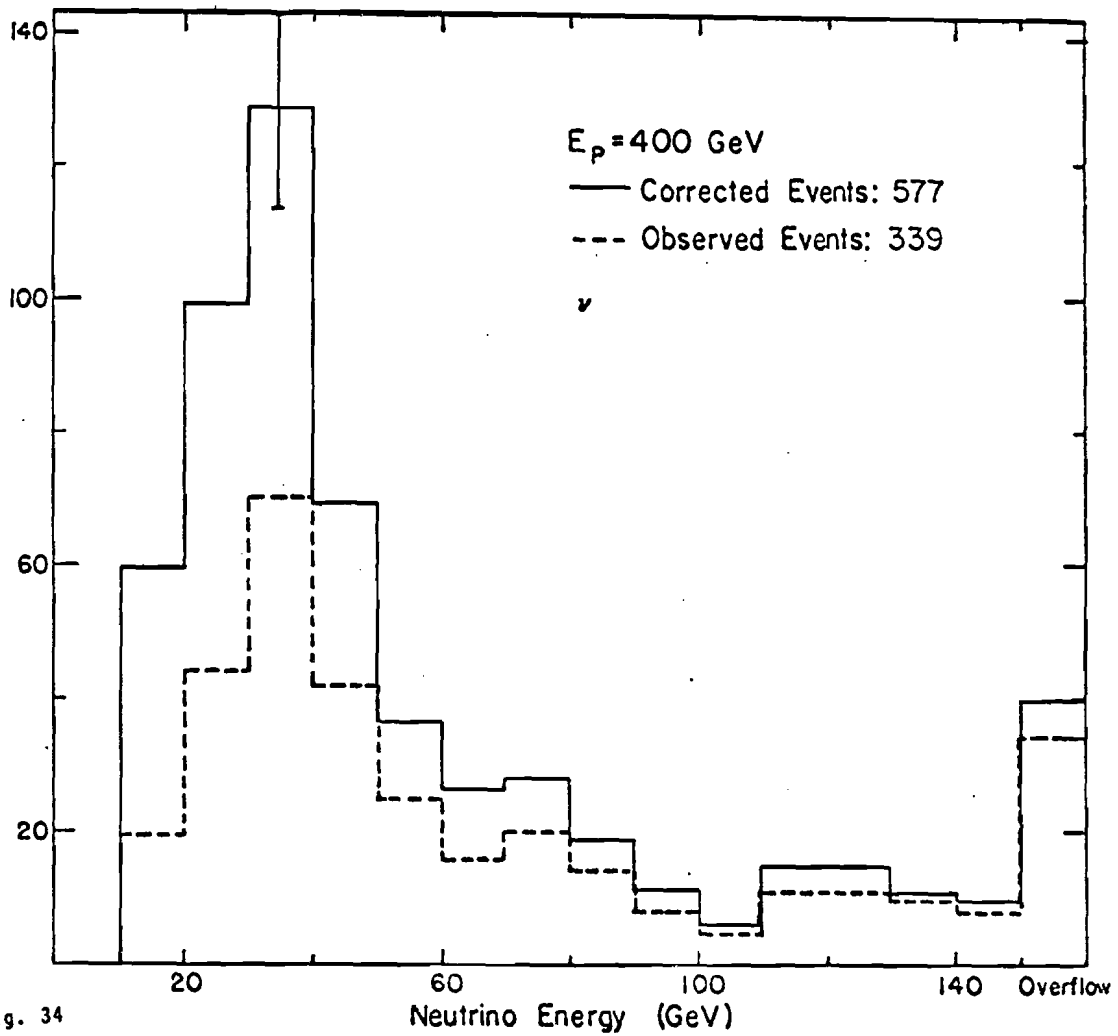
140
100
60
20
E_p=400 GeV
Corrected Events: 577
Observed Events: 339
ν
20
60
100
140
Overflow
Neutrino Energy (GeV)

Fig. 34

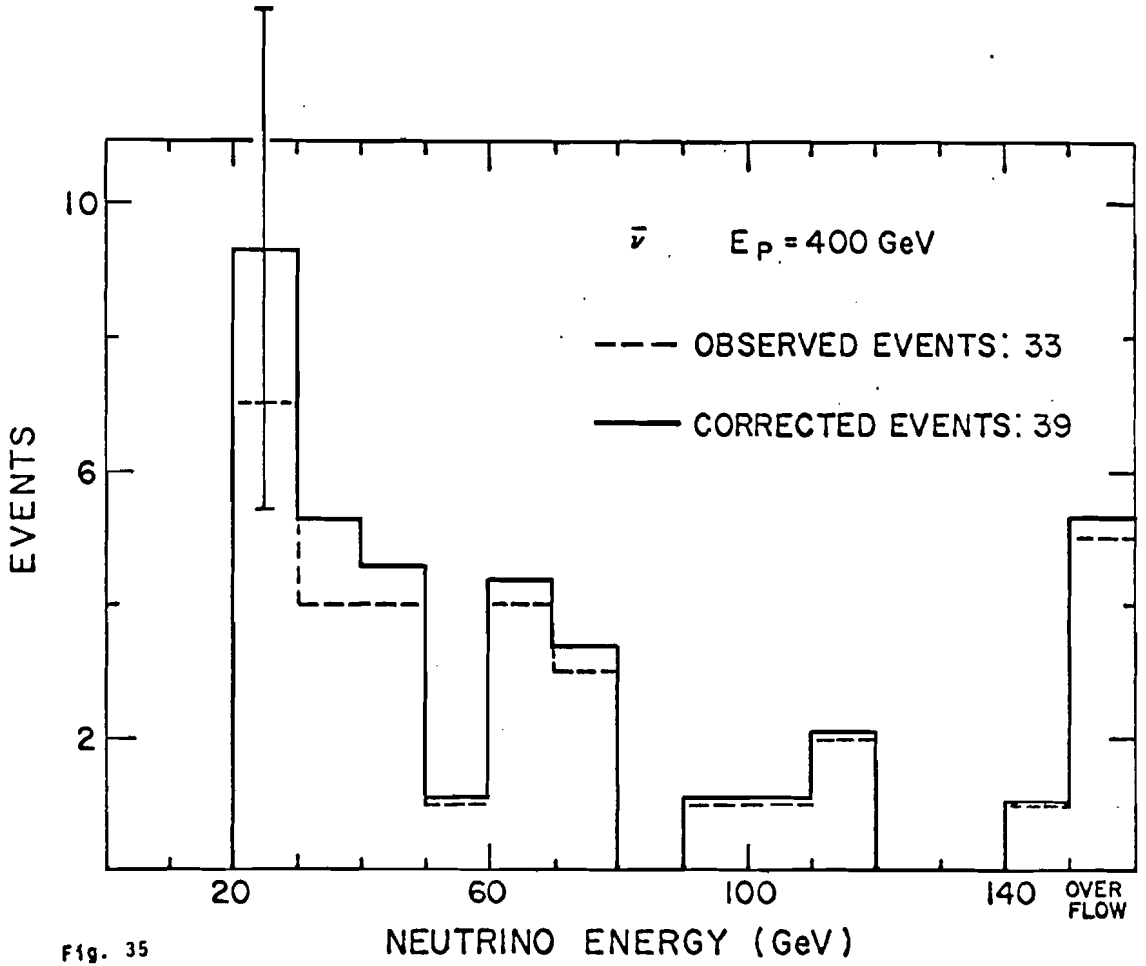
$\bar{\nu}$ $E_p = 400$ GeV
OBSERVED EVENTS: 33
CORRECTED EVENTS: 39
EVENTS
10
6
2
20
60
100
140
OVER FLOW
NEUTRINO ENERGY (GeV)

Fig. 35

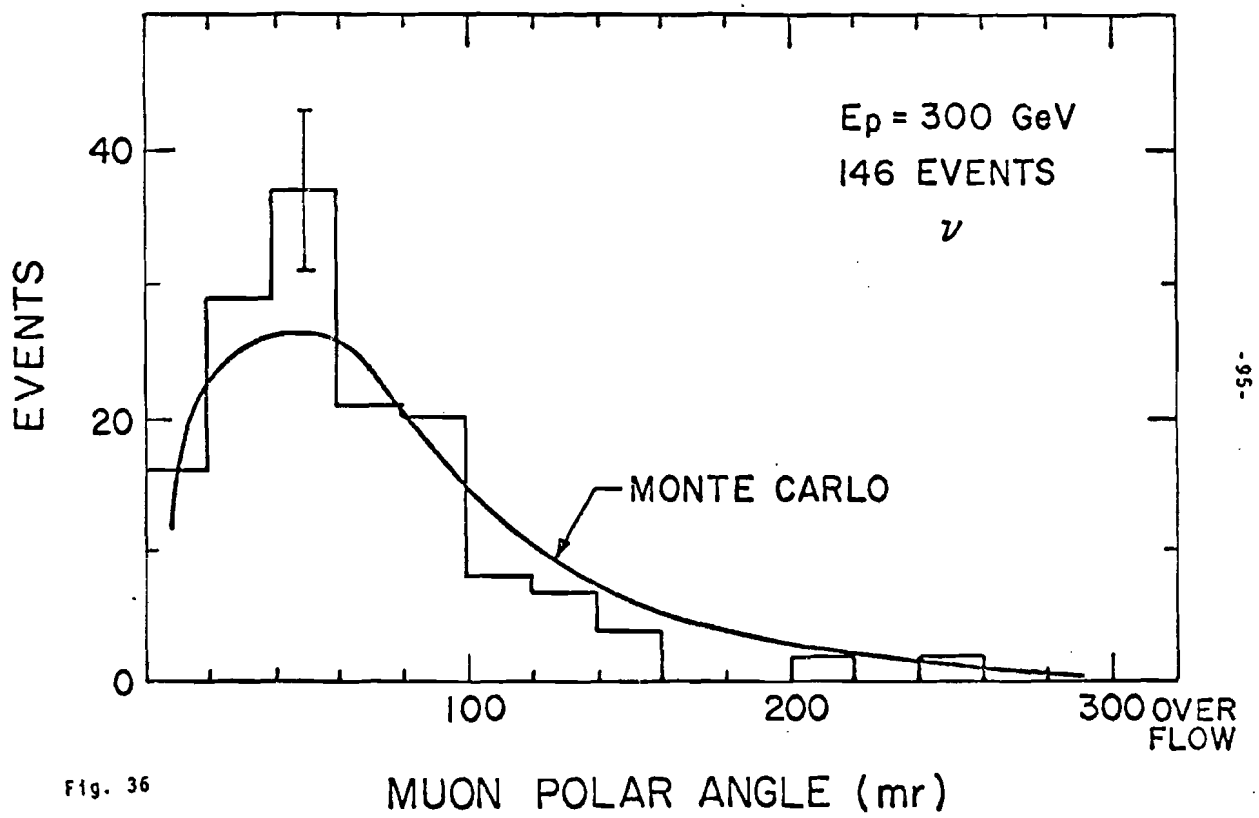
Ep = 300 GeV
146 EVENTS
ν
MONTE CARLO
EVENTS
40
20
0
100
200
300 OVER FLOW
MUON POLAR ANGLE (mr)

Fig. 36

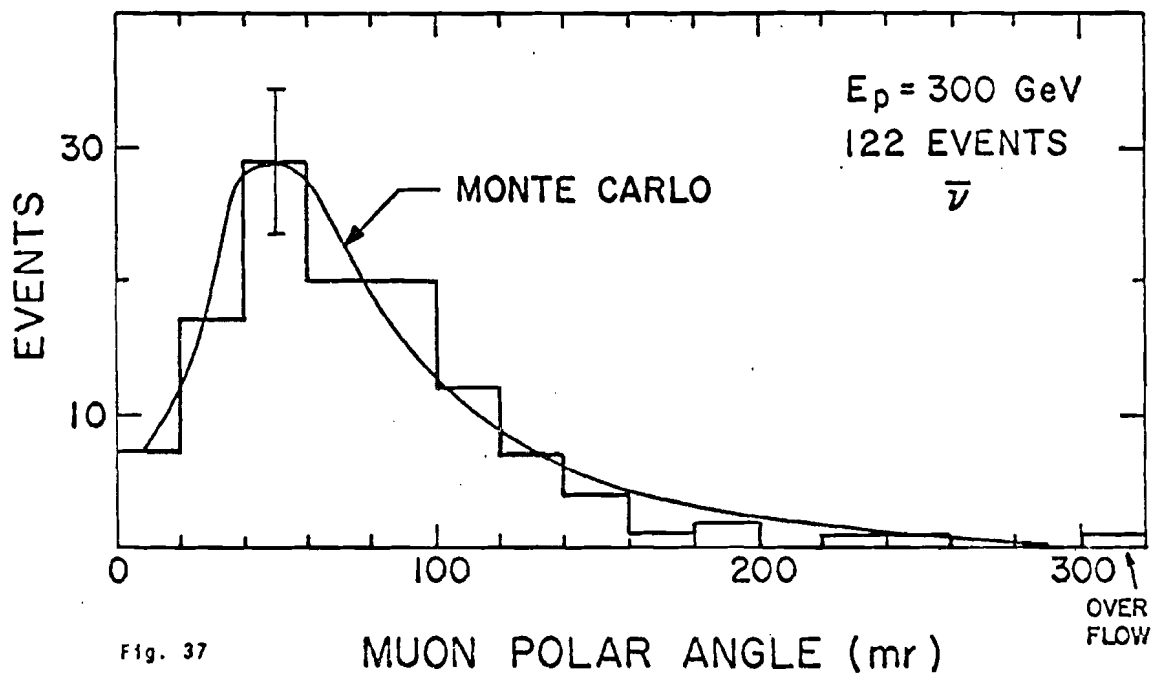
E_p = 300 GeV
122 EVENTS
$\bar{\nu}$
MONTE CARLO
EVENTS
30
10
0
100
200
300
OVER FLOW
MUON POLAR ANGLE (mr)

Fig. 37

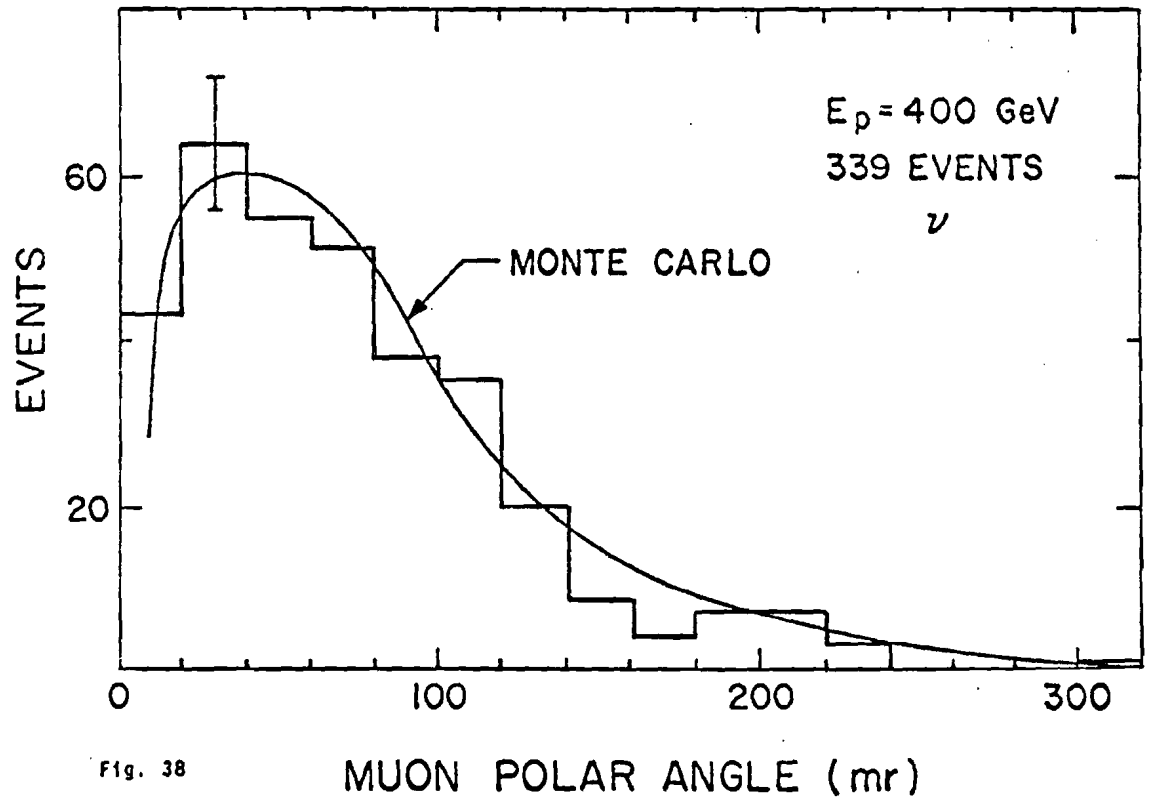
$E_p = 400$ GeV
339 EVENTS
ν
MONTE CARLO
EVENTS
60
20
0
100
200
300
MUON POLAR ANGLE (mr)

Fig. 38

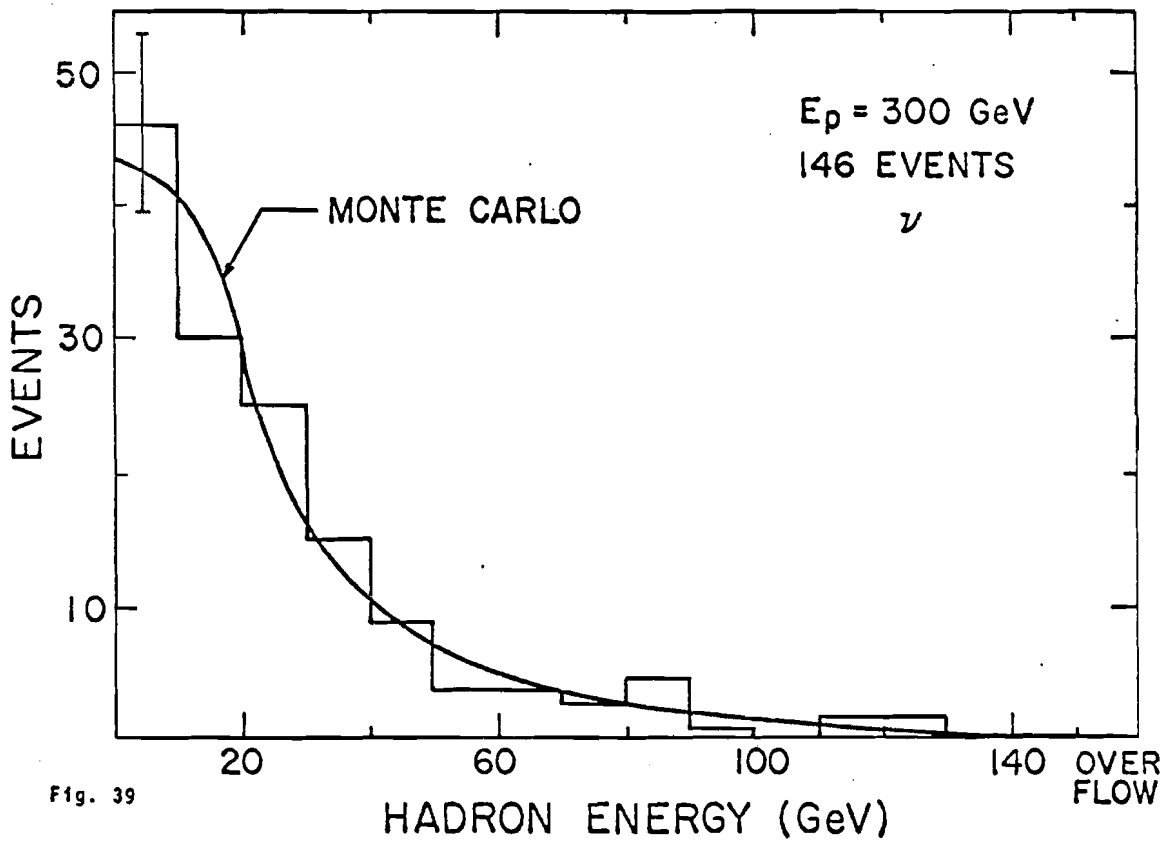
50
30
10
EVENTS
MONTE CARLO
E_p = 300 GeV
146 EVENTS
ν
20
60
100
140
OVER FLOW
HADRON ENERGY (GeV)

Fig. 39

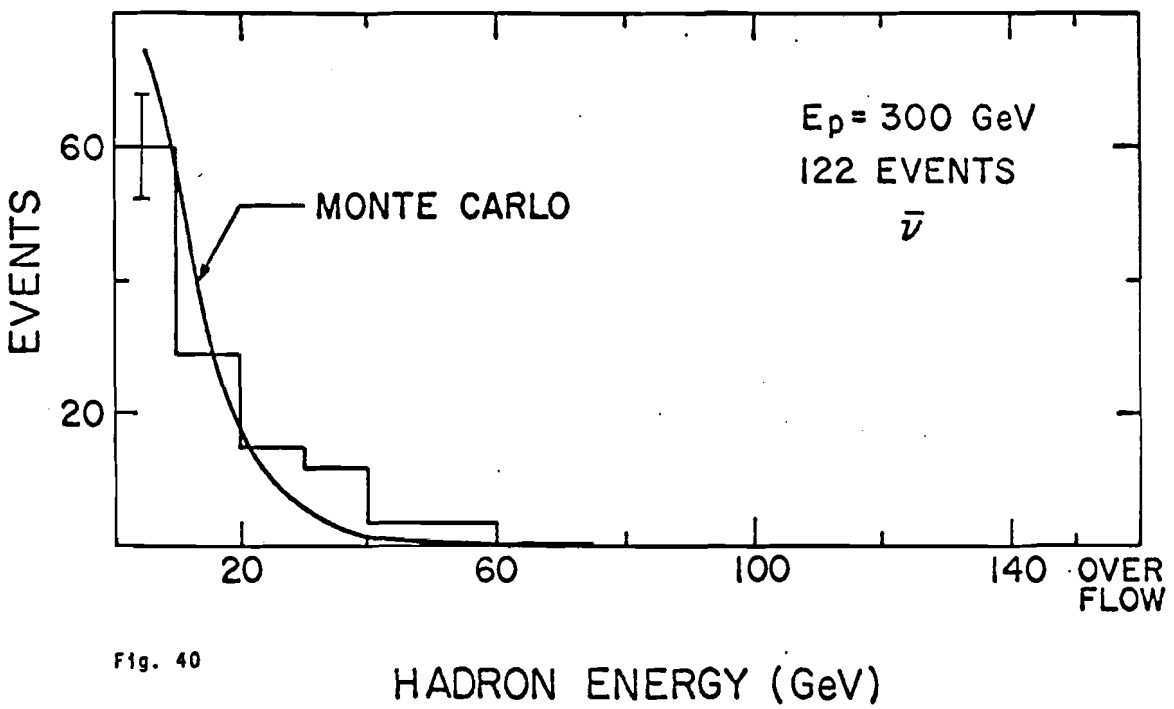
EVENTS
60
20
MONTE CARLO
Ep = 300 GeV
122 EVENTS
$\bar{\nu}$
20
60
100
140
OVER FLOW
HADRON ENERGY (GeV)

Fig. 40

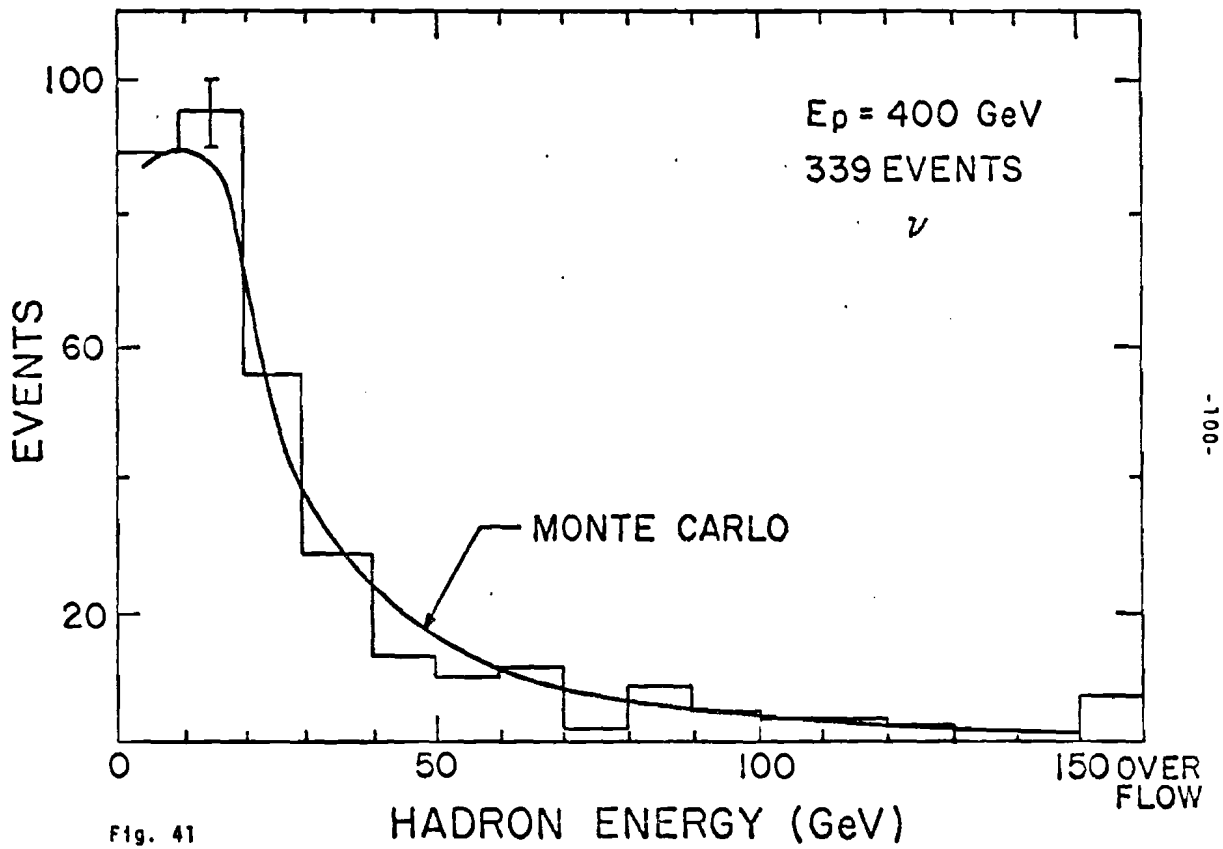
Ep = 400 GeV
339 EVENTS
ν
MONTE CARLO
EVENTS
100
60
20
0
50
100
150 OVER FLOW
HADRON ENERGY (GeV)

Fig. 41

Proton Energy (E_p)	400 GeV	300 GeV
Charge of hadrons focussed by horn	+	-
Reconstructed μ^+	33	122
Reconstructed μ^-	339	146
Corrected μ^+	39	158
Corrected μ^-	577	253
Ratio of neutrino events to antineutrino events = $\bar{\nu}/\nu$	.07±.01	.62±.06
$\alpha = \frac{\nu}{\bar{\nu}+\nu}$	.94±.01	.62±.03

Fig. 42

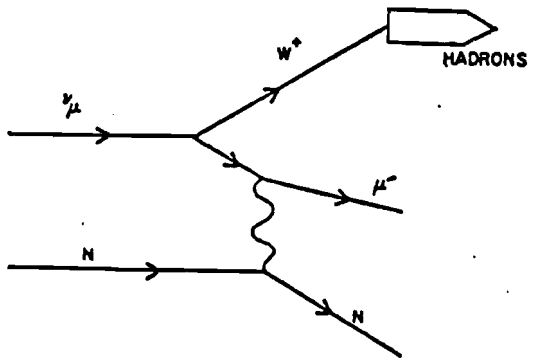

W PRODUCTION

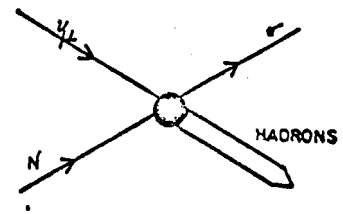

MUON NUMBER NOT CONSERVED

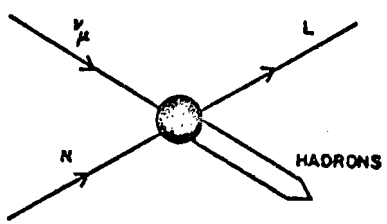

HEAVY LEPTON PRODUCTION

Fig. 43

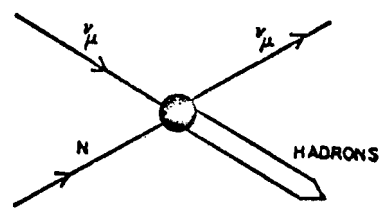

WEAK NEUTRAL CURRENT

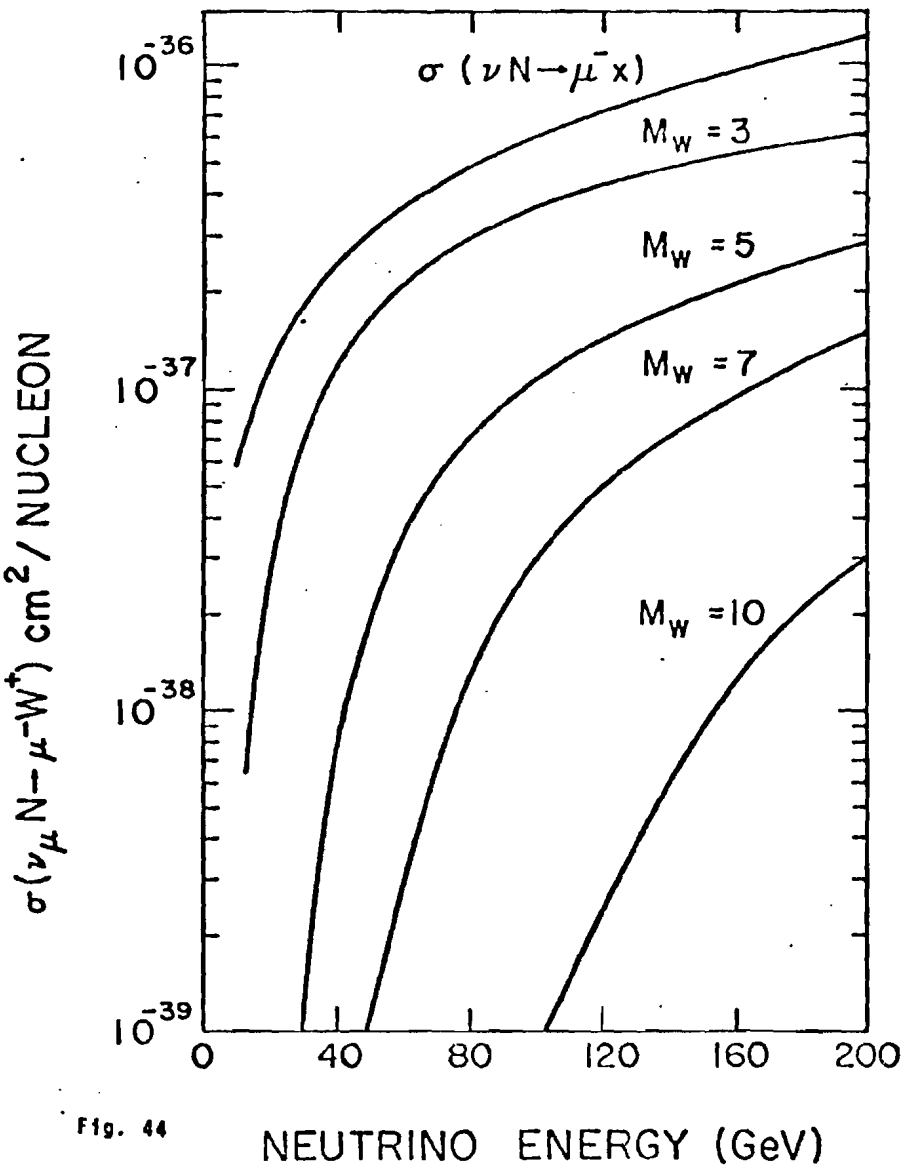
σ (νN→μ⁻x)
M_W = 3
M_W = 5
M_W = 7
M_W = 10
10⁻³⁶
10⁻³⁷
10⁻³⁸
10⁻³⁹
σ(ν_μ N→μ⁻W⁺) cm²/NUCLEON
0
40
80
120
160
200
NEUTRINO ENERGY (GeV)

Fig. 44

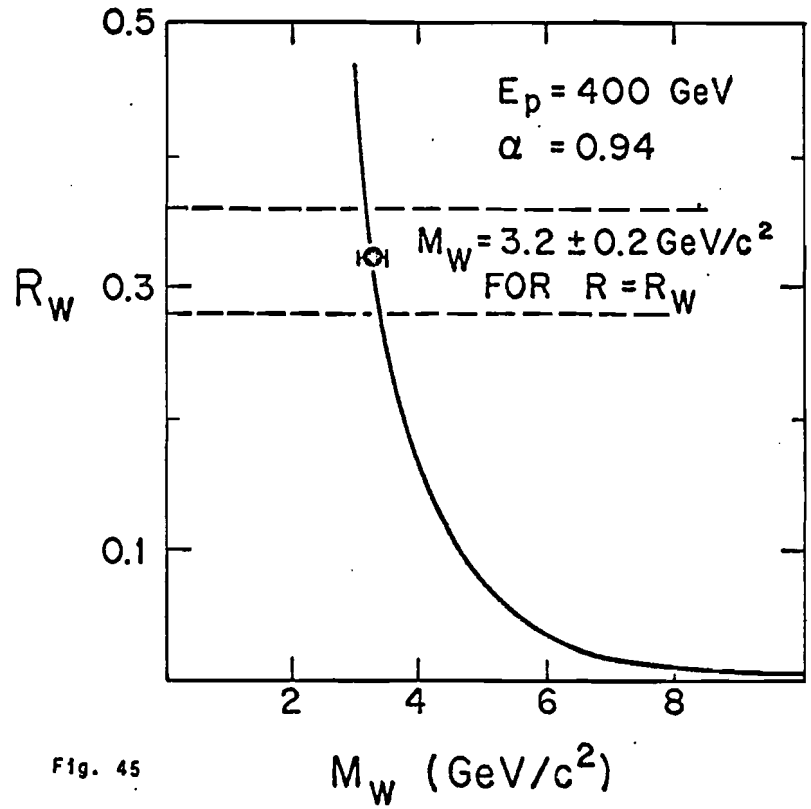
0.5
0.3
0.1
R_W
$E_p = 400$ GeV
$\alpha = 0.94$
$M_W = 3.2 \pm 0.2$ GeV/c^2
FOR $R = R_W$
2
4
6
8
M_W (GeV/c^2)

Fig. 45

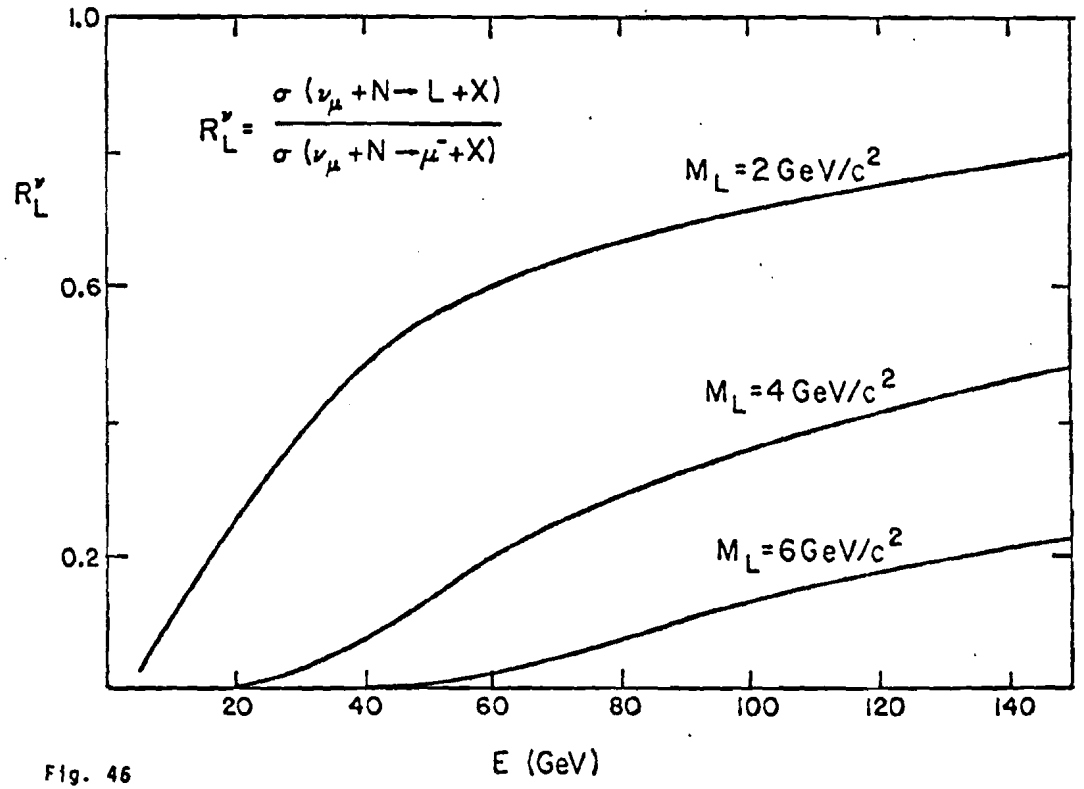
1.0
0.6
0.2
R_L^ν
$R_L^\nu = \frac{\sigma(\nu_\mu + N \to L + X)}{\sigma(\nu_\mu + N \to \mu^- + X)}$
$M_L = 2\ GeV/c^2$
$M_L = 4\ GeV/c^2$
$M_L = 6\ GeV/c^2$
20
40
60
80
100
120
140
E (GeV)

Fig. 46

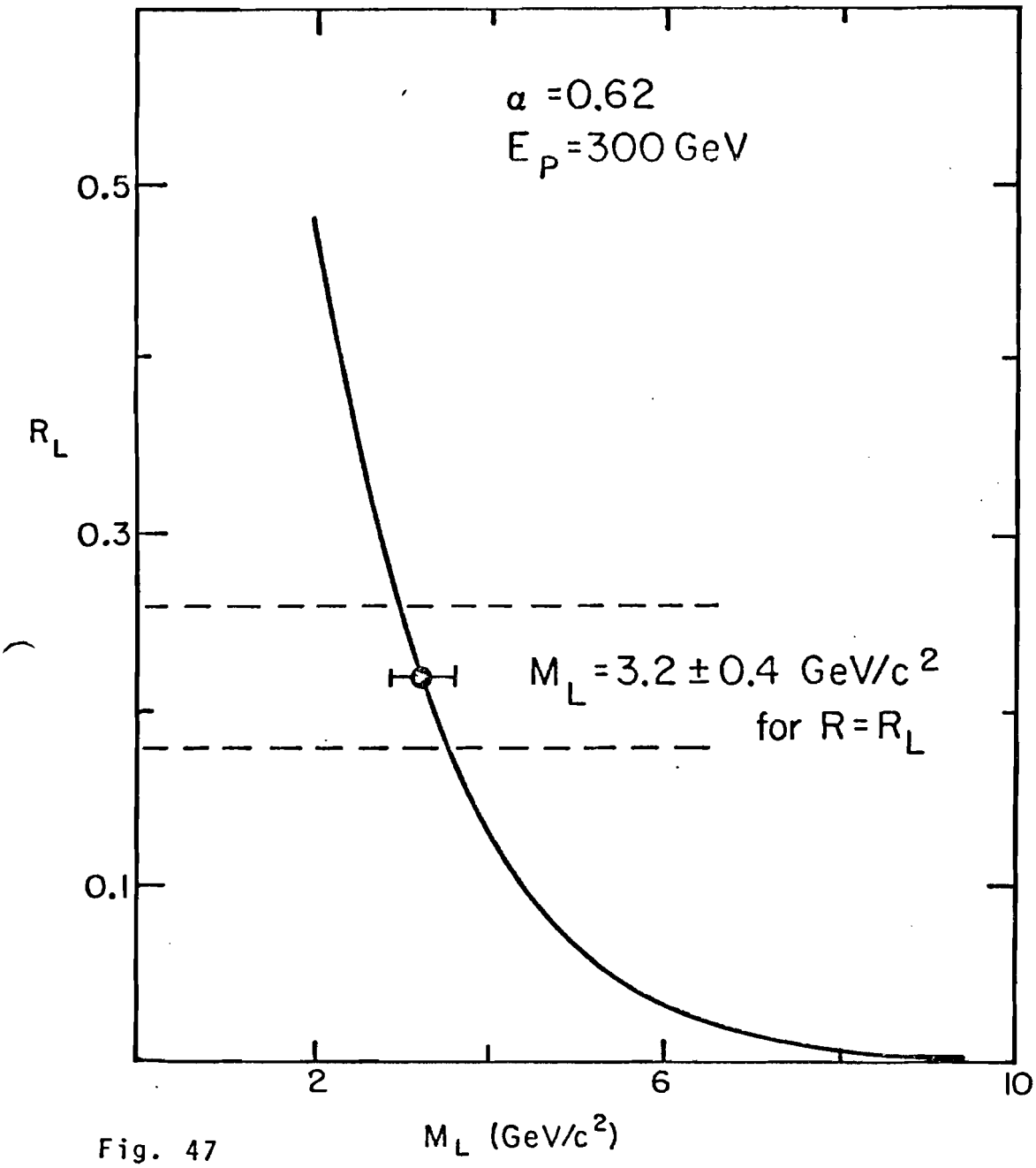

Fig. 47

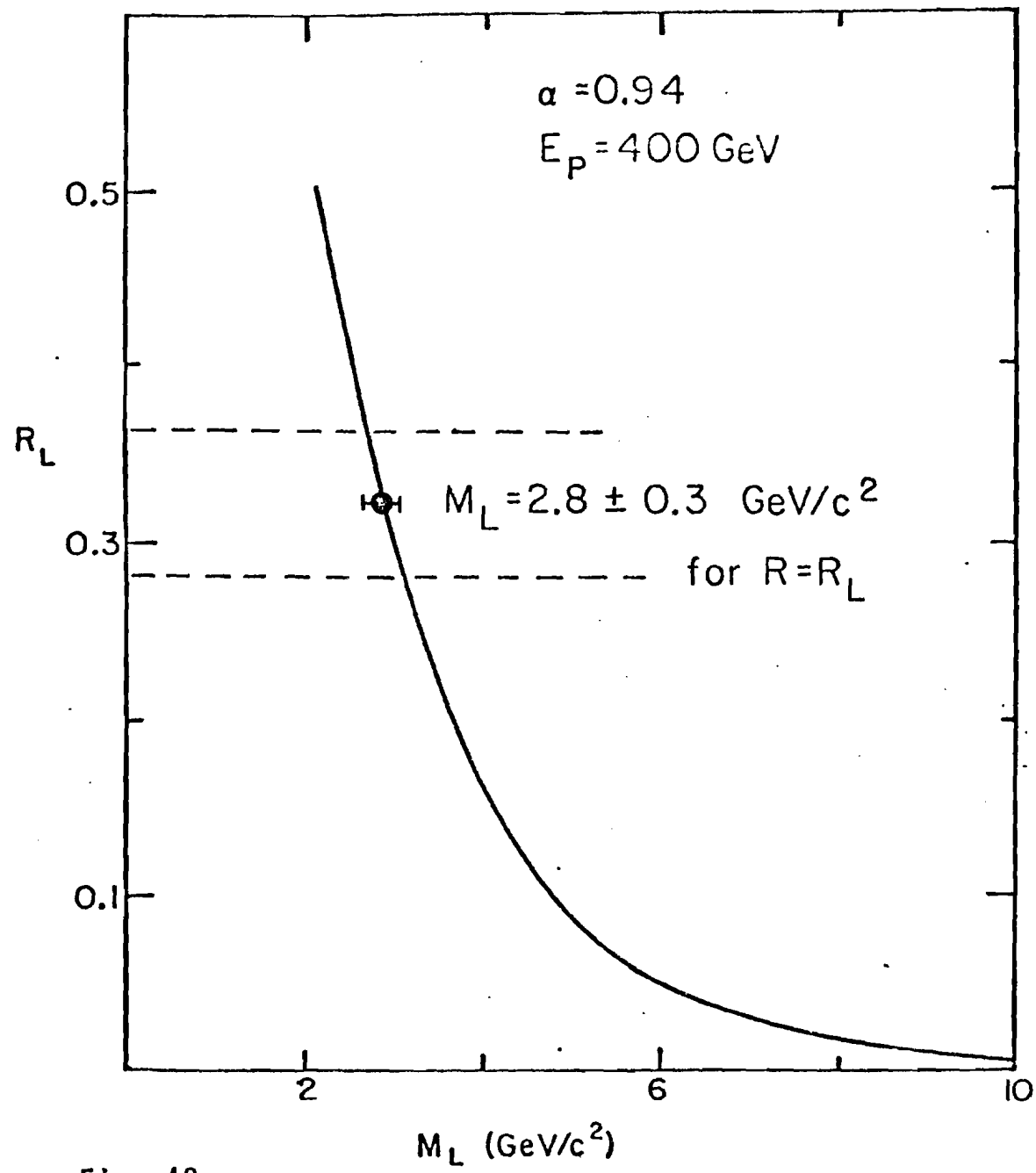

Fig. 48

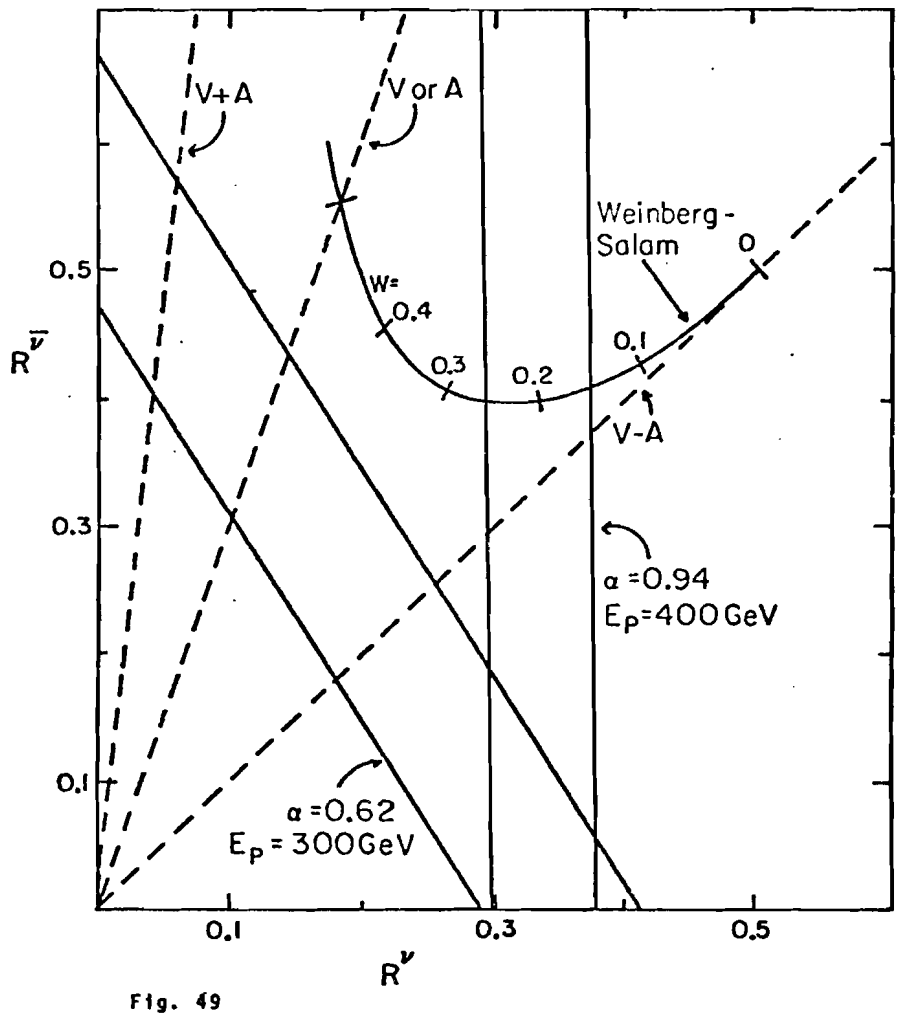

Fig. 49

/580076

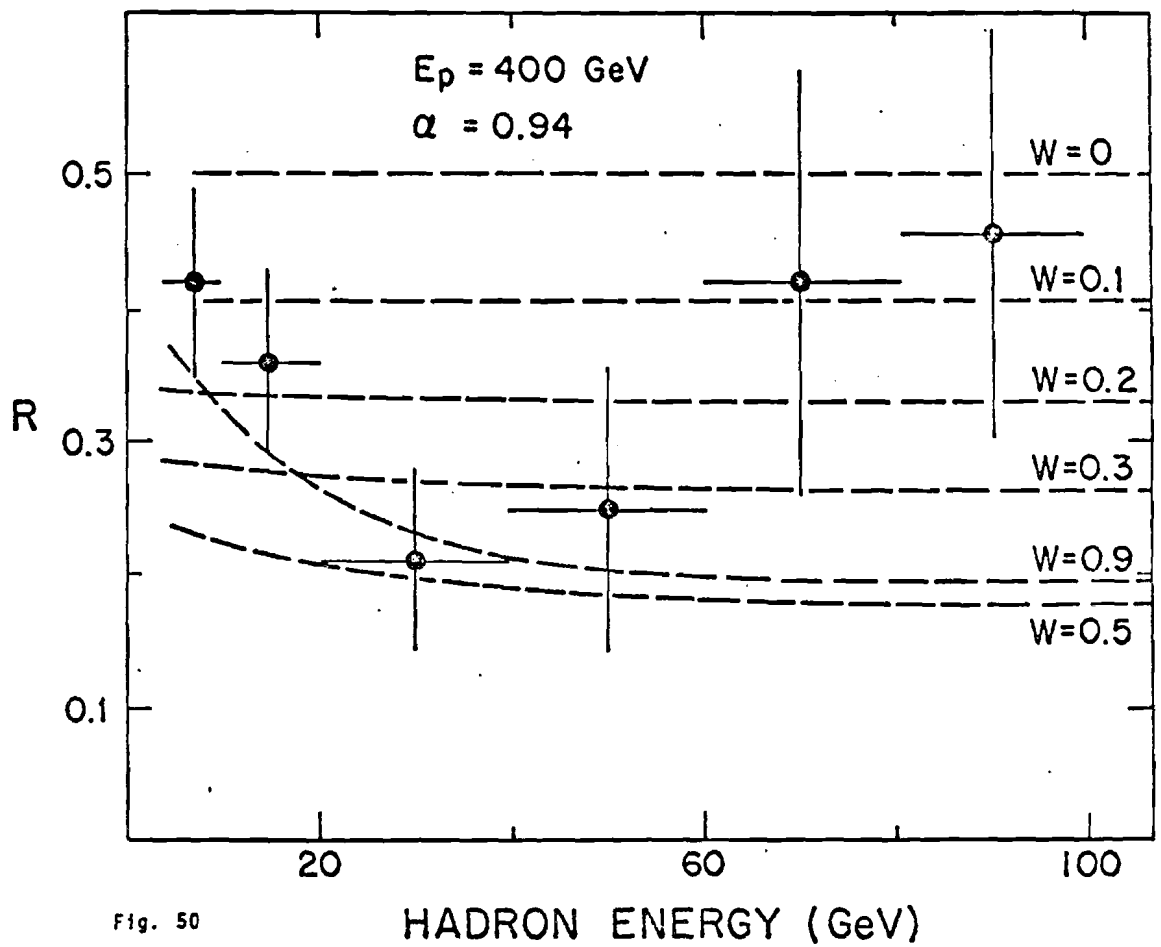
E_p = 400 GeV
α = 0.94
W = 0
W=0.1
W=0.2
W=0.3
W=0.9
W=0.5
R
0.5
0.3
0.1
20
60
100
HADRON ENERGY (GeV)

Fig. 50

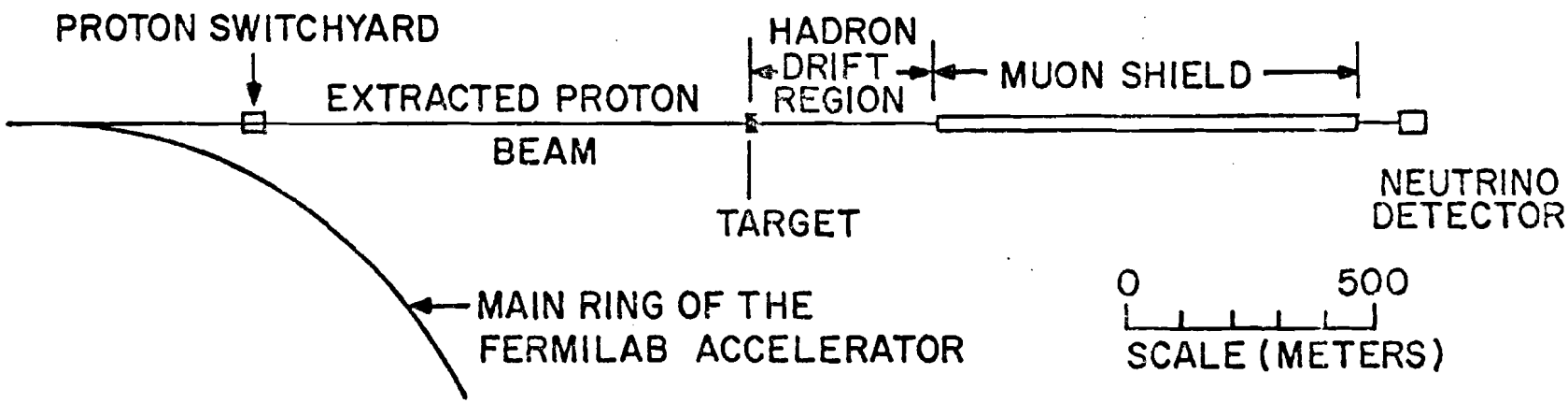
PROTON SWITCHYARD
EXTRACTED PROTON
BEAM
HADRON
DRIFT
REGION
MUON SHIELD
TARGET
NEUTRINO
DETECTOR
MAIN RING OF THE
FERMILAB ACCELERATOR
0
500
SCALE (METERS)

Fig. 51

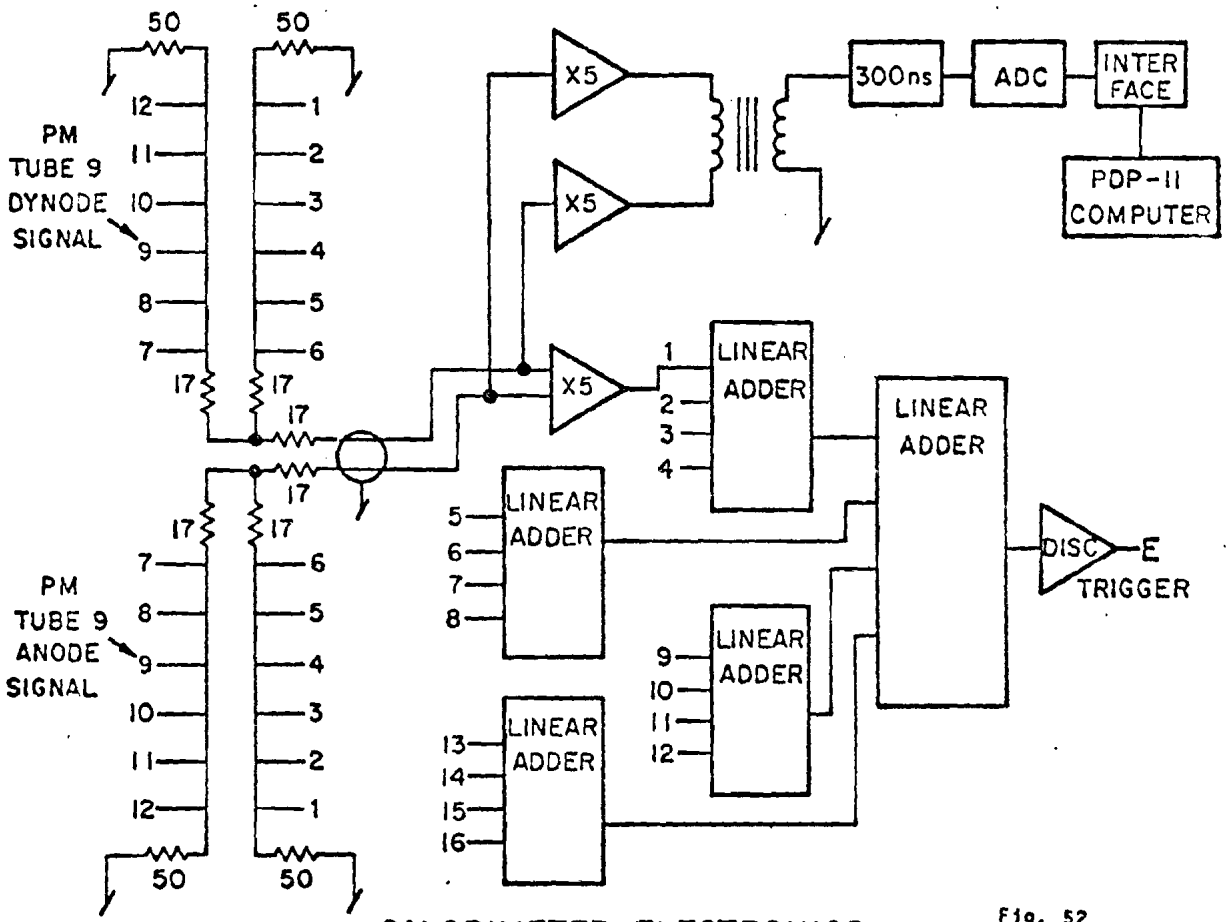

CALORIMETER ELECTRONICS

Fig. 52

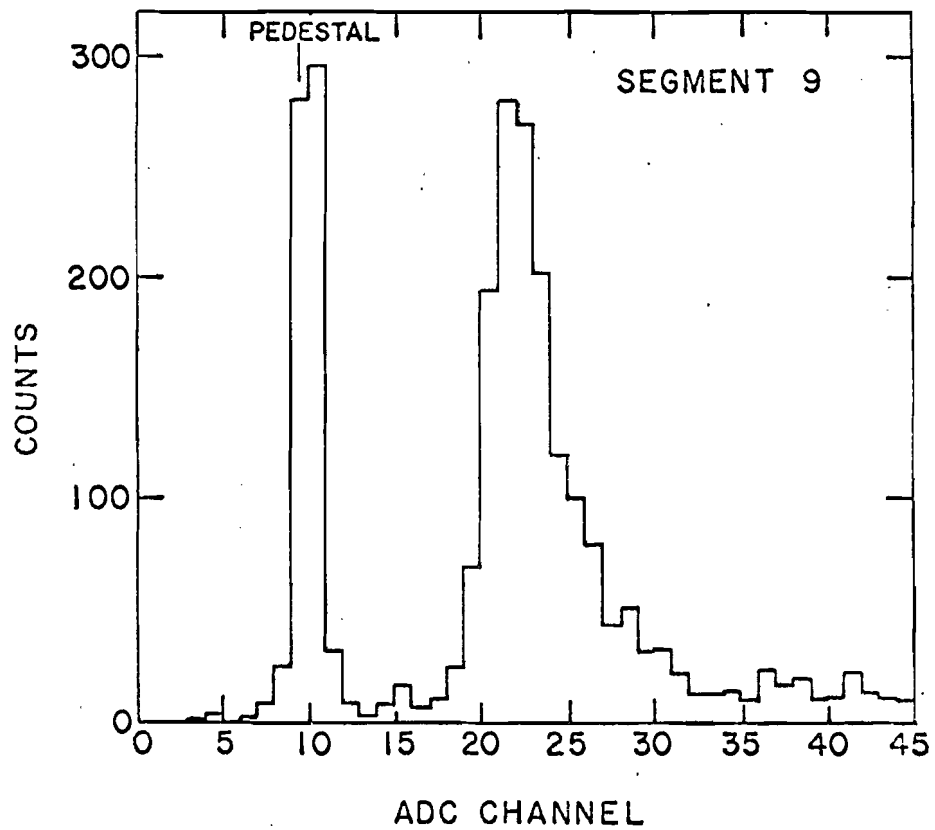
PEDESTAL
SEGMENT 9
COUNTS
300
200
100
0
0
5
10
15
20
25
30
35
40
45
ADC CHANNEL

Fig. 53

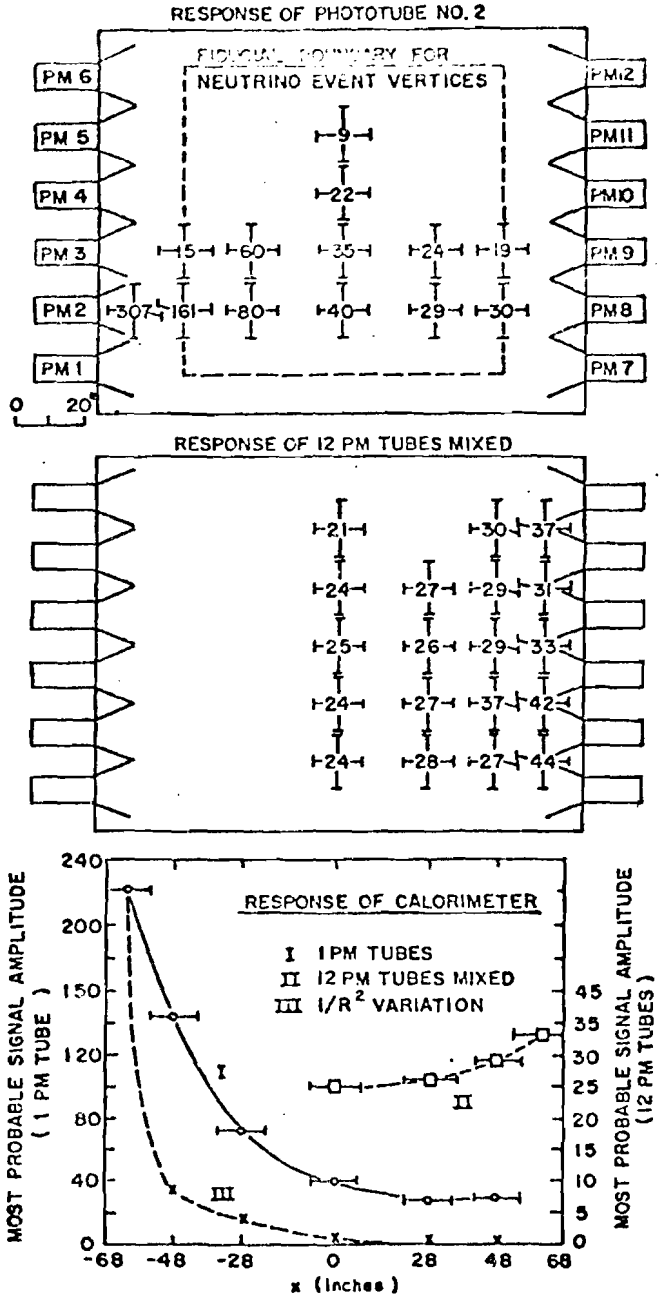
RESPONSE OF PHOTOTUBE NO. 2
FIDUCIAL BOUNDARY FOR
NEUTRINO EVENT VERTICES
PM 6
PM 5
PM 4
PM 3
PM 2
PM 1
PM12
PM11
PM10
PM9
PM8
PM7
9
22
15
60
35
24
19
307
161
80
40
29
30
0 20
RESPONSE OF 12 PM TUBES MIXED
21
30
37
24
27
29
31
25
26
29
33
24
27
37
42
24
28
27
44
RESPONSE OF CALORIMETER
I 1PM TUBES
II 12 PM TUBES MIXED
III 1/R² VARIATION
MOST PROBABLE SIGNAL AMPLITUDE (1 PM TUBE)
MOST PROBABLE SIGNAL AMPLITUDE (12 PM TUBES)
x (inches)
240
200
150
120
80
40
0
45
35
30
25
20
15
10
5
0
-68
-48
-28
0
28
48
68

Fig. 54

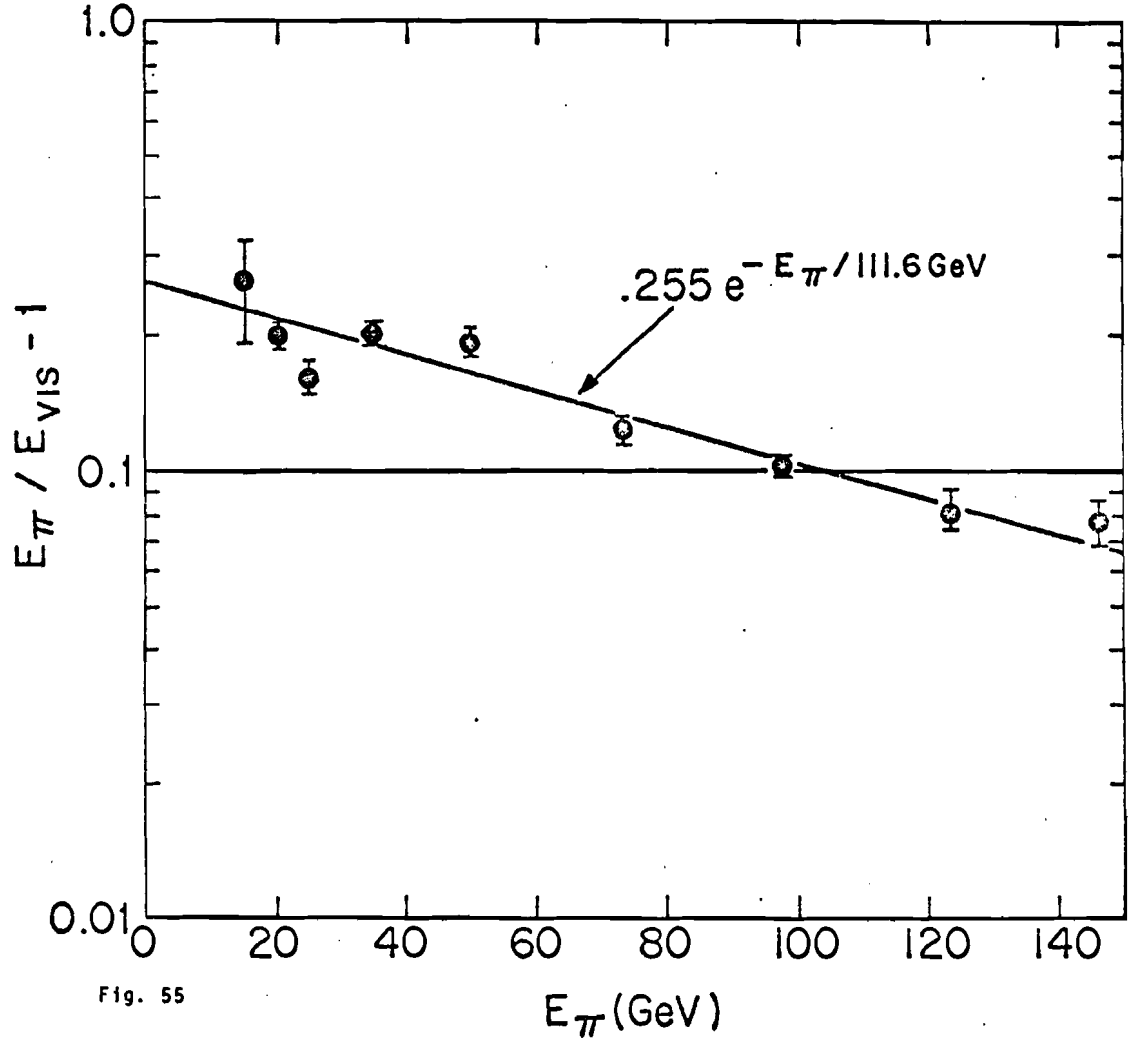
1.0
0.1
0.01
0
20
40
60
80
100
120
140
$E_\pi / E_{VIS} - 1$
E_π (GeV)
$.255\, e^{-E_\pi / 111.6\,\mathrm{GeV}}$

Fig. 55

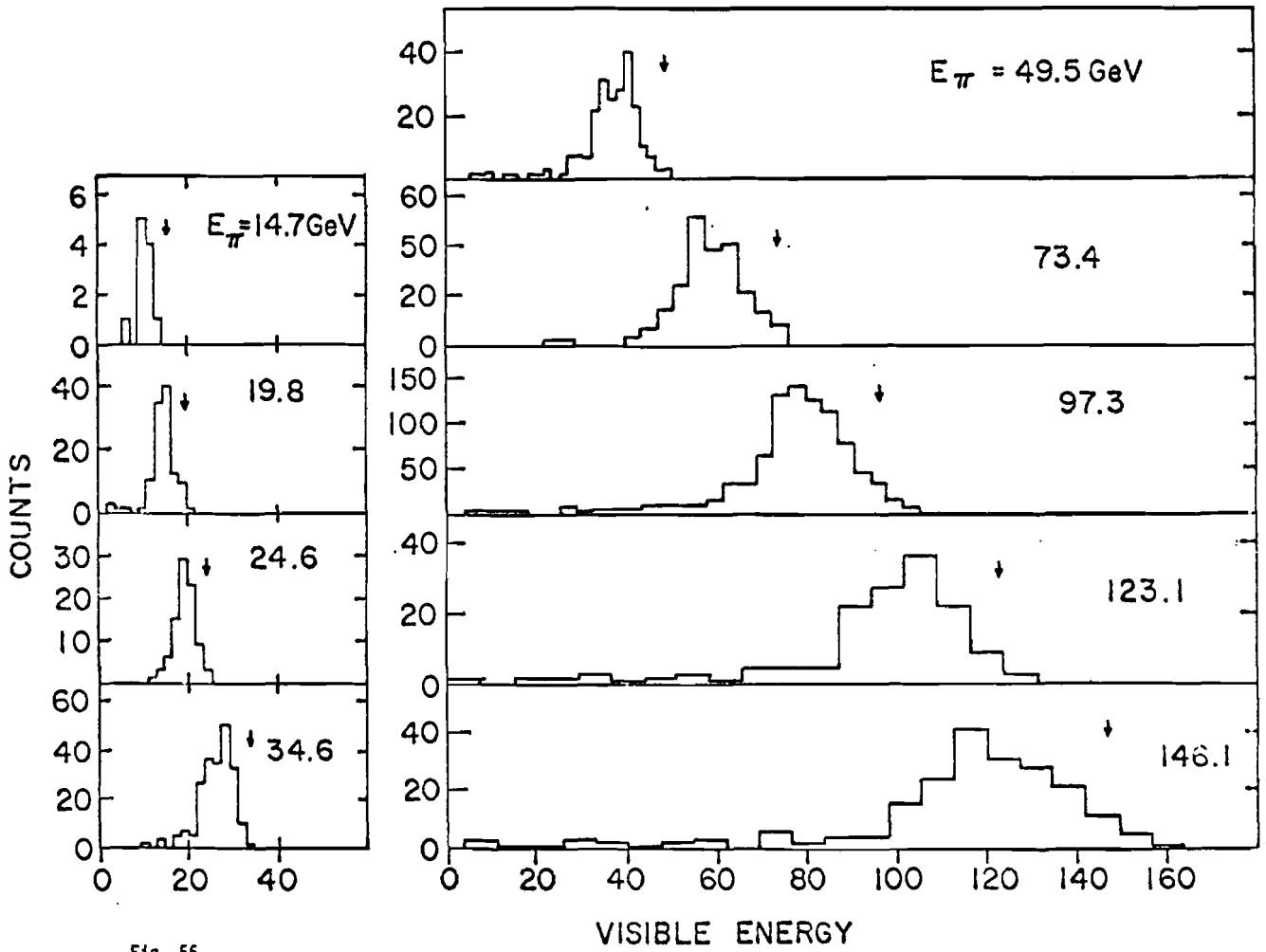
COUNTS
E_π=14.7GeV
19.8
24.6
34.6
E_π = 49.5 GeV
73.4
97.3
123.1
146.1
VISIBLE ENERGY

Fig. 56

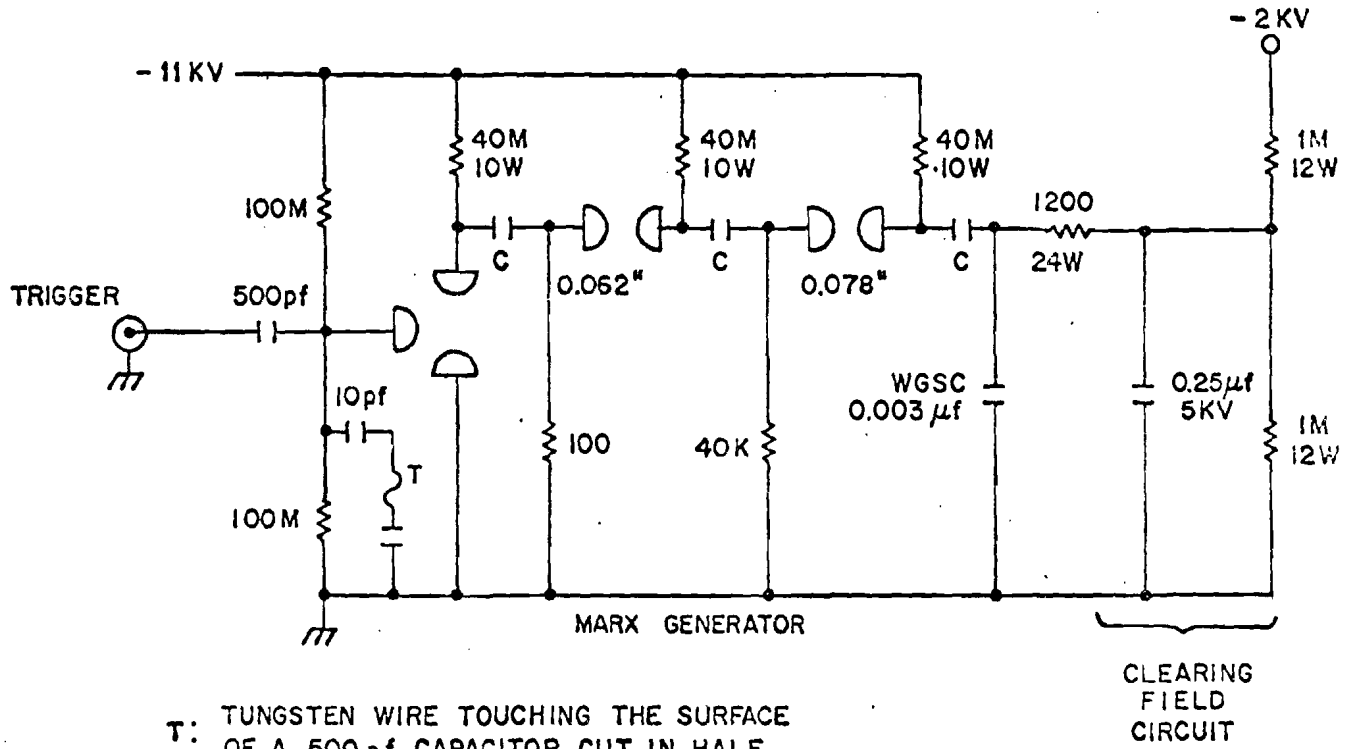

T: TUNGSTEN WIRE TOUCHING THE SURFACE OF A 500 pf CAPACITOR CUT IN HALF

C: 0.04μf ,15KV.

Fig. 57

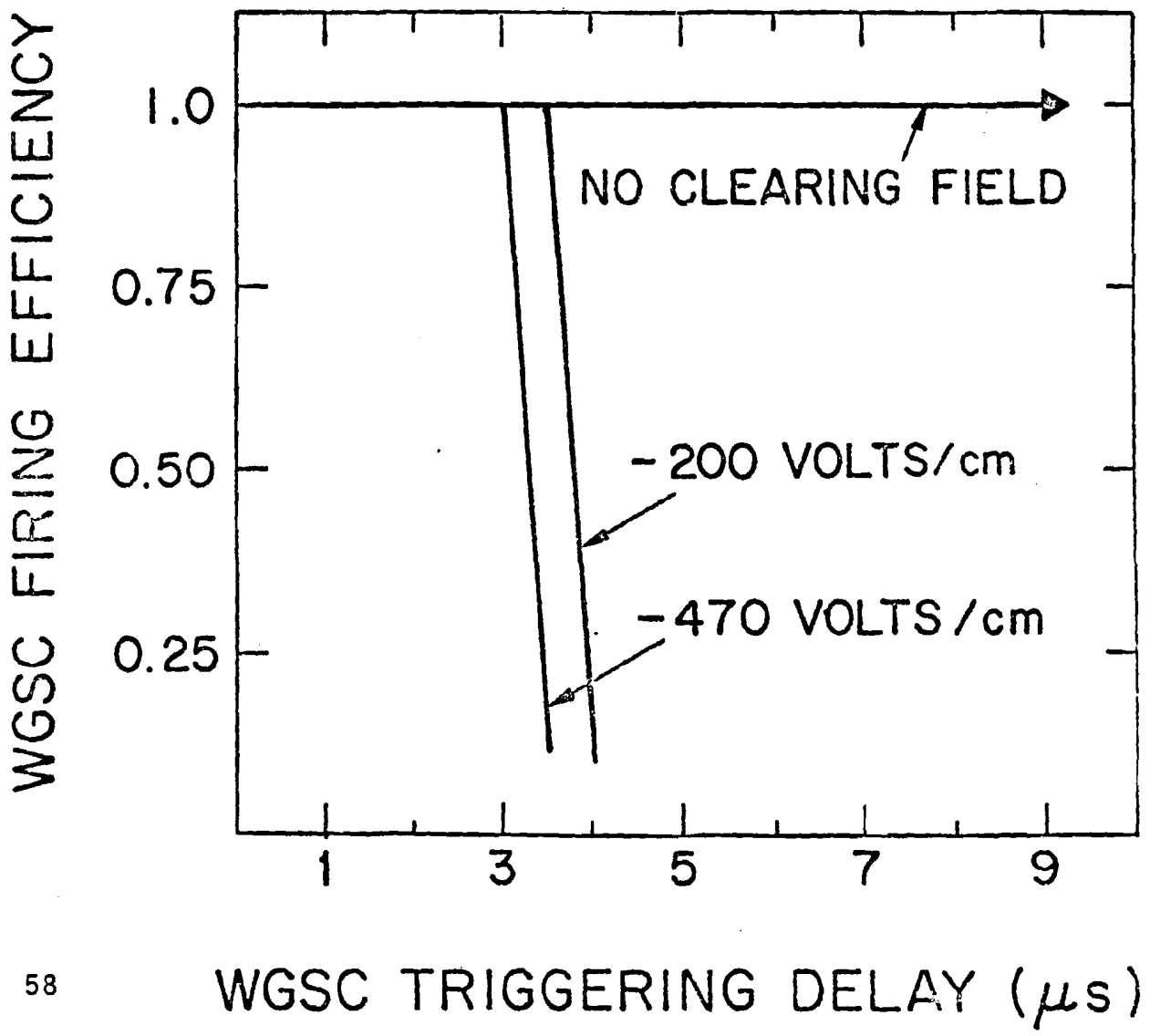
WGSC FIRING EFFICIENCY
1.0
0.75
0.50
0.25
NO CLEARING FIELD
-200 VOLTS/cm
-470 VOLTS/cm
1
3
5
7
9
WGSC TRIGGERING DELAY (μs)

Fig. 58

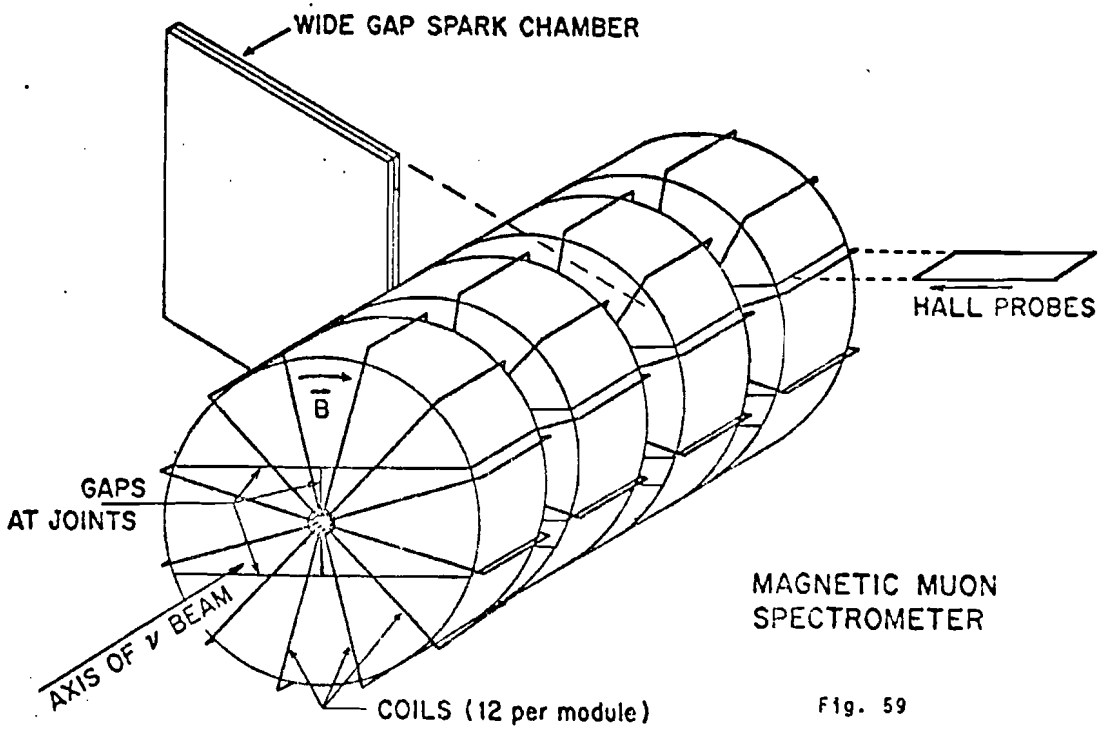

MAGNETIC MUON
SPECTROMETER

Fig. 59

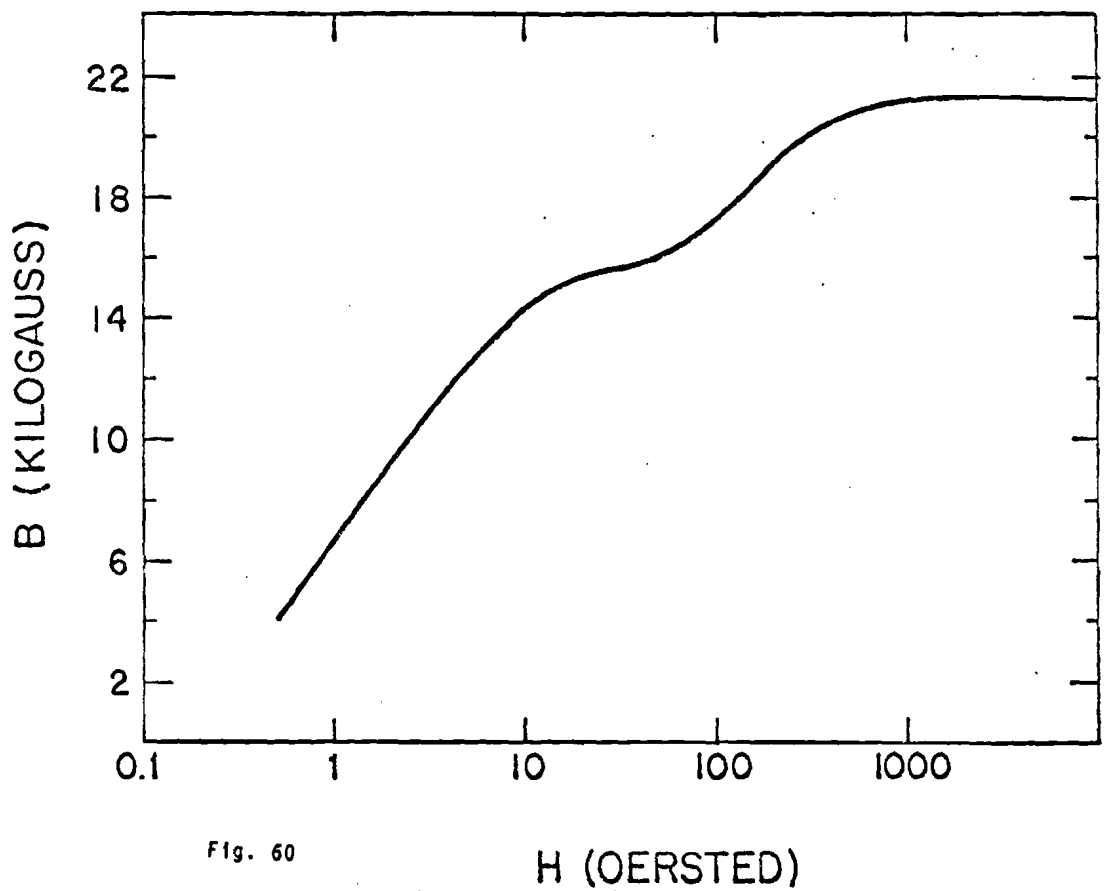

Fig. 60

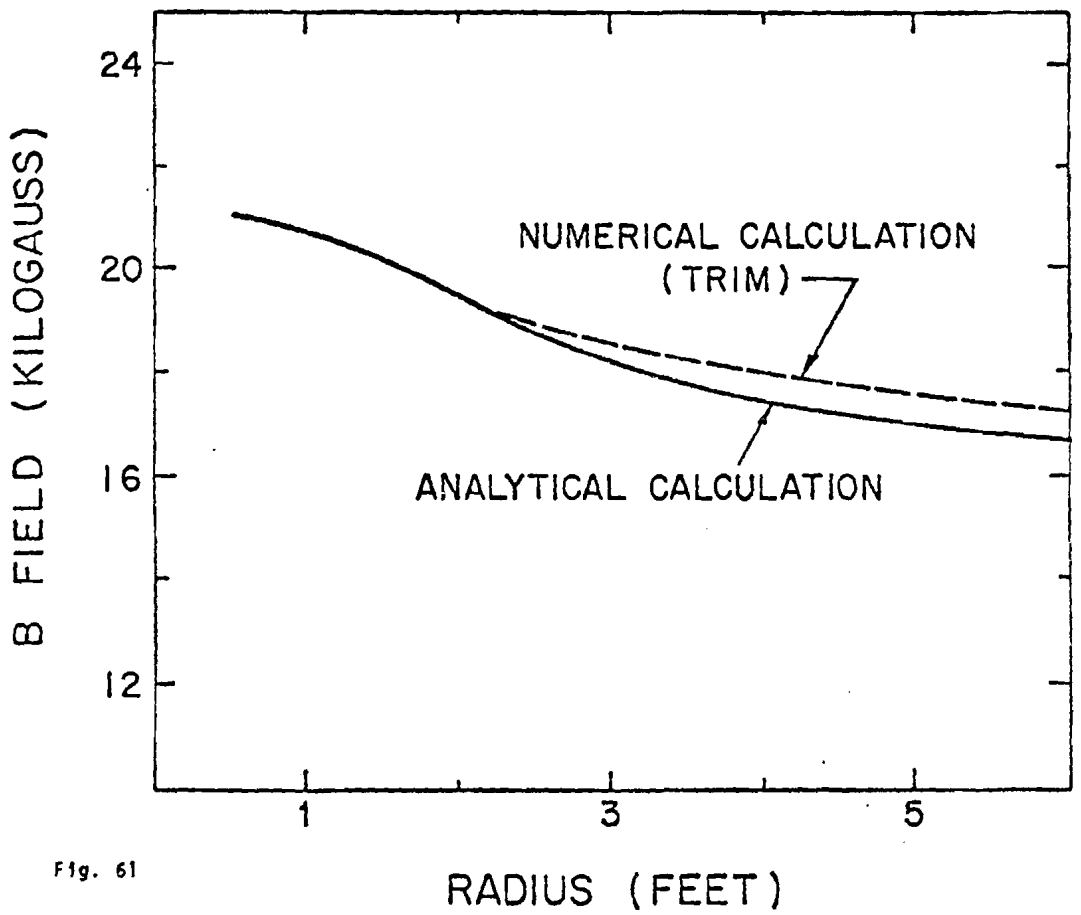
24
20
16
12
B FIELD (KILOGAUSS)
NUMERICAL CALCULATION
(TRIM)
ANALYTICAL CALCULATION
1
3
5
RADIUS (FEET)

Fig. 61

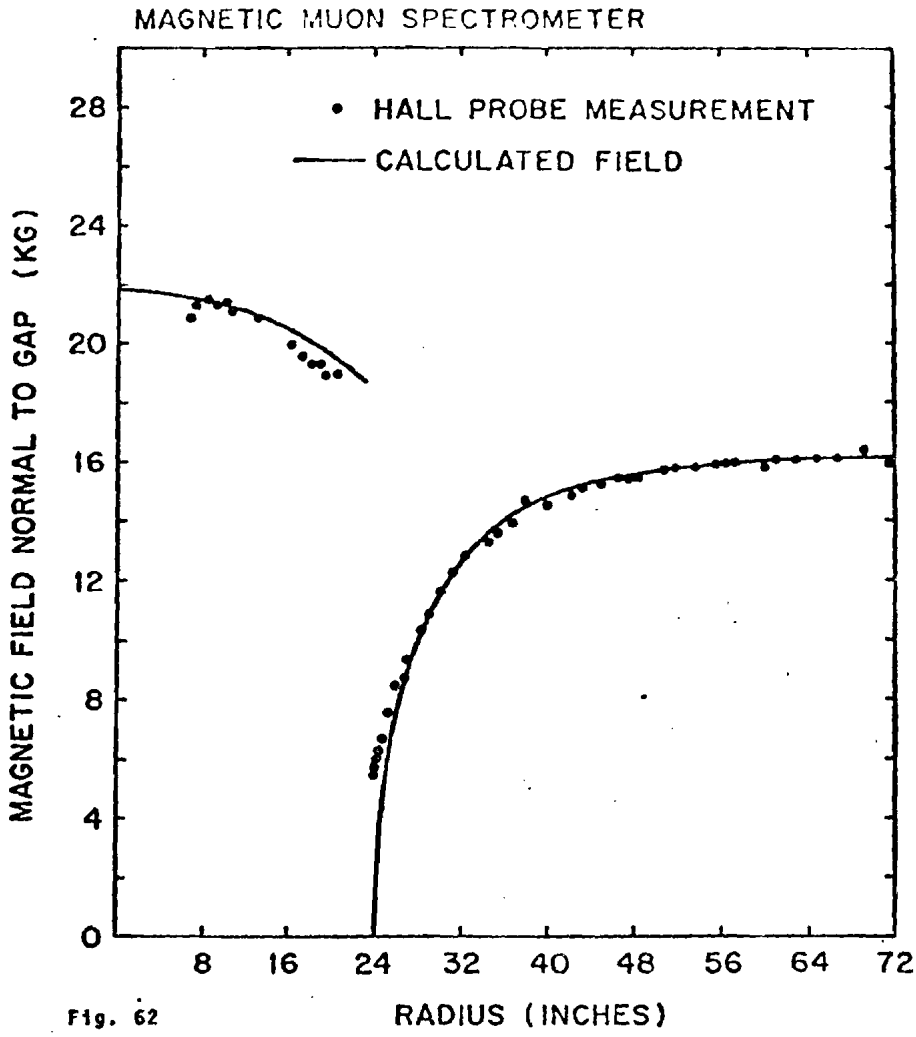
MAGNETIC MUON SPECTROMETER
• HALL PROBE MEASUREMENT
—— CALCULATED FIELD
MAGNETIC FIELD NORMAL TO GAP (KG)
0
4
8
12
16
20
24
28
8
16
24
32
40
48
56
64
72
RADIUS (INCHES)

Fig. 62

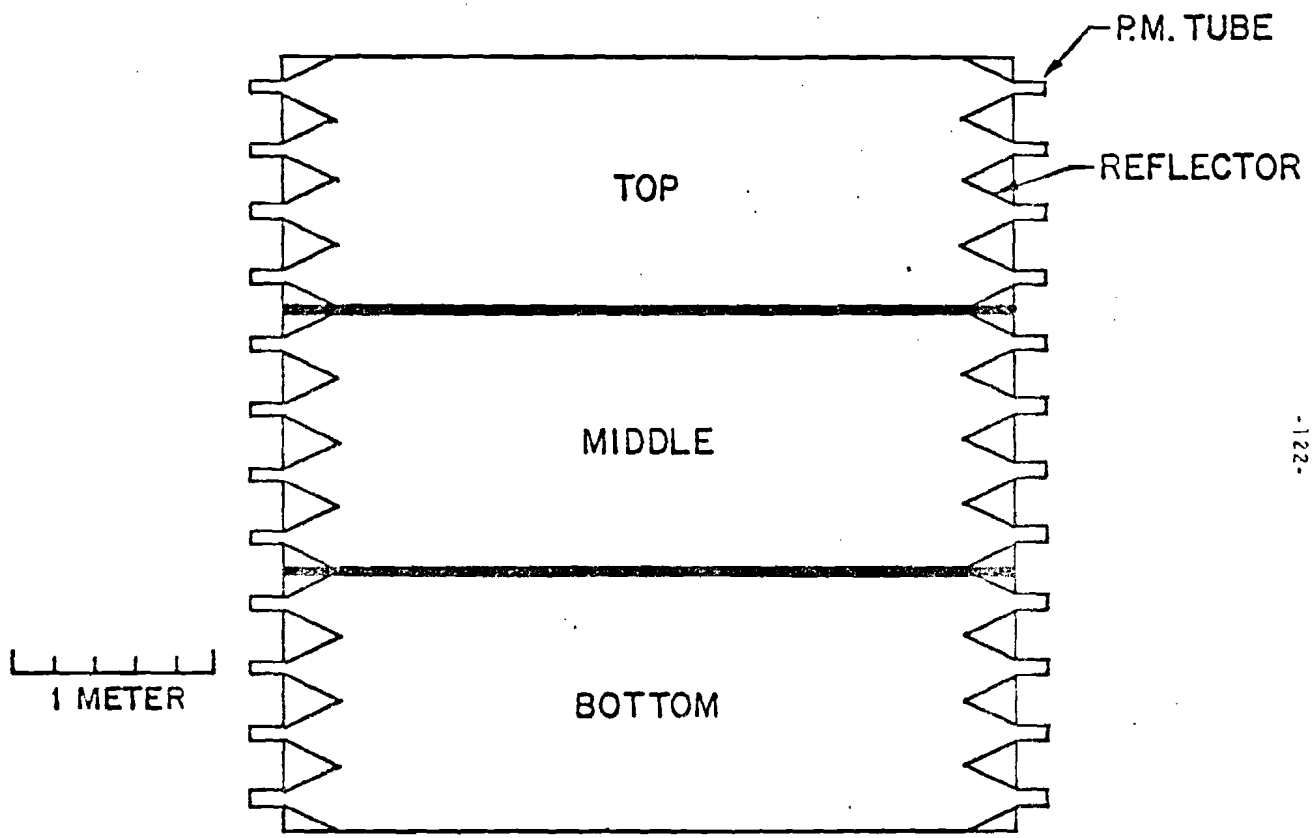

LIQUID SCINTILLATOR TRIGGER COUNTERS A,B,D

Fig. 63

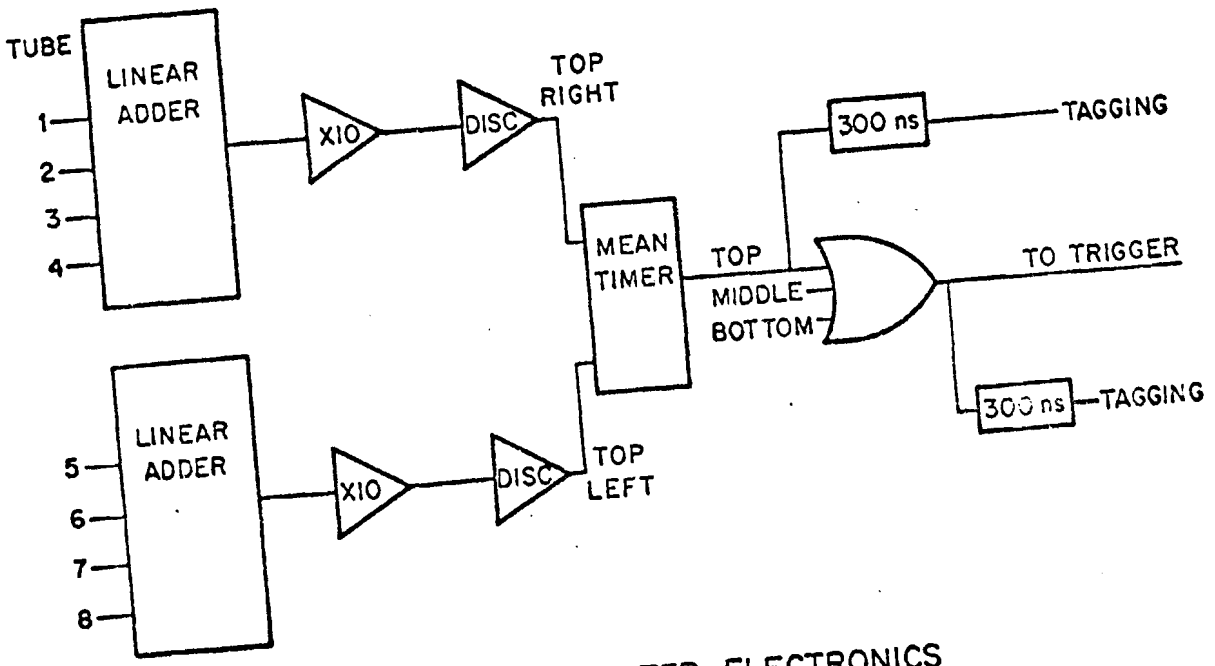

A,B,D COUNTER ELECTRONICS

Fig. 64

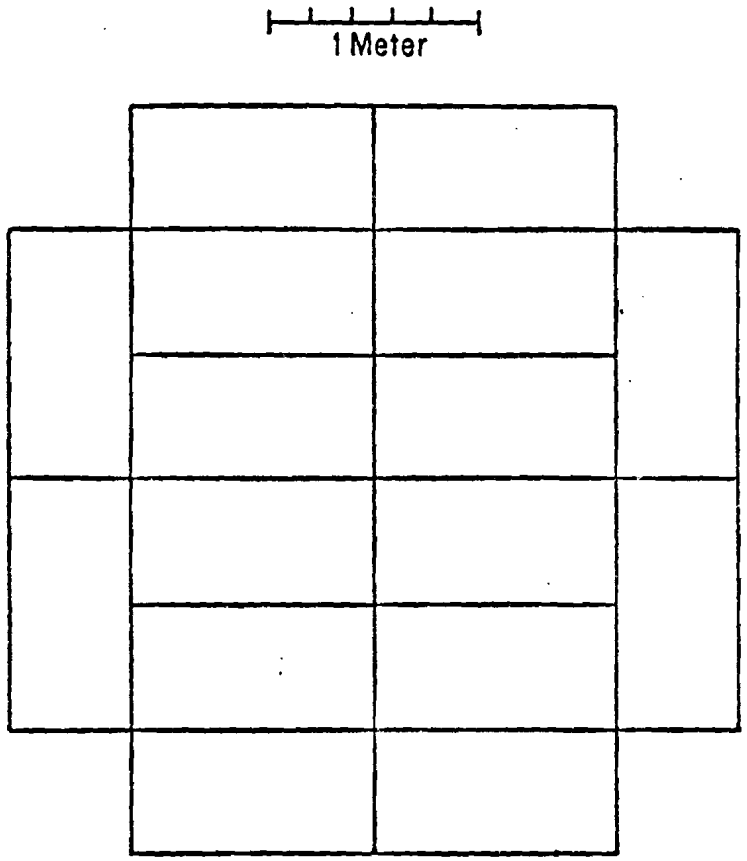

PLASTIC SCINTILLATOR TRIGGER COUNTER C

Fig. 65

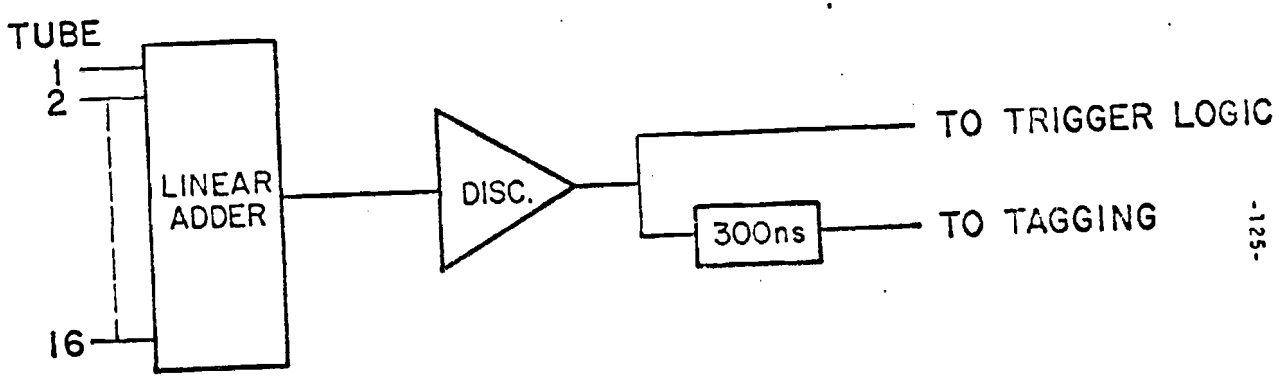

C COUNTER ELECTRONICS

Fig. 66

FRAME NUMBER ADVANCE

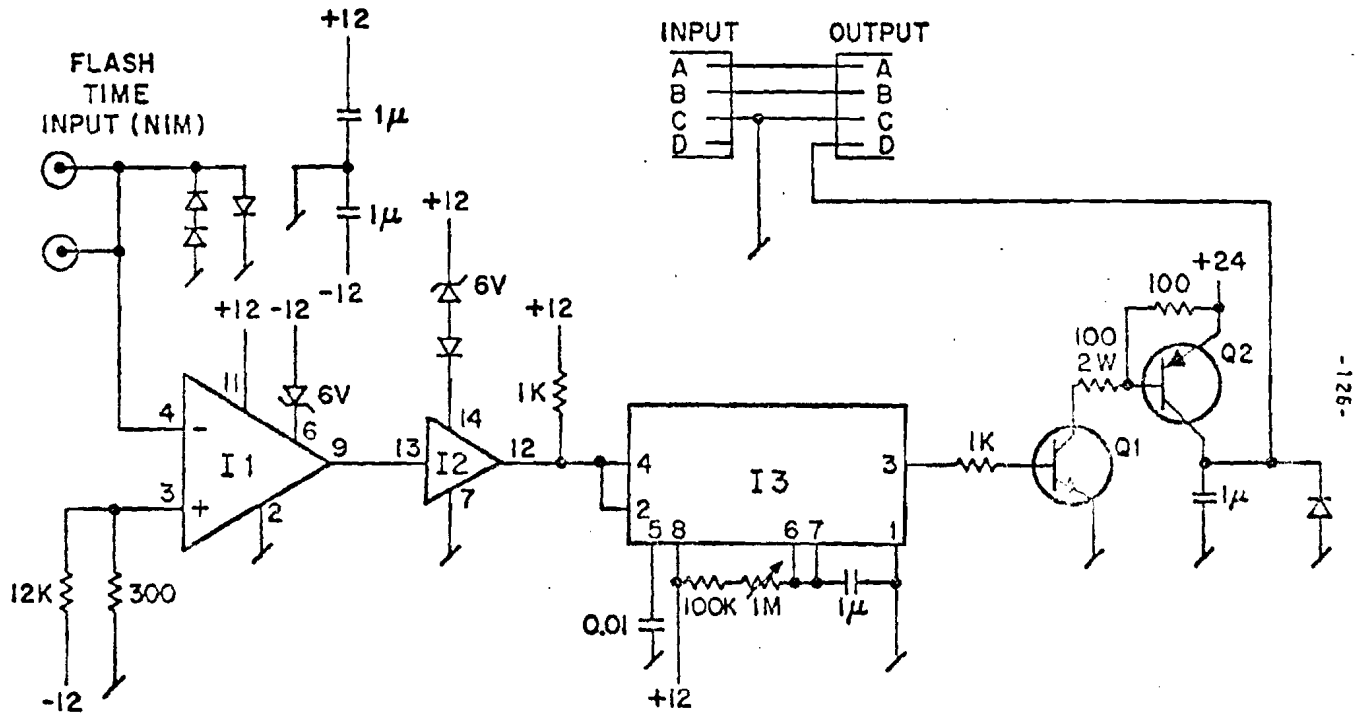

ALL RESISTORS 1/4 WATT
ALL DIODES 1N4002
ALL ZENER DIODES 6V

I1 SN72710
I2 SN7406
I3 NE555
Q1 2N2219
Q2 2N1905

Fig. 67

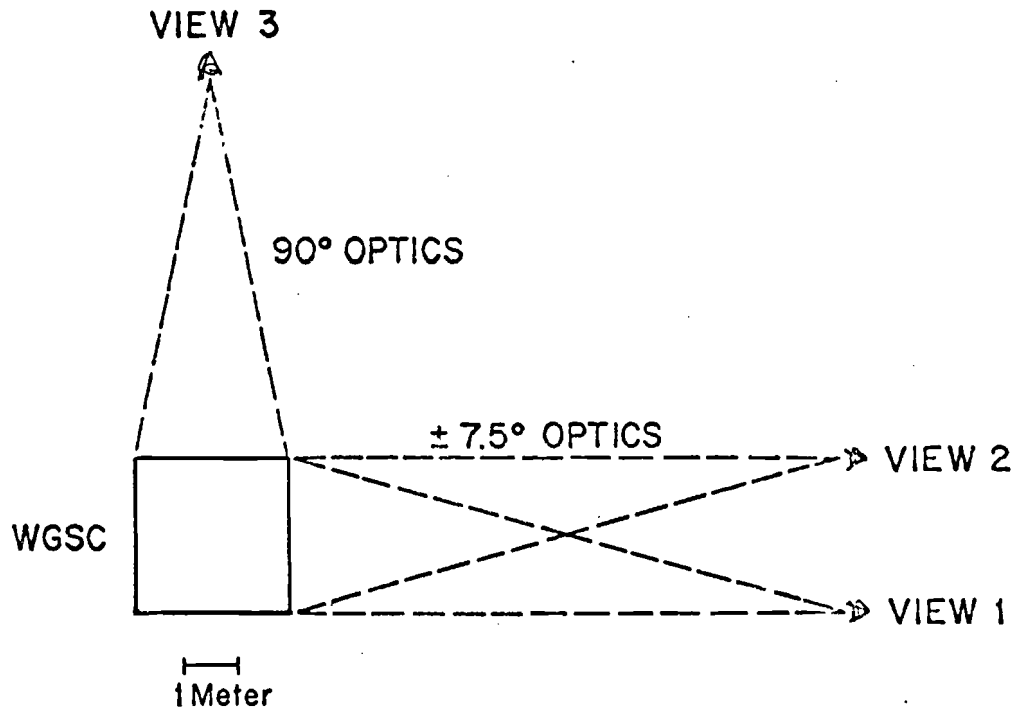

Fig. 68 EQUIVALENT OPTICAL SYSTEM

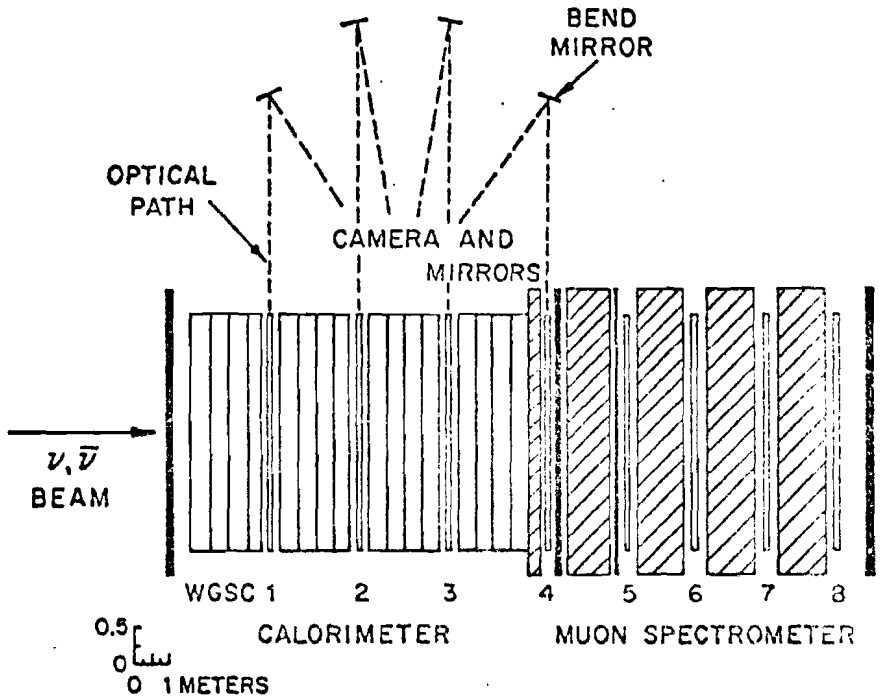

Fig. 69

90° OPTICAL SYSTEM

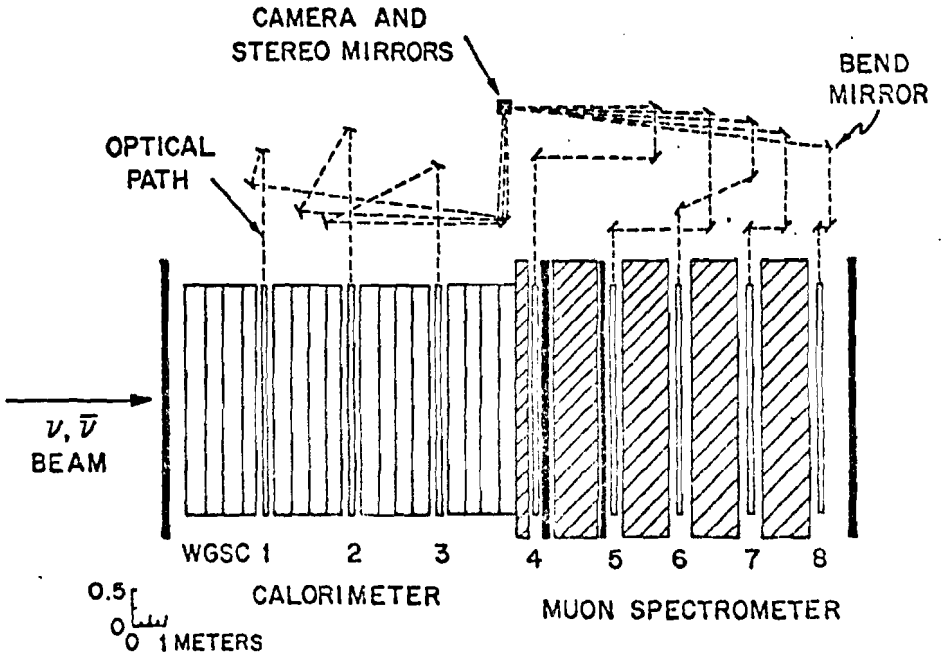

Fig. 70 ± 7.5° OPTICAL SYSTEM

OBSERVED MUON MOMENTUM SPECTRA OBTAINED
IN CALIBRATION RUNNING

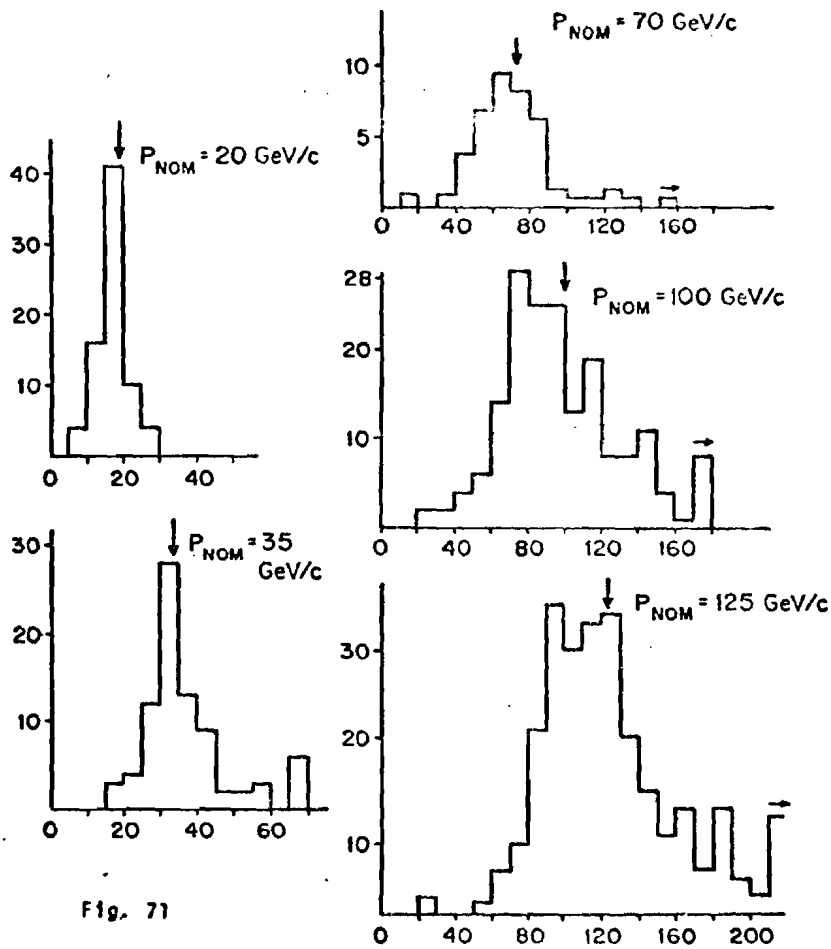

Fig. 71

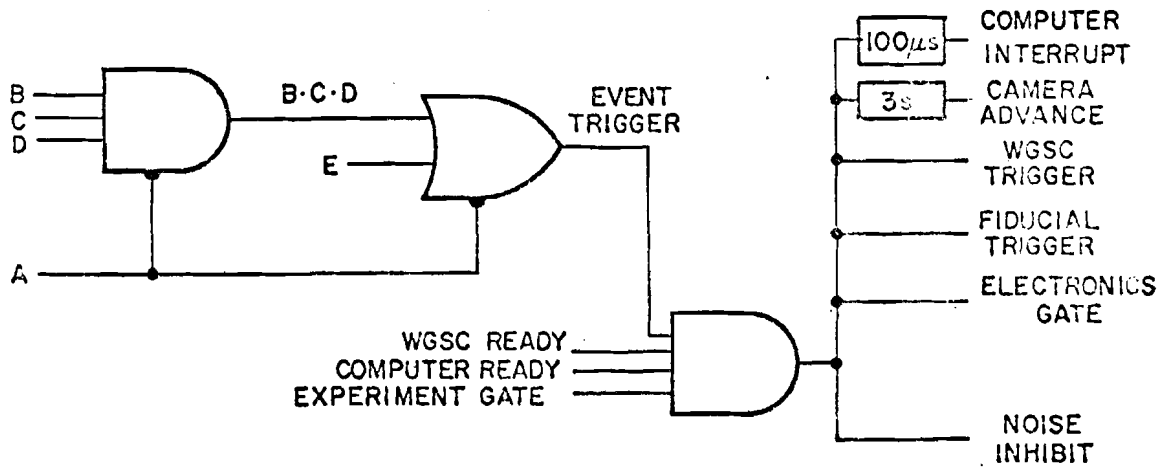

ELECTRONIC TRIGGERING LOGIC

Fig. 72

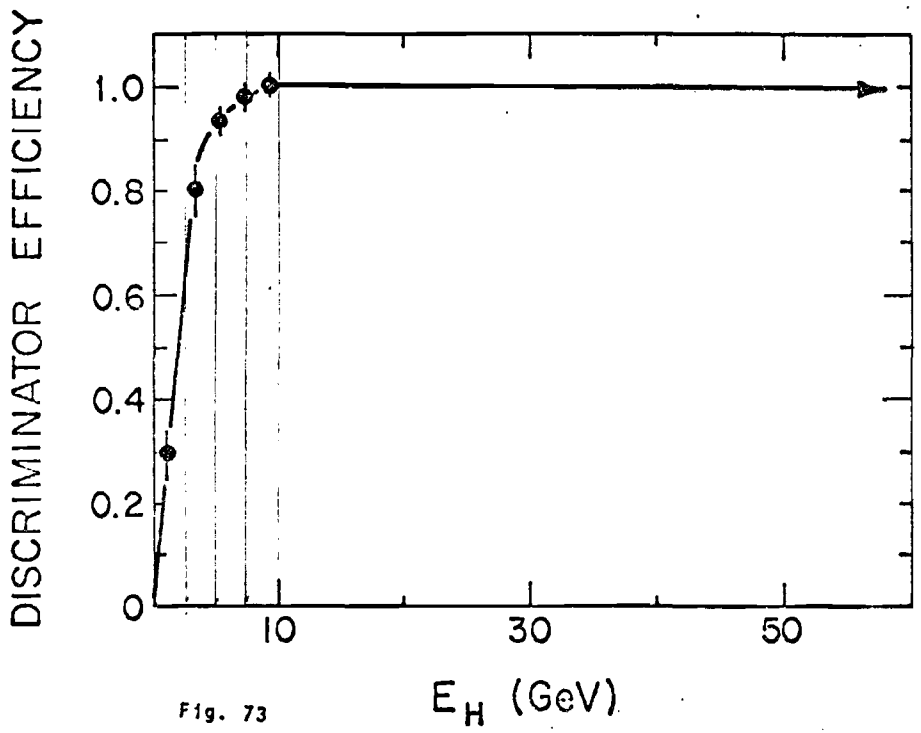

Fig. 73

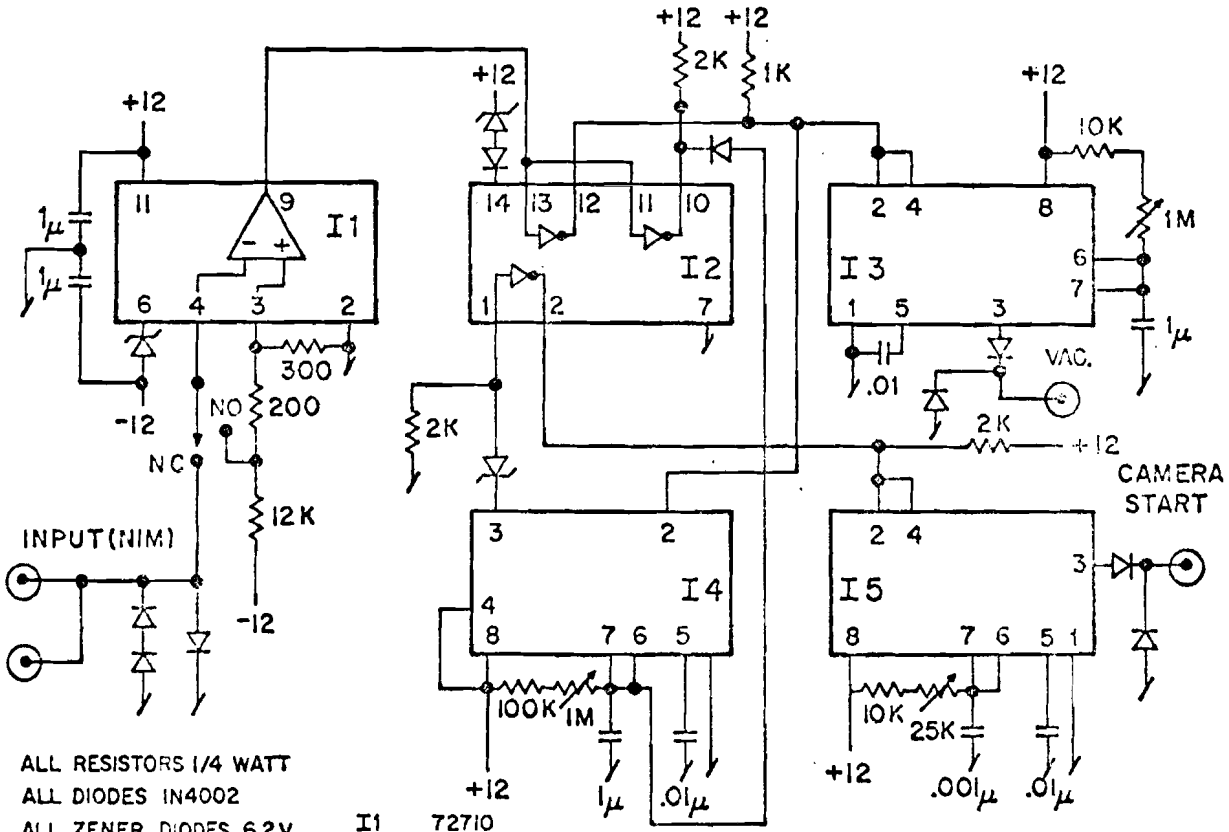

ALL RESISTORS 1/4 WATT
ALL DIODES IN4002
ALL ZENER DIODES 6.2V

I1 72710
I2 7406
I3-5 NE555

Fig. 74